Bridging the gap between protein microfluidic assay and precision oncology: developing sample preparation and assay standards for robust protein measurement

by

John J. Kim

A dissertation submitted in partial satisfaction of the

requirements for the degree of

Joint Doctor of Philosophy with University of California, San Francisco

in

Bioengineering

in the

Graduate Division

of the

University of California, Berkeley

Committee in charge:

Professor Amy E. Herr, Chair
Professor Bo Huang
Professor Liwei Lin

Summer 2018

Bridging the gap between protein microfluidic assay and precision oncology: developing sample preparation and assay standards for robust protein measurement

Abstract

Bridging the gap between protein microfluidic assay and precision oncology: developing sample preparation and assay standards for robust protein measurement

by

John J. Kim

Joint Doctor of Philosophy with University of California, San Francisco in Bioengineering

University of California, Berkeley

Professor Amy E. Herr, Chair

Microfluidics enables high-throughput protein measurements and holds great promise in unraveling the mechanisms underlying complex biological systems, such as the estrogen receptor signaling pathways in breast cancer. However, implementation of protein cytometry for precision oncology is stymied by insufficient classification and insight of protein isoforms, high sample losses during handling, and lack of standards that evaluate device performance. In my dissertation, I address each of these challenges by applying chemistry and physics to develop and optimize single-cell electrophoretic protein assays.

Lab-on-a-disc platform for sparse sample handling: To minimize cell handling losses in sparse samples from both clinical and experimental settings, we designed and developed a multi-stage assay using a lab-on-a-disc that integrates cell handling and subsequent single-cell western blotting. As the two-layer microfluidic device rotates, the induced centrifugal force directs dissociated cells to dams, which in turn localize the cells over microwells. Taking into account cell losses from loading, centrifugation, and lysis-buffer exchange, our lab-on-a-disc device handles cell samples with as few as 200 cells with 75% cell settling efficiencies. By integrating the lab-on-a-disc cell preparation and the single-cell western blot, our platform measures proteins from sparse cell samples at single-cell resolution.

Microparticle-delivered standards for protein sizing: To identify different protein species (i.e. isoforms) and complexes that are spatially resolved in the separation lanes of single-cell western blot, protein sizing standards are needed for thousands of separation lane to accurately measure the protein masses. Here, we developed a technique to deliver magnetic microparticles with protein sizing standards into microwells and integrate with the single-cell western blot workflow. Using nickel-histidine chemistry, we demonstrated that 80% of protein standards are released from microparticles within a time scale of in-situ cell lysis. After characterizing release and electrophoresis of protein sizing standards in hundreds of single-cell separation lanes, we successfully analyzed lane-to-lane and chip-to-chip technical variability and extracted mass sizes of cellular endogenous proteins from individual cells.

Single-cell western blotting for refining estrogen receptor taxonomy: Estrogen receptor (ER-α) is a key regulator of cancer growth, and different ER-α isoforms have been shown to affect hormone therapy response in breast cancer (BCa). Conventional immunoassays cannot selectively measure ER-α isoforms, given the high amino-acid sequence overlap between all isoforms of ER-α. To address this challenge, we demonstrate a high-selectivity, single-cell western blot, that distinguishes full-length ER-α66 from truncated ER-α46 in single cells by prepending an electrophoretic separation of proteins to a subsequent immunoassay. Employing this assay, we measured abundance and frequency of ER-α isoforms in ER-$\alpha^{+/-}$ BCa and identified a $< 10\%$ subpopulation of BCa cells with truncated ER-α46. Then, by treating cells with estradiol and tamoxifen, we discovered distinctive activations of ER-α signaling pathways from different BCa subtypes. Our single-cell quantitation of downstream ER-α and downstream signaling proteins have a potential to bring new therapeutic regimes for hormone-resistant cancers.

Kinetic binding measurement assay: Traditional biochemical assays suffer from low reproducibility and lengthy sample handling time to prepare a large set of samples. By using a microfluidic platform, serial preparation steps are reduced by exploiting a laminar flow and channel design to create spatial gradient and uniform concentration of proteins. Using a polyacrylamide gel as an size exclusion zone, the amount of bounded molecules over a different range of initial molecule concentrations are captured. The result of bounded fraction are plotted to find a dissociation constant rate of a receptor protein and its binding molecule.

Taken together, these advancements for robust protein measurement will provide a potential to apply microfluidic protein tools for precision oncology.

To my beloved family, colleagues, and friends

Contents

List of Figures

List of Tables

Acknowledgments

During my graduate work, I was fortunate enough to have support from incredible people. I wholeheartedly thank every past and current lab member. One of big reasons to join Herr lab is because of their enthusiasm and kindness. I sincerely appreciate Dr. Todd Duncombe, Dr. Chi-Chih Kang, Dr. Elly Sinkala, Dr. Julea Vlasakkis, Dr. Augusto Tentori for taking extra miles to guide and help me during my struggles in my projects. To Hector Neira, Elisabet Rosas, and Elaine Su, I am blessed to go through this PhD journey together and thank you for wonderful memory together. Hector deserves the best housemate and labmate I could ever asked for. Lastly and foremost, I owe Prof. Amy E. Herr a debt of gratitude. Prof. Herr is an exemplary scientist and mentor who has taught me how to carefully analyze and communicate science with communities. Her professionalism and passion for science truly motivate me to pursue my dream to inspire others like her and find a cure for cancer.

Before my graduate school, my first research experience started during my summer high school research program at University of California, Santa Barbara. I thank Dr. Douglas Thrower who introduced me to my first research experience in cancer and microtubule kinetics. After high school, I am extremely lucky to work in Brady Urological Institute at Johns Hopkins Hospital. I learned tremendous amount of biology and cancer by doing research with phenomenal oncologists. I especially cannot thank enough for Prof. Donald S. Coffey, who believed in me and taught me how to think creativity. Prof. Coffey's leadership and genuine hospitality influenced me to follow his footsteps in medicine.

Without my family and friends, I would not be the person I am today and be where I am now. I thank you so much to my grandmother who believed in me and sacrificed so much. I wish you were here with me. I owe my forever gratitude to my parents (Prof. Hyo Kim and Gi-Bun Lee) who sacrificed so much to provide me high education. I also cannot thank enough to my lifetime supporter and brother, Robert Kim. His guidance with intelligence and compassion motivated me to pursue science and engineering. Lastly, I thank my close friends who keep me in check and build unforgettable memories together: Hikaru Miyazaki, Anthony Turk, Phillip Kang, Bennett Ng, Joe Dyer, Vikram Rajan, Stephanie Caronna, Ahmed Aly, Kiwoo Shin. I dedicate this dissertation to all my family and friends.

Chapter 1

Introduction

1.1 Motivation and Overview

Proteins are a group of macromolecules that carry information in living systems. Elucidating protein functions and structures has been an ongoing quest for biologists and engineers, as proteins are directly associated with progression of many diseases. Although genomes do not vary much within the same organism, protein functions can be very heterogeneous. This inherent heterogeneity leads to complexity that is difficult to decode protein functions and cellular outputs. Protein abundance, post-translational modifications, and conformational states vary from cell to cell and generate complex systems with different cellular phenotypes that are not feasible to measure with current bulk and/or non-specific biological assays. As an example, estrogen receptor (ER-α) is one of protein markers that are stained in immunoassay to grade progression of breast cancer. About 80% of patients have breast cancer the ER-α positive and receive hormone therapy [1, 2]. However, about 16% of patients have cancer with drug resistance and do not survive more than 5 years [3, 4]. To assess and reverse the drug resistance in cancer, precision medicine necessitates quantitative protein tools with high specificity to identify and measure abundance and kinetics of proteoforms. The advances in quantitative measurement of proteoforms have a potential to solve the 'leaky' protein biomarker pipeline, in which only 3 5% out of $>$ 7000 new protein biomarkers reach to clinical diagnostics and therapeutics [5, 6].

A considerable discrepancy (2.5% - 26%) in protein biomarker grading in immunoassay between clinics can occur due to lack of standardization in sample preparation, semi-quantitative analysis, and assay evaluation [6–8]. In order to develop biomarkers and personalized drugs that selectively target a pathological condition, integrated and automated assays are essential for reproducible and precise protein measurements. Sample preparation can benefit from recent advances in microfluidics. Because of deterministic fluid flow inside a microchannel and capability of parallel processing, microfluidic assays can integrate sample preparation modules with detection modules to reduce errors and losses in sample handling. In the chapters 2 and 5, we design and develop integrated microfluidic tools to reduce loss

of rare cell samples and serial protein dilutions to measure binding kinetics of proteins [9].

Moreover, the facile integration of modules in microfluidics is realized in evaluation and validation of device reproducibility and specificity. Consistency of protein analysis between device replicates is achieved by utilizing analytical standard materials to each replicate. In the chapter 3, we develop microparticle delivery of protein standard markers to evaluate single-cell protein sizing performance within and across the replicates.

Besides sample preparation and device evaluation, semi-quantitative and bulk protein measurement can mask an essential information about heterogeneous cellular functions and associations of proteoforms in cellular signaling pathways. In the chapter 4, we extensively characterize and investigate heterogeneity of full-length and truncated ER-α isoforms and proteins associated with ER-α signaling pathways in response to hormone treatments (E2 and tamoxifen) in individual breast cancer cells. Quantitative analysis of proteoforms at a single-cell resolution will provide rich information about cell subpopulations that develop resistance or sensitization to targeted therapies.

The following sections describe fundamental principles of physics and separation science applied for designing and developing microfluidic protein assays.

Fluid Dynamics in Microfluidics

At microscale, fluid dynamics constitutes well-defined models that quantitatively describe the interplay between fluid flow and physical chemistry. Under the assumptions of fluid continuum and incompressibility, the conversation laws of mass, charge, and momentum are applied for describing phenomena under viscous fluids. The conservation law of linear momentum in a controlled volume is described as:

(Change of accumulation rate of momentum) = (Rate inflow of momentum) - (Rate outflow of momentum) + (Sum of forces)

The sum of forces are divided into two kinds in fluid dynamics: surface and body forces. Surface forces are composed of pressure, shear stress, and normal stress. Pressure is a common parameter used for controlling the fluid flow in microfluidic devices. Regarding the body forces, microfluidic technology exploits gravity, electric, magnetic, and centrifugal forces for controlling fluid and sparse particles. By applying the fluid incompressibility assumption and using divergence theorem in the conservation of momentum equations, Cauchy momentum is obtained:

$$\frac{\partial}{\partial t}\int_V \rho\vec{u}dV = -\int_S (\rho\vec{u}\vec{u})\hat{n}dA + \int_S \vec{\vec{t}}\hat{n}dA + \int_V \sum \vec{f}_l dV \tag{1.1}$$

$$\rho\frac{\partial\vec{u}}{\partial t}+\rho\vec{u}\cdot\nabla\vec{u}=\nabla\cdot\vec{\tau}+\sum\vec{f_i} \tag{1.2}$$

where ρ is the density, u is the flow velocity, τ is the shear tensor, n is the unit vector, f is the body forces per unit volume.

By decomposing the stress tensor into pressure and viscous forces, the Navier-Stokes equations for a Newtonian incompressible fluid are obtained:

$$\rho\frac{\partial\vec{u}}{\partial t}+\rho\vec{u}\cdot\nabla\vec{u}=-\nabla p+\nu\nabla^2\vec{u}+\sum\vec{f_i} \tag{1.3}$$

where ν= fluid kinematic viscosity, p is pressure.

The Navier-Stokes equations describe the motion of fluids as the balance among inertial, pressure, viscous, and external applied forces. For simulation and modeling, the Navier-Stokes equations are solved under the conservation of mass (the continuity equation) for incompressible fluid:

$$\nabla\cdot\vec{u}=0 \tag{1.4}$$

In microfluidics, viscous forces (diffusion) dominate over inertial forces (convection) under a laminar flow. To characterize a flow condition for microfluidic devices, a dimensionless momentum transport ratio of convection to diffusion, Reynolds number (Re), is used and defined as:

$$Re=\frac{uL}{nu} \tag{1.5}$$

Small characteristic velocity, characteristic channel length, or high viscosity lead to the small Re ($Re<1$)that indicates the laminar flow in microfluidic systems.

Stokes Flow as an Approximation for Particle Movement in Microfluidic Design

Considering that microfluidic systems involve small characteristic channel length and/or small velocity flow, the Stokes flow approximation is often applied to predict flow and particle behaviors with viscous friction. Assuming the body forces are zero for now, the Navier-Stokes equation can be written in a dimensionless form with the Re term:

$$\mathrm{Re}\left(\frac{\partial\vec{u}}{\partial t}+\rho\vec{u}\cdot\nabla\vec{u}\right)=-\nabla p+\nabla^2\vec{u} \tag{1.6}$$

As Re becomes really small ($Re \rightarrow 0$), the equation is simplified without non-linear terms and described as the Stokes flow equation:

$$0 = -\nabla p + \nabla^2 \vec{u} \tag{1.7}$$

For the uniform and laminar flow around a fixed particle (Figure 1.1), the analytical solution of the Stokes flow is used to describe the drag force from viscous forces (F_d):

$$F_d = 6\pi R_{ij} \rho \nu \vec{U} \tag{1.8}$$

where U is the fluid velocity relative to the particle, and R_{ij} is the translational tensor. For a solid sphere, R_{ij} is replaced with radius of the sphere (a) and resulted in the classical Stokes drag law.

$$F_d = -6\pi a \rho \nu \vec{U} \tag{1.9}$$

For the following sections, the balance of viscous forces and body forces is outlined to design, optimize, and integrate processes of sample handling and proteoform detection in microfluidic assays.

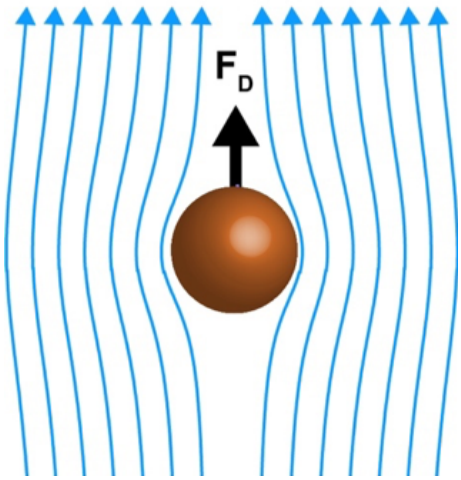

Figure 1.1: Flow streamlines around a fixed particle. Under a laminar flow with Re <<1, the viscous force (F_D) acts on the particle.

Newtons Second Law and Governing Forces in Microfluidics

Microwells are widely utilized to isolate intact single cells for subsequent analysis. [10–13] Microwell arrays have been used for high throughput and automatic analysis of DNA [13–15] and protein[16, 17] from hundreds to thousands of cells. Gravity is commonly used to sediment

single cells into open microwells, followed by in-situ cytometry. To conduct electrophoresis of single-cell lysate, an external electric field is applied across cell-laden microwells (fabricated in agarose or polyacrylamide) to initiate and drive electrophoresis separation. Physically isolated inside microwells, intact individual cells are readily monitored for cell morphology [18, 19] and lysed to measure DNA damage and repair [13, 20], transcriptional levels [14, 15], and protein expression [21, 22].

In the chapters 2 – 4, an open microfluidic device format comprising an array of microwells cast in a thin layer of polyacrylamide gel is developed and utilized to perform electrophoretic analyses of isolated mammalian cells, including circulating tumor cells and breast cancer cells [9, 16, 23–26]. Each microwell acts as a reactor for cell and microparticle preparation, with endogenous and microparticle-delivered proteins then subjected to electrophoretic analysis (i.e., protein PAGE, isoelectric focusing) in the surrounding polyacrylamide gel layer.

As cells and proteins are assumed to be spherical particles in the laminar flow, passive and active forces are assessed to characterize the microfluidic processes (Figure 1.2).

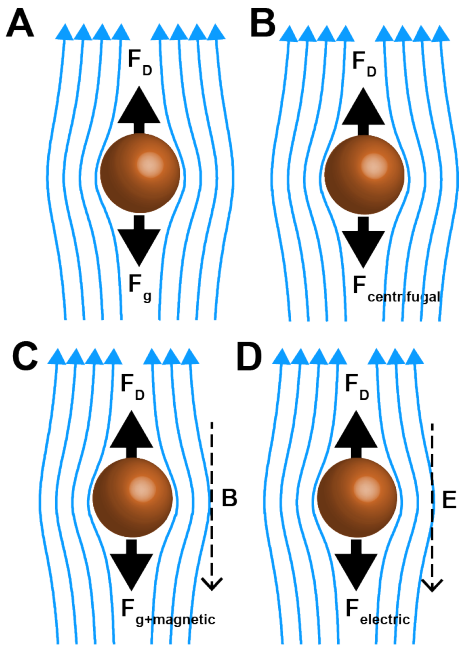

Figure 1.2: Different dominant forces on cells, microparticles, and proteins in microfluidic systems throughout the dissertation chapters. (A,B) In order to settle cells in the microwell array, passive gravity and centrifugal forces are used. (C) Magnetic and passive gravity forces are used to settle microparticles in the microwell array. (D) Under an electrical field, Coulomb force is applied on proteins to migrate inside the microfluidic devices.

Particle Sedimentation and Centrifugation

For passive gravity settling of cells in the microwells, force of gravity (including buoyant force) and drag force are dominant forces (Figure 1.2A). The force balance for the cells that are freely falling in microwells is described as:

$$6\pi a\rho_{fluid}\nu\vec{U} = \frac{4}{3}\pi a^3\left(\rho_{cell} - \rho_{fluid}\right)\vec{g} \tag{1.10}$$

Solving the equation above, the terminal velocity of cell sedimentation is described as:

$$\vec{U} = \frac{2}{9}\frac{a^2}{\nu}\left(\frac{\rho_{cell}}{\rho_{fluid}} - 1\right)\vec{g} \tag{1.11}$$

Of note, the terminal velocity is proportional to the square of cell radius, which is exploited for fractionation of cells with different diameters in the chapter 2. Furthermore, controlling cells are further refined by utilizing centrifugal force perpendicular to the passive gravity. Similar to the gravity settling, the centrifugal force and the drag force balance out in the rotating reference frame (Figure 1.2B).

$$\vec{U} = \frac{2}{9}\frac{a^2}{\nu}\left(\frac{\rho_{cell}}{\rho_{fluid}} - 1\right)\left[\vec{\omega}\times\left(\vec{\omega}\times r\right)\right] \tag{1.12}$$

$$\vec{U} = \frac{2}{9}\frac{a^2}{\nu}\left(\frac{\rho_{cell}}{\rho_{fluid}} - 1\right)\left(\vec{\omega}^2 r\right) \tag{1.13}$$

Here, ωis an angular velocity, and r is the distance from the axis of rotation of the frame. Later in the chapter 2, we characterize and optimize the angular velocity to control the terminal velocity of cells and time-of-flight required to place cells next to dams and microwells.

Magnetophoresis

In the chapter 3, nickel microparticles are introduced as carriers of protein markers for using as standards for protein sizing. To actively settle the microparticles in the microwells, we applied an applied, external magnetic field using a permanent magnet. The dominant forces for the active microparticle settling are the magnetic, gravity, and drag forces (Figure 1.2C).

$$6\pi a\rho\nu\vec{U} = \frac{4}{3}\pi a^3\left(\rho_{cell} - \rho_{fluid}\right)\vec{g} + \left(\vec{m}\cdot\nabla\right)\vec{B} \tag{1.14}$$

Here, m is the magnetic moment, and B is the magnetic field. Under the influence of an applied magnetic field, the electrostatic forces from surface-charged particles are generated yet only considered to be significant when the distance between particles are less than 10 nm [27, 28].

Electrophoresis

Electrophoresis is a method of separation of proteins by sieving proteins through a gel or a fluid by applying an electric field. In response to the potential field in the colloidal solution, an electric double layer (EDL) around the proteins is formed with a debye length (λ), where an excess of counterions and a deficiency of co-ions exist. Under an electric field, two main forces applied to the proteins are drag and electric (Coulomb) forces (Figure 1.2D). Balancing these forces, we get a particle velocity:

$$6\pi\rho\nu a\vec{U} = q\vec{E} \tag{1.15}$$

$$\vec{U} = \frac{q\vec{E}}{6\pi a\rho\nu} \tag{1.16}$$

Here, q is the net charge on protein, E is the electric field.

When the protein radius (a) is greater than the debye length, curvature effects on the EDL can be ignored, and we can relate the particle velocity equation with the Helmholtz-Smolochowski equation to obtain an electrophoretic mobility:

$$\vec{U} = -\frac{\epsilon\zeta\vec{E}}{\rho\upsilon} = -\mu_E\vec{E} \tag{1.17}$$

$$\mu_E = \frac{\epsilon\zeta}{\rho\nu} = \frac{q}{6\pi a} \tag{1.18}$$

Here, ε is permittivity and ζ is electric potential. Of note, the electrophoretic velocity is directly proportionally to the protein net charge and inversely proportional to the particle radius. Using this electrokinetic principle, proteins can be analyzed by separating based on molecular mass (size) or isoelectric point (charge).

Diffusion

In cells, Brownian motion is neglected because the average mammalian cell diameter is in micron range. On the other hand, Brownian motion, significantly affects small particles like proteins, which have a diameter ¡ 10 nm. Down a concentration gradient, the proteins diffuse in a distance proportional to the square root of the diffusion time. Driven by the thermal energy, Stokes-Einstein equation is used to describe diffusion in the low Re number:

$$F_{thermodynamic} = F_{drag} \tag{1.19}$$

$$-\frac{k_B T}{c}\vec{\nabla}c = 6\pi\rho v a\vec{U} \tag{1.20}$$

Where c is protein concentration, k_B is Boltzmann constant, and T is temperature. Because the mean protein velocity (U) can be described as the ratio of flux (J) to the protein concentration, we can apply the second Fick law to get the diffusion coefficient (D) in terms of thermodynamic and viscous parameters:

$$\vec{J} = -D\vec{\nabla}c = \vec{U}c \tag{1.21}$$

$$\vec{J} = -D\vec{\nabla}c \tag{1.22}$$

$$-\frac{k_B T}{c}\vec{\nabla}c = 6\pi\rho v a\frac{\vec{J}}{c} \tag{1.23}$$

$$\frac{k_B T}{c}\vec{\nabla}c = 6\pi\rho v a\frac{D\vec{\nabla}c}{c} \tag{1.24}$$

$$D = \frac{k_B T}{6\pi\rho v a} \tag{1.25}$$

For designing processes in the open microfluidic format, diffusion affects the detection limit and the resolution of protein separation. More specifically in the single-cell electrophoretic assay, timescales for protein solubilization and electromigration and buffer temperature are carefully considered to ensure that the proteins are not too diffused out into the solution below the limit of detection.

Separation Resolution

Diffusion drives dispersion of protein peaks, thereby lowering the resolution of detecting proteins with different molecular sizes or isoelectric points. Separation resolution is a common metric in analytical chemistry to describe how well two protein peak distributions are separated. The separation resolution (SR) is defined as:

$$SR = \frac{\Delta x}{2\left(\sigma_1 + \sigma_2\right)} \tag{1.26}$$

where δx is the center-to-center distance between the protein peaks and σ is the peak width. The protein peak width (σ) is affected by the injection width (σ_o) and the variance of the position, caused by diffusion (2Dt).

$$\sigma = \sigma_o + 2Dt \tag{1.27}$$

In electrophoresis, the center-to-center distance (Δx) translates into the difference of electrophoretic mobilities (Δμ) between two proteins peaks for a given time (Δt) of applied electric field (E):

$$\Delta x = \Delta\mu E \Delta t \tag{1.28}$$

In analytical chemistry, two species are typically considered to be resolved when the SR = 1, or only overlapping 2% each other.

Protein Sizing by Electrophoresis

Protein molecular sizes can be predicted by measuring electromigration of uniformly charged proteins. The addition of anionic detergent, such as sodium dodecyl sulfate, provides a uniform charge-to-mass ratio to proteins. When the uniformly charged and denatured proteins are electrophoresed through a sieving matrix, Ferguson analysis can be used to estimate unknown molecular sizes from the log-linear regression relationship between the known molecular sizes and the known protein electromigration [29]:

$$\log(\mu E t) = -kT \tag{1.29}$$

Here, k represents a retardation factor (analogous to the translational tensor in the drag force), and T represents the density of the sieving matrix. In the chapter 3, we extensively use the Ferguson analysis to investigate protein sizing performance in the single-cell electrophoretic assay.

Bibliography

1. Manna, S. & Holz, M. K. Tamoxifen Action in ER-Negative Breast Cancer. *Signal Transduction Insights.* ISSN: 1178-6434. doi:10.4137/STI.S29901 (2016).
2. Stewart, J. *et al.* Estrogen and progesterone receptors: Correlation of response rates, site and timing of receptor analysis. *Breast Cancer Research and Treatment* **2,** 243–250. ISSN: 0167-6806 (1982).
3. Johnston, S. R., Dowsett, M & Smith, I. E. Towards a molecular basis for tamoxifen resistance in breast cancer. *Annals of oncology : official journal of the European Society for Medical Oncology* **3,** 503–11. ISSN: 0923-7534 (1992).
4. Shou, J. *et al.* Mechanisms of tamoxifen resistance: Increased estrogen receptor-HER2/neu cross-talk in ER/HER2-positive breast cancer. *Journal of the National Cancer Institute.* ISSN: 00278874. doi:10.1093/jnci/djh166 (2004).
5. De Gramont, A. *et al.* Pragmatic issues in biomarker evaluation for targeted therapies in cancer. *NATURE REVIEWS — CLINICAL ONCOLOGY* **12,** 197–212 (2014).
6. Drucker, E. & Krapfenbauer, K. *Pitfalls and limitations in translation from biomarker discovery to clinical utility in predictive and personalised medicine* tech. rep. (2013). doi:10.1186/1878-5085-4-7. <http://www.epmajournal.com/content/4/1/7>.
7. Fakhri, G. B. *et al.* Concordance between Immunohistochemistry and Microarray Gene Expression Profiling for Estrogen Receptor, Progesterone Receptor, and HER2 Receptor Statuses in Breast Cancer Patients in Lebanon. *International journal of breast cancer* **2018,** 8530318. ISSN: 2090-3170 (2018).
8. Griggs, J. J. *et al.* Discordance between original and central laboratories in ER and HER2 results in a diverse, population-based sample. *Breast cancer research and treatment* **161,** 375–384. ISSN: 1573-7217 (2017).
9. Kim, J. J., Sinkala, E. & Herr, A. E. High-selectivity cytology via lab-on-a-disc western blotting of individual cells. *Lab on a Chip* **17,** 855–863. ISSN: 1473-0197 (2017).
10. Rettig, J. R. & Folch, A. Large-scale single-cell trapping and imaging using microwell arrays. *Analytical Chemistry* **77,** 5628–34. ISSN: 00032700 (2005).
11. Revzin, A. *et al.* Development of a microfabricated cytometry platform for characterization and sorting of individual leukocytes. *Lab on a Chip* **5,** 30–7. ISSN: 14730197 (2005).

12. Di Carlo, D., Aghdam, N. & Lee, L. P. Single-cell enzyme concentrations, kinetics, and inhibition analysis using high-density hydrodynamic cell isolation arrays. *Analytical Chemistry* **78,** 4925–30. ISSN: 00032700 (2006).

13. Wood, D. K. *et al.* Single cell trapping and DNA damage analysis using microwell arrays. *Proceedings of the National Academy of Sciences* **107,** 10008–10013. ISSN: 0027-8424 (2010).

14. Gierahn, T. M. *et al.* Seq-Well: Portable, low-cost rna sequencing of single cells at high throughput. *Nature Methods* **14,** 395–398. ISSN: 15487105 (2017).

15. Yuan, J. & Sims, P. A. An Automated Microwell Platform for Large-Scale Single Cell RNA-Seq. *Scientific Reports* **6,** 1–10. ISSN: 20452322 (2016).

16. Duncombe, T. A. *et al.* Hydrogel Pore-Size Modulation for Enhanced Single-Cell Western Blotting. *Advanced Materials.* ISSN: 15214095. doi:10.1002/adma.201503939 (2016).

17. Hughes, A. J. *et al.* Single-cell western blotting. *Nature Methods* **11,** 749–755. ISSN: 1548-7091 (2014).

18. Rosenthal, A., Macdonald, A. & Voldman, J. Cell patterning chip for controlling the stem cell microenvironment. *Biomaterials* **28,** 3208–16. ISSN: 01429612 (2007).

19. Doh, J., Kim, M. & Krummel, M. F. Cell-laden microwells for the study of multicellularity in lymphocyte fate decisions. *Biomaterials* **31,** 3422–8. ISSN: 01429612 (2010).

20. Collins, A. R. The comet assay for DNA damage and repair: principles, applications, and limitations. *Molecular Biotechnology* **26,** 249–61. ISSN: 1073-6085 (2004).

21. Yang, L. *et al.* Single-cell, multiplexed protein detection of rare tumor cells based on a beads-on-barcode antibody microarray. *Analytical Chemistry* **88,** 11077–11083. ISSN: 15206882 (2016).

22. Varadarajan, N. *et al.* A high-throughput single-cell analysis of human CD8+ T cell functions reveals discordance for cytokine secretion and cytolysis. *Journal of Clinical Investigation* **121,** 4322–4331. ISSN: 0021-9738 (2011).

23. Kang, C. C. *et al.* Single cell-resolution western blotting. *Nature Protocols.* ISSN: 17502799. doi:10.1038/nprot.2016.089 (2016).

24. Kang, C. C. *et al.* Single-cell western blotting after whole-cell imaging to assess cancer chemotherapeutic response. *Analytical Chemistry* **86,** 10429–10436. ISSN: 15206882 (2014).

25. Kang, C.-C. *et al.* Electrophoretic cytopathology resolves ERBB2 forms with single-cell resolution. *npj Precision Oncology* **2,** 10. ISSN: 2397-768X (2018).

26. Sinkala, E. *et al.* Profiling protein expression in circulating tumour cells using microfluidic western blotting. *Nature Communications* **8,** 14622. ISSN: 2041-1723 (2017).

27. Plouffe, B. D., Murthy, S. K. & Lewis, L. H. *Fundamentals and application of magnetic particles in cell isolation and enrichment: A review* 2015. doi:10.1088/0034-4885/78/1/016601. arXiv: NIHMS150003.

28. Bartlett, P. N. *Bioelectrochemistry : fundamentals, experimental techniques and applications* 478. ISBN: 9780470843642. <https://www.wiley.com/en-us/Bioelectrochemistry+{\%}3A+Fundamentals{\%}2C+Experimental+Techniques+and+Applications-p-9780470843642> (John Wiley & Sons, 2008).

29. Ferguson, K. A. Starch-gel electrophoresis–application to the classification of pituitary proteins and polypeptiedes. *Metabolism: clinical and experimental* **13,** 985–1002. ISSN: 0026-0495 (1964).

Chapter 2

High-selectivity cytology via lab-on-a-disc western blotting of individual cells

Material adapted from: Kim JJ, Sinkala E, Herr AE. High-selectivity cytology via lab-on-a-disc western blotting of individual cells. Lab on a Chip, 2016; doi: 10.1039/C6LC01333C

2.1 Introduction

Immunocytochemistry (ICC) and immunohistochemistry (IHC) are workhorse immunoassays routinely employed for assessing cancer grade from biopsy samples. Single-cell resolution is important, as the degree of cellular heterogeneity can provide insight into cancer diagnosis [1–3], prognosis [4], and the selection of therapeutic regime [5–7]. Yet, in these cell-based assays, multiplexing is constrained to a sub-set of 4-5 protein targets per cell [8]. Selectivity is limited by unavailable immunoreagents and poor immunoreagent performance, which can yield substantial off-target and background signals [9, 10]. Deep profiling of protein-mediated signalling would complement conventional clinical protein assays as well as supplement single-cell resolution genomics and transcriptomics.

In contrast to immunoassays (i.e., single-stage protein assays), multi-stage protein assays enhance selectivity by prepending a protein sizing (electrophoresis) stage to the downstream immunoassay stage. These so-called immunoblots report both protein molecular mass and immunoreactivity, thus offering more comprehensive information on both the targets and any confounding signals. While providing powerful analytical specificity, contemporary slab-gel western blotting requires pooling of cells to achieve sufficient analytical sensitivity [11]. Slab-gel western blotting typically requires 10^5 - 10^6 cells, thus making the assay ill-suited for analysis of small volume biopsies. More broadly, the pooling of cell populations obscures cell-to-cell variation in protein expression. To overcome this limitation, our recent studies report microfluidic single-cell western blotting (scWestern)[12–15]. While promising, the analytical

module has not yet been integrated with an upstream cell handling module suitable for preparation of dissociated tumour cells, as is needed for clinical impact.

That said, downstream cellular analyses have been successfully integrated with upstream cell preparation using microfluidic design. In one class of microfluidic cell preparation tools, a pressure-driven flow directed cell suspensions through microscale features (dams) that passively trapped (immobilized) individual cells for subsequent *in-situ* enzymatic activity assays [16, 17]. In order to yield 200 immobilized single cells, starting populations of 300,000 cells (100 µL of ~ 3 x 10^6 cells/mL) were required due to 50% trapping single-cell efficiencies [16].

Another class of cell handling tools utilized applied fields and field gradients. In one example, local magnetic fields enriched antibody-functionalized magnetic beads, which isolated cells expressing specific surface receptor proteins from suspension [18]. Dependent on antibody specificity and sensitivity, this bulk process of cell capture usually required > 1 x 10^6 cells [18, 19]. While useful for enrichment, antibody binding could alter cellular gene expression [20]. In a label-free variant, dielectrophoretic (DEP) forces, created by non-uniform electric fields based on dielectric properties, finely controlled the spatial location of individual cells [21–23]. Embedded electrodes and low conductivity buffers limited the damage to cell membranes or DNA [24–26]. Light has also been used to tune conductivity, thus generating local electric field gradients useful for non-contact manipulation of cells [21]. However, before DEP, cell losses due to dead volumes and a driving pressure-driven flow were substantial [22, 23]. Despite a slow flow rate (10 µL/min), high cell concentrations (5 x 10^5 — 1 x 10^6 cells/mL) were needed to settle hundreds of cells for viability testing and immunostaining [22, 23, 27]. Overall, existing single-cell protein assays, which apply hydrodynamic or external-field techniques, require at least 1000 cells as a starting number of cells [15, 28–30].

Owing to our interest in robust integration of sparse cell handling and subsequent scWestern analysis, we explore centrifugation for cell preparation. So-called lab-on-a-disc tools readily maneuver sparse cell samples with < 10% cell handling losses [31, 32]. The centrifugal force is nearly independent of buffer properties and compatible with subsequent electrophoretic analysis of cells from samples [31, 33, 34]. With minimal usage of cell sample and reagents, we developed a low-loss and rapid lab-on-a-disc device that measures proteins from single cells. Here, we report on the design, demonstration, and characterization of a centrifugal cell preparation module to direct cells from sparse starting cell populations to single-cell occupancy of microwells for subsequent scWestern.

2.2 Materials and Methods

SU-8 Soft Lithography

A two-layer polyacrylamide gel was polymerized against a silicon wafer with SU-8 features. The bottom layer of the gel houses chamber walls and dams, and the top layer houses microwell pillars. A mechanical grade silicon wafer (University Wafers) was pre-treated with isopropanol and acetone to clean the wafer surface. An 80-µm SU-8 3050 (Y311075; MicroChem) layer was coated by spinning at 1750 RPM for 30 s and soft baked at 95 °C for 30 min. To create an SU-8 mold of the chambers, the wafer was exposed to UV (Model 200IR, OAI) at 40 mW/cm^2 for 6 s through a Mylar mask (CAD/Art Services), which has a transparent area with the chamber design. After a post-exposure baking at 65 °C for 1 min and 95 °C for 5 min, another layer of 40-µm SU-8 3050 was spin-coated at 4000 RPM for 30 s on top of the previous SU-8 layer to make microwell posts. Then, the wafer was soft baked at 95 °C for 15 min, and exposed to UV (40 mW/cm^2, 5 s) under another Mylar mask with the microwell design. Followed by post-exposure baking (65 °C for 1 min, 95 °C for 5 min), the wafer was submerged in SU-8 developer (Y020100; Microchem) and rinsed with 2-propanol. In the end, the wafer was composed of an 80- µm bottom layer with chamber posts and a 40-µm top layer with microwell post. Before casting a polyacrylamide gel, the wafer was coated with 100 µL hydrophobic dichlorodimethylsilane (DCMC, 440272; Sigma-Aldrich) via vapor-deposition for 40 min under vacuum. The SU-8 molds thickness was measured by using a surface profiler (Sloan Dektak 3030) with a 0.10 mN stylus force.

Device Materials and Fabrication

Two chambers with microwells and dams were fabricated on a standard microscope glass slide by casting a polyacrylamide gel against the wafer with SU-8 features. The final gel with 8 %T and 2.7 %C was chemically polymerized from a stock 30 %T, 2.7 %C acrylamide/bis-acrylamide solution (A3699; Sigma) with a 3 mM N-[3-[(3-Benzoylphenyl)formamido]propyl] methacrylamide (BPMAC, custom synthesized by PharmAgra Laboratories) and 75 mM Tris HCl pH 8.8 (T1588; Teknova). Ammonium persulfate (A3678; Sigma) and TEMED (T9281; Sigma) were used as reagents for chemical polymerization. The dried gels thickness was measured by using Sloan Dektak 3030. To hold the cell suspension inside each chamber during centrifugation, a polyester film (GelBond; Lonza) was used as a lid (Figure 2.1). Holes were punched in the lid using a revolving hole punch (Herm Sprenger, 10809). A liquid superglue (Loctite) was applied along the edges between the glass slide and the lid to act as a seal.

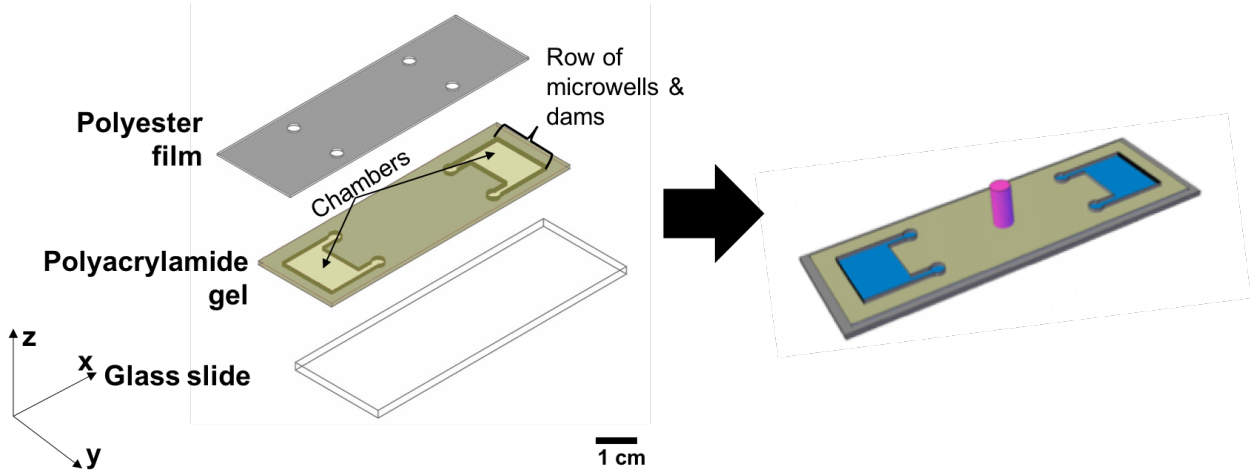

Figure 2.1: Lab-on-a-disc device consists of a polyester film, polyacrylamide gel, and a microscope glass slide. The polyester lid encloses a cell suspension inside chambers during centrifugation. The microscope glass slide functions as a base support for the polyacrylamide gel and allows to image cells and proteins during the device operation.

Cell Line and Microbead Preparation

A U251 glioblastoma cell line with stable expression of turboGFP (U251-GFP) was kindly provided by Prof. S. Kumars Laboratory at the University of California, Berkeley. The U251-GFP cells were cultured in high glucose Dulbecco's Modified Eagle Medium (Life Technologies, 11965), supplemented with 10% of fetal bovine serum (JR Scientific), 1% penicillin/streptomycin (Invitrogen, 15140122), 1 mM sodium pyruvate (Life Technologies, 11360-070), and 1 MEM nonessential amino acids (Life Technologies, 11140050). The cell line was incubated at 37 °C with 5% CO2. For cell detachment from a tissue-culture flask, U251-GFP cells were incubated with 0.05% trypsin-EDTA (Gemini, 400-150) at 37°C for 5 min. Detached cells were counted with a hemocytometer and diluted accordingly with ice-cold 1x PBS. For cell-viability testing, 1 mg/mL propidium iodide (P1304MP) was diluted 1:100 with cells in 1x PBS. The SEM cell line, a B cell precursor leukemia, was generously received from Prof. R. Stams Laboratory at the Erasmus University Rotterdam via Deutsche Sammlung von Mikroorganismen und Zellkulturen GmbH (DSMZ).

The SEM cells were cultured in RPMI 1640 medium (ThermoFisher Scientific, 11875093) with 10% fetal bovine serum (JR Scientific) and 1% penicillin/streptomycin (Invitrogen, 15140122). The SEM cell line was maintained in a humidified 37 °C incubator with 5% CO_2. For nucleic acid staining, SEM cells were incubated with 1 µg/mL Hoechst 33342 (ThermoFisher Scientific, H3570) for 10 min. The excess stain was removed by centrifuging the cells at 450 xg for 5 min and aspirating the supernatant. FITC-labeled, 15-µm diameter polystyrene microbeads (Invitrogen, F21010) were used to measure particle drift velocities at different rotational speeds. Before introducing into the lab-on-a-disc device, microbeads

were diluted in 1x PBS and vortexed thoroughly.

Cell Loading Simulation

We simulated the cell loading in a 2D environment using COMSOL Multiphysics version 5.0 (COMSOL Inc.). The device geometry was drawn in AutoCAD (Autodesk, Inc.) and exported to COMSOL. Laminar flow and particle tracing fluid flow physics modules were used. In the fluid flow physics module, material properties of water (density ρof 0.995 g/ml, dynamic viscosity μof 8.90 x 10^{-4} Pa s), no-slip wall boundary conditions, and an average inlet velocity of 0.006 m/s were implemented. In the particle tracing module, one hundred 30-μm particles with a density of 1.050 g/ml were added with a drag force. The drag force was calculated from the fluid flow physics module.

scWestern

Microwells were spaced 160 μm apart and configured with the 1.5 mm gel for scWestern. The microwell post area was increased from 700 μm ^{2} to 3100 μm ^{2}, while maintaining the post height at 40 μm. Also, the microwells were modified from a circular to trapezoidal geometry to increase the microwell area.

After centrifugation, the polyester lid was removed. The device was cut in half for concurrent chemical lysis and electrophoresis in scWestern. To dice the slide in half, we used a laser cutter (H-Series Desktop CO_2 Laser, Full Spectrum Laser). 1% SDS (Sigma, L3771), 0.1% v/v Triton X-100 (Sigma, X100), 0.25% sodium deoxycholate (Sigma, D6750), 12.5 mM Tris, and 96 mM glycine (Bio-Rad, 161-0734) were combined to make a Radioimmunoprecipitation-like (RIPA-like) buffer. 10 ml of the RIPA-like buffer was slowly poured over the device for 25 s. Then, an electrical field of 40 V/cm was applied across the slide to electrophorese proteins for 25 s. Immediately after the protein electrophoresis, we exposed the slide to UV at 100% power for 45 s (Hamamatsu, Lightningcure LC5) to immobilize proteins. The slide was washed with 1x TBS with Tween 20 (TBST, Affymetrix, 77500) before antibody probing. Primary and secondary antibodies were diluted with 1x TBST with 2% BSA. At room temperature, 0.1 g/l of primary antibodies and 0.05 g/l of secondary antibodies were used to probe the slide for 2 h. Between and after each probing step, 1x TBST was used as a washing buffer. Then, the slide was dried and imaged under a fluorescence microarray scanner (Genepix, 4300A). A half-slide seats stably on the four-pin mount located in the sample chamber of the imaging instrument. For Genepix laser settings, PMT gain was set at 500, power at 50%, and focus position at 10 μm for all fluorescence channels. The slide was held in place by four prongs inside Genepix. Primary GAPDH, β-Tubulin, turboGFP, STAT3, and H3K79me2 antibodies were purchased from Sigma (SAB2500450), Abcam (ab6046), Pierce (PA5-22688), Cell Signalling (9139), and Abcam (ab3594), respectively. Anti-goat antibody with Alexa Fluor 555 (ThermoFisher, A-21432), anti-mouse antibody with Alexa Fluor 594

(A-11032), and anti-rabbit antibody conjugated with Alexa Fluor 647 (A-21245) were used as secondary antibodies.

Image Acquisition

An inverted microscope (Olympus IX71) equipped with a motorized stage (Applied Scientific Instrumentation, MS-2000) and an X-cite mercury light lamp source (Lumen Dynamic) imaged cells. 10x-objective brightfield and fluorescence images were taken with the iXon+ EMCCD camera (Andor Technology Ltd.) and stitched together with Metamorph software (Molecular Devices). Standard FITC/GFP and DAPI filter cubes were used to detect U251-GFP and DAPI-stained SEM cells, respectively.

Image Analysis and Quantitation

All images were analysed by ImageJ 1.49v (NIH). Cell diameters were estimated by adjusting image threshold and using the built-in ImageJ particle analyser command. In scWestern, protein peaks were quantified by performing Gaussian fitting with an R-squared value > 0.7. Fluorescence intensity was obtained by summing the area under curve (AUC). The AUC and separation resolution were calculated by using our in-house MATLAB (R2015b) code [15]. Statistical analyses were performed using EXCEL and existing MATLAB functions.

2.3 Results and Discussion

Integrating Centrifugal Cell handling with scWestern Analysis

We designed a microfluidic lab-on-a-disc device that integrates our scWestern with a new bulk approach to handle sparse, heterogeneous cell samples (Figure 2.2A). We sought to minimize cell loss during device operation and analysis of the sparse starting populations of cells. The analytical module comprises an array of microwells directly molded into a photo-active polyacrylamide gel layered onto a glass microscope slide. The scWestern blot isolates a single cell in a microwell, chemically lyses *in-situ*, and injects the lysate electrophoretically through the microwell walls and into the molecular sieving matrix (Figure 2.2B, Figure 2.3). After the completion of electrophoresis, the proteins are covalently immobilized onto the hydrogel (photo-immobilization) and probed with a series of antibodies to report protein target identity.

The integrated cell handling module consists of two chambers, flanked by an array of 100 microwells, with an inlet at the axis of rotation (Figure **??**A). As described, the microwells isolate cells for subsequent scWestern. To localize cells to the microwells, we use a two-layer polyacrylamide gel with microwells molded into the bottom layer and U-shaped cell trapping dams located above and around each microwell. Cell trapping dams have been used

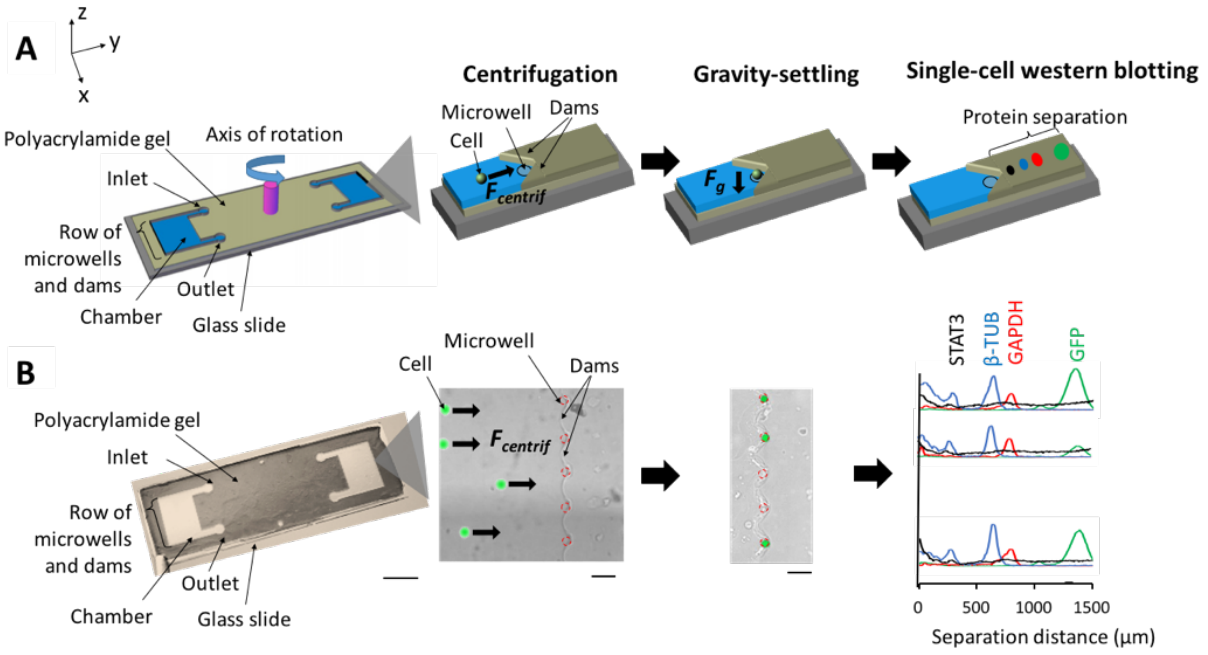

Figure 2.2: Lab-on-a-disc couples the handling of sparse cell samples with single-cell western blotting (scWestern). The microfluidic design (A) and device (B) consists of two chambers with dams and arrays of microwells that are built by patterning a polyacrylamide gel on a microscope glass slide, sandwiched with a polyester lid. After an injection of 1 — 20 µl of cells via an inlet, the device is centrifuged on an upright spinner. In a rotation frame of reference, the centrifugal force leads to migration of the cells towards the microwells. Subsequently, gravity sediments the cells into the microwells. Finally, the patterned polyacrylamide gel with single cells is used as a medium for scWestern. Scale bar left, 1 cm. Scale bars middle and right, 100 µm.

to physically trap single cells under a pressure-driven flow or centrifugation [16, 17]. Here, we develop a two-layer fabrication process using the same hydrogel material that is used for the electrophoresis and immunoprobing steps of the scWestern (Figure 2.3). Then, the lab-on-a-disc device is placed in the spin coater (SoftLithoBox; Elveflow) for centrifugation. Once centrifugation drives cells into the U-shaped dams on the periphery of the fluidic chamber, each cell then gravity settles into the microwell directly below. To create fully enclosed fluidic chambers, the device is capped with a layer of transparent polyester film (GelBond). Once cells are seated in the microwells, this lid layer is removed, and the lysis buffer is applied to initiate the analytical stage of the assay (Figure 2.2, Figure 2.3).

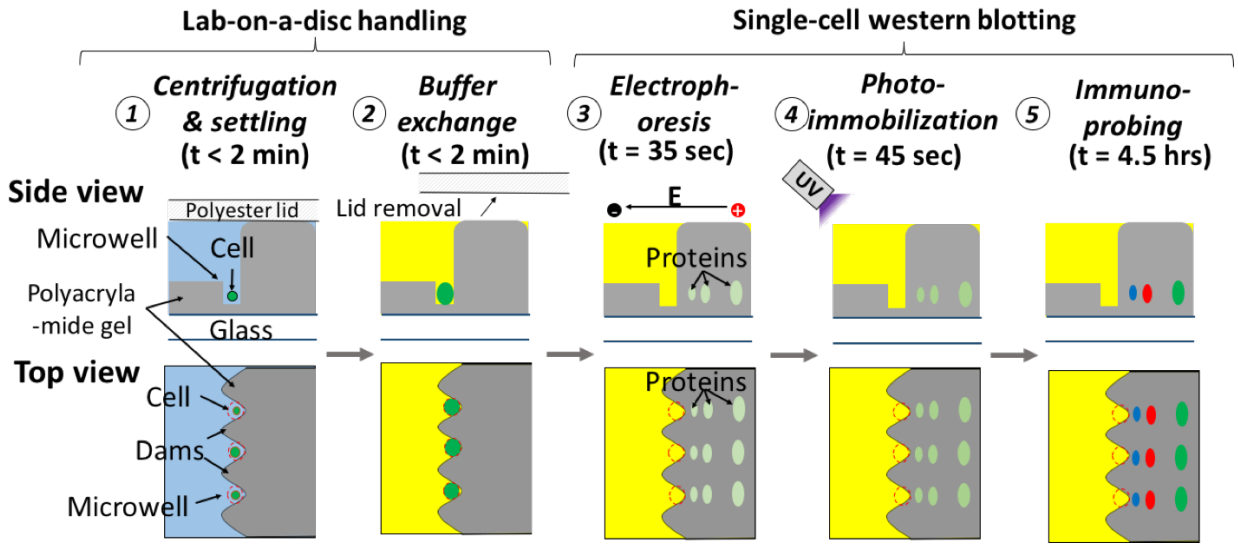

Figure 2.3: Schematic workflow of the lab-on-a-disc handling and scWestern blotting. 1: Centrifugal force and dams place single cells to microwells. Subsequently, cells settle in microwells by gravity. 2: After opening the polyester lid and cutting the device in half, a chemical lysis and electrophoretic buffer is poured in the device. Steps 3 — 5 entail scWestern blotting. 3: An electric field (40 V/cm) is applied for protein separation. 4: UV is applied to activate benzophenone moieties, incorporated in the gel, for protein capture. 5: Fluorescent antibodies are introduced to probe for target proteins.

Characterization of a lab-on-a-disc design for cell handling

By using a lab-on-a-disc approach to localize cells to the microwells flanking the fluidic chambers, we sought to understand three operational aspects of the device and centrifugation scheme: (i) cell drift velocities across the fluidic chambers, (ii) suitable centrifugation forces for moving cells to the microwell array, and (iii) final uniformity of the cell distribution along the linear microwell array. First, we estimate the drag force expected on a cell migrating in the fluidic chamber under centrifugation. With our device design and a rotational velocity of a 5000 RPM (980 xg), the Reynolds number is $<<1$, so Stokes Law is applied. Although cells do not reach terminal velocities during centrifugation, the radial drift velocity across the chamber is relatively constant and allowed estimates of suitable operating conditions. We calculate and also measure the drift velocities of FITC-labelled polystyrene microbeads (15 µm, 1.06 g/cm ^{3}) under various RPMs and found appreciable agreement between theory and experiment (Figure 2.4A).

Second, we investigate suitable centrifugal conditions for directing mammalian cells to microwells. After 2 min of operation at 2000 RPM (157 xg), 82% of the 15-µm polystyrene microbeads (n = 3 chambers) and 90% of human glioblastoma cells (U251-GFP, 30-µm diameter, n = 5 chambers) are localized to the microwell array (Figure 2.4B, C). Under

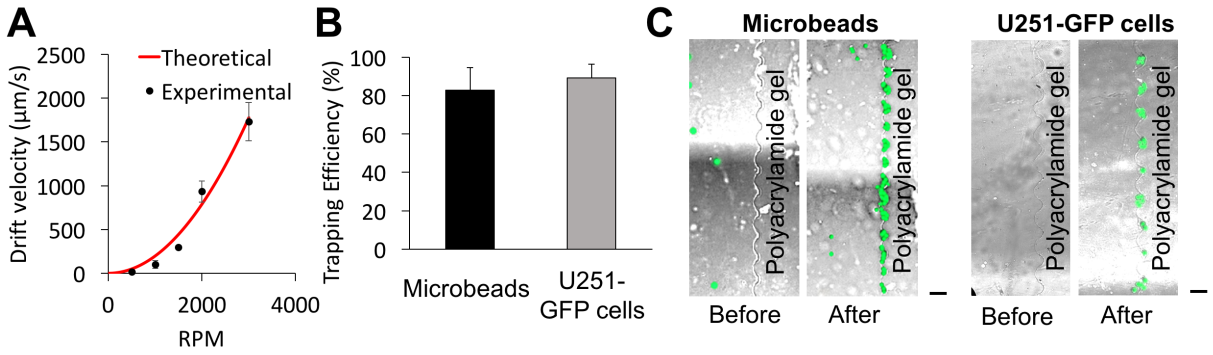

Figure 2.4: Characterization of particle drift velocities as a function of rotational velocity. (A) A plot of theoretical and experimental drift velocities. Based on forces acting on a 15-µm, FITC microbead in a rotational reference frame, drift velocities are calculated to estimate particle velocity. By injecting 3~5 microbeads into the device, microbeads are imaged before and after centrifugation to measure distance and calculate velocities. Theoretical and experimental data follow a similar behavior. (B, C) Measurement of trapping efficiencies and false-color epifluorescence micrographs of microbeads and U251-GFP cells. Centrifugal effect is tested by using FITC microbeads and a U251-GFP cell line. Rotating at 2000 RPM for 2 min, more than 80% of microbeads and U251-GFP cells migrate to microwells. Scale bars, 100 µm.

higher rotational speeds, we observe appreciable cell lysis (e.g., 3000 RPM; 353 xg; 4.15 nN of centrifugal force; Figure 1.5). Cell lysis under these conditions might be attributable to shear forces, as notable cell lysis had been observed under ~1.4 nN of shear force [35]. Cells may be more susceptible to lysis by shear forces than by compressive forces [35, 36]. We further investigated cell viability under the suitable 2000 RPM conditions and observed no dead cells by propidium iodide (PI) stain (Figure 2.5) as well as no visible changes in cell morphology after centrifugation.

Third, we sought to numerically and empirically assess the cell distribution in the fluidic chamber. In a first aspect, we consider a system where capillary flow is utilized for sample introduction into the fluidic chamber. Through the inlet, we applied a microbead suspension (1 - 20 µl of 1x PBS solution) and generated a capillary force by applying a task wipe at the chamber outlet for 1 s (Figure 2.6). Both the COMSOL simulation and empirical results for 15-µm microbeads demonstrated capillary flow as a feasible and passive means to introduce cells across the chamber width (Figure 2.6A). In the experimental study, we observed a similar distribution of cells except with a higher concentration of microbeads near the top wall of the chamber, possibly due to a backflow generated by pressing the task wipe on the outlet port. In a second aspect, after loading and centrifuging the cells (2 min, 2000 RPM), we assessed the final distribution of cells across the flanking microwell array.

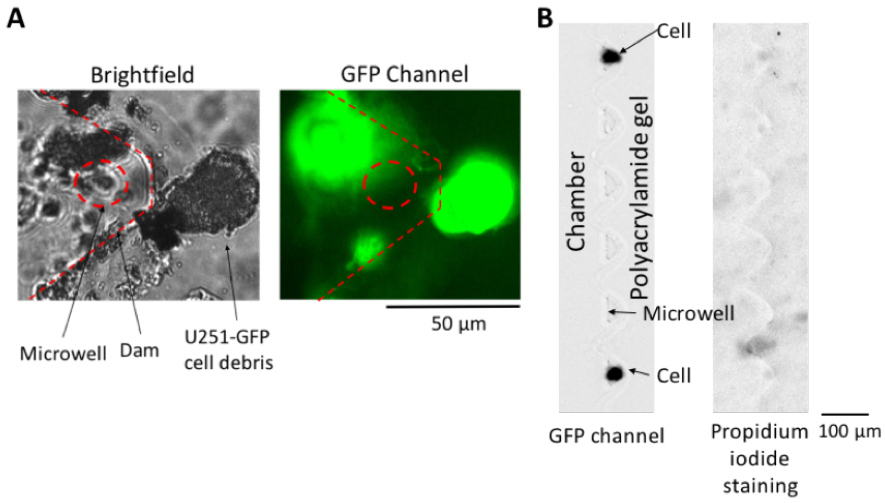

Figure 2.5: Effect of centrifugation on cells is examined at different rotational speeds. (A) Centrifugation at 3000 rpm for 5 min results in a mechanical lysis of U251-GFP cells. Released from cells, GFP protein streaks are observed in polyacrylamide gel. (B) U251-GFP cells are stained with propidium iodide and centrifuged in our device at 2000 rpm for 2 min. Absence of red fluorescence due to the propidium iodide inside the settled cells indicates that cells are viable after centrifugation.

We determined that glioblastoma cells (U251-GFP) settled uniformly across the length of the linear microwell array (Pearsons chi-squared statistic test; 8 devices, 569 cells; Figure 2.6B). A cell-occupancy likelihood is calculated by enumerating cells in each microwell via microscopy, across 8 replicate runs. For a uniform distribution with 569 cells, the expected value for cell-occupancy likelihood for each microwell is 5.69. The chi-squared value, calculated here from 8 devices, is 95.5 which is less than the critical value 120. The analysis suggests that no significant difference exists between the experimental data and a random distribution of cells (95% CI).

Analysis of single-cell settling and cell losses in lab-on-a-disc cell handling

For scWestern, the cell occupancy of each microwell (i.e., number of cells seated in each microwell) has to be one. To characterize the effectiveness of the lab-on-a-disc design for manipulating — and then analysing — individual cells, we first assessed the number of microwells containing individual cells at the end of the preparatory stage. After applying 100 U251-GFP cells and completing the centrifugation based handling (2 min, 2000 RPM), we observed 84% of trapezoidal microwells (n = 8 devices) contained single cells after centrifugation (Figure 2.7). When microwell occupancy exceeded unity, visual inspection suggested

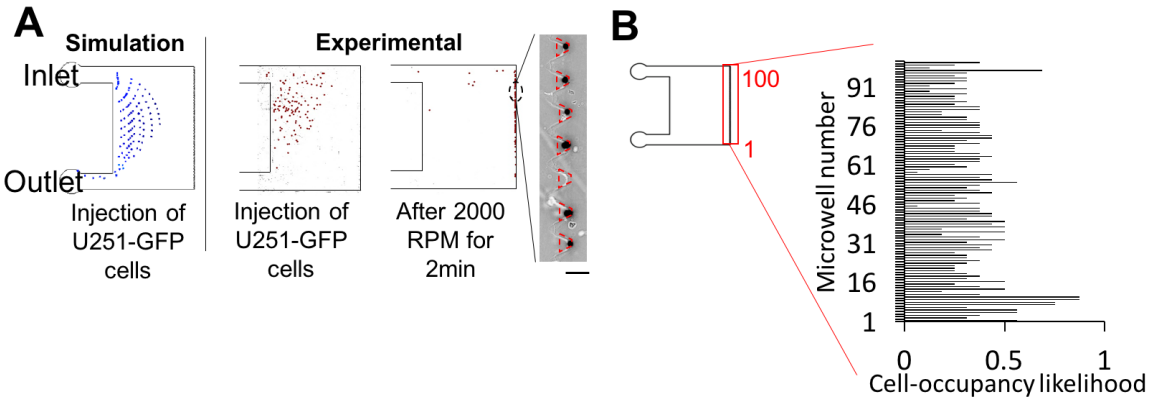

Figure 2.6: Cell loading by capillary force results in a uniform cell distribution across the array of microwells. (A) False-color epifluorescence micrographs of U251-GFP cells during cell loading. Particle tracing simulations show capillary force-based introduction of cells into the fluidic chamber results in uniformly dispersed cells, corroborating empirical results. (B) A plot of cell-occupancy likelihood across the array of microwells. After cell loading, centrifugation is applied for 2 min at 2000 RPM. In 8 replicates with 569 cells, cell-occupancy likelihood is calculated for each microwell. Based on Pearsons chi-squared statistic test, the distribution of cells settled into the microwells does not differ from the anticipated distribution of cells settled randomly without any bias (95% CI). Scale bar, 100 µm.

that cell clumping in the initial suspension was a factor. Next, cell losses during handling were characterized for biospecimens comprised of small numbers of cells. We assessed cell losses for starting populations at and then below 100 cells. To benchmark suitability of the lab-on-a-disc preparatory module, we compared cell losses with a gold-standard of passive-gravity sedimentation into a 2D array of microwells per our previous planar scWestern blot, which was not optimized for handling sparse cell suspensions [13]. Benchmarking with a sample of sparse cells on the 2D microwell array yielded $< 5\%$ single-cell occupancy rate (20 µl of 100 U251-GFP cells; Figure 2.7C), with the vast majority of microwells containing no cells. Cell losses exceeded 95% of the starting population owing to just 1.1% of the device surface area occupied by the microwells. Additionally, the 20-µl cell suspension was evaporated during the first 5 min of the 20-min duration allotted for cell sedimentation.

In contrast, using the integrated lab-on-a-disc cell handling and chamber-flanking microwell array, we observed >70% of cells settled into microwells, even with the starting cell population below 100 cells (Figure 2.7B, n = 4 devices for each case). Single-cell occupancy rates were in the 70% range. The 30% cell loss in our device originated from three processes: cell loading, centrifugation, and lid removal (Figure 1.8). During the cell loading, 7.5% of the total number of cells remained at the cell loading areas (Figure 2.8, n = 5 chambers). Pinched between the gel layer and the polyester lid, the cells were caught at

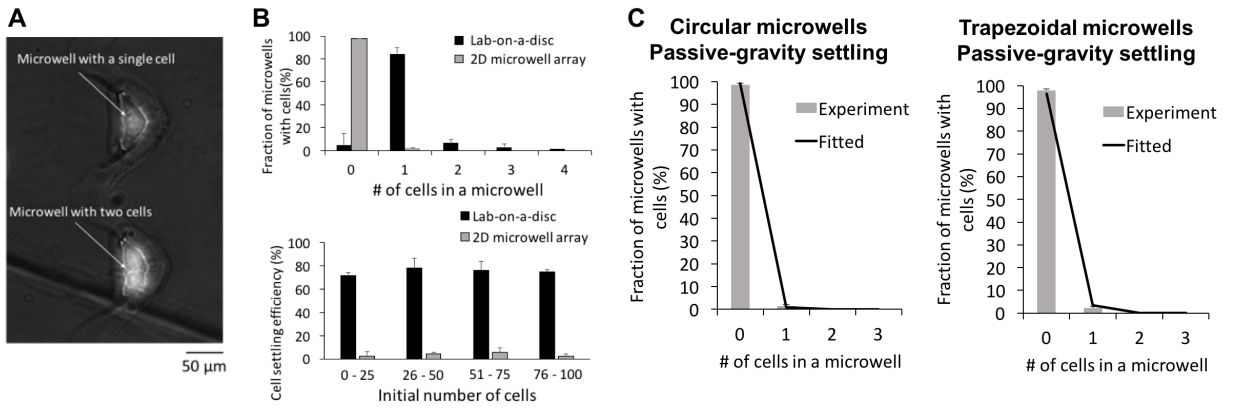

Figure 2.7: Lab-on-a-disc handling enhances single-cell microwell occupancy from sparse cell samples. (A) The cell occupancy of each microwell is determined by combined brightfield and fluorescence inspection. Representative micrographs show 10x-objective fluorescence/brightfield images (100 ms exposure time) of the microwell region just prior to scWestern. (Top) Image of a single cell seated in a microwell and (bottom) image of multiple cells seated in a microwell. Using similar micrographs, we exclude scWestern endpoint protein readouts from microwells housing multiple cells. (B) With less than 100 starting cells, over 80% of microwells are occupied with single cells in the lab-on-a-disc device, as compared to 3% of microwells in the 2D microwell array device with gravity settling [13, 15](n = 4 slides for each case, error bars represent standard deviation). (C) The 2D microwell-array scWestern blotting with passive-gravity settling contains $< 4\%$ of microwells filled with single cells and follows the Poissons distribution with 100 cells (n = 4 slides for each case, $\lambda = 0.002$ for circular, 0.01 for trapezoidal).

the inlet and outlet boundaries during capillary loading and centrifugation (Figure 2.8A). During centrifugation, 1.2% of the injected cells travelled to the side walls of the chambers, rather than being directed to microwells (Figure 2.8A, n = 5 chambers). Lastly, the major cell loss took place during lid removal prior to the application of lysis buffer (Figure 2.8B, n = 6 chambers). Despite dams localizing cells above microwells during centrifugation, cells that were not settled in microwells were washed away. The trapezoidal microwell geometry increases the chances that a cell will sediment into a microwell after being trapped at a dam feature. As compared to a circular microwell, the trapezoidal microwell enhances the dam proximal microwell area by conforming to the dam footprint more closely than is possible with a circular geometry. In comparison to circular microwells, the trapezoidal microwells reduced the cell loss from 44% to 17% (Figure 2.8B).

Having established the operational parameters for integrating the lab-on-a-disc preparatory module with the scWestern, we sought to explore a novel aspect of the device physics: to operate the centrifugal cell preparation module in a filtering-like mode based on differences

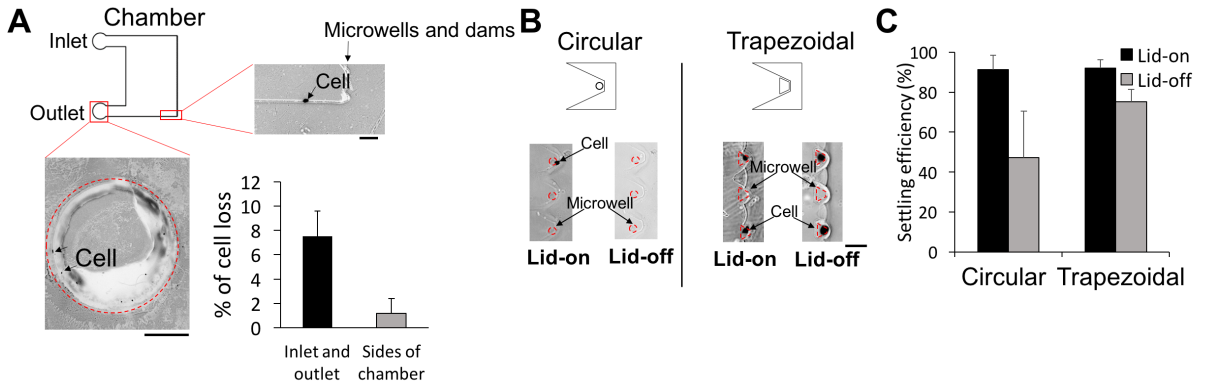

Figure 2.8: Cell losses are characterized during lab-on-a-disc handling and minimized by matching the microwell and dam geometries. (A) Epifluorescence micrographs of U251-GFP cells in cell loading areas and side walls of the chamber. Cell losses are from (i) cell loading, where 7.5% of total cells are immobilized at the inlet and the outlet borders, (ii) centrifugation, in which 1.2% of the loaded cells migrate to side walls of the chambers (n = 5 chambers for each case). Scale bar bottom, 500 µm. Scale bar top right, 100 µm. (B) Epifluorescence micrographs of cells in microwells before and after lid removal. 44% of total cells are partially settled in circular microwells and subsequently dislodged during lid removal for buffer exchange (n = 6 chambers). Increasing the microwell area from 710 mm^2 to 3200 mm^2 and modifying to a trapezoidal shape reduced the cell loss to 16.9% of total cells (n = 6 chambers). (C) Overall, 47.2% and 75.2% of total cells are settled in circular and trapezoidal microwells before scWestern, respectively.

in drift velocity. The time-of-flight to microwell varies among cells with different diameters because the drift velocity is proportional to the square of the cell diameter (Equations 2.1 – 2.3, Figure 2.9A):

$$U_{drift} = \frac{dx}{dt} = \frac{x\omega^2(\rho_{cell} - \rho_{liq})d_{cell}^2}{18\mu} \tag{2.1}$$

$$\int_{r_1}^{r_2} dx \frac{18\mu}{x\omega^2(\rho_{cell} - \rho_{liq})d_{cell}^2} = \int_0^t dt \tag{2.2}$$

$$t_1 = \frac{18\mu}{x\omega^2(\rho_{cell} - \rho_{liq})d_{cell}^2} ln(\frac{r_2}{r_1}) \tag{2.3}$$

U_{drift} = cell drift velocity, µ= dynamic viscosity, ω= rotational velocity, r_1 = 0.023 m, r_2 = 0.033 m, ρ_{liq} = density of 1x PBS (0.995 g/ml), SEM cell diameter (d_{cell} = ~ 6 µm) and density (ρ_{cell} = 1.1 g/ml), U251-GFP cell diameter (d_{cell} = ~30 µm) and density (ρ_{cell} = 1.05 g/ml).

To address this question, we considered a 3:1 mixed population comprised of two cell types: small DAPI-stained cells from a mouse leukocyte cell line (SEM, ~6 µm diameter; = 1.1 g/ml [37, 38]) and large GFP cells from a glioblastoma cell line (U251-GFP, ~30 µm diameter, = 1.05 g/ml [37]). The larger U251-GFP cells were anticipated to have a higher drift velocity than the SEM cells, giving the U251-GFP cells a shorter time-of-flight to the microwell array (Figure 2.9B). Based on calculations with cell densities and diameters, we centrifuged our platform for 2 min at 1000 RPM to preferentially bias settling of the U251-GFP cells in the microwells, with smaller SEM cells confined closer to the fluid inlet (Figure 2.9A-C). With DAPI and GFP fluorescence channels, a visual inspection of microwells after the lid removal indicates that more than 60% of the shorter time-of-flight U251-GFP cells were settled in microwells, while $< 5\%$ of the longer time-of-flight SEM cells were settled into the microwells (Figure 2.9C, n = 5 chambers). The scWestern reports that microwells housing U251-GFP cells are devoid of SEM cells (Figure 2.9D).

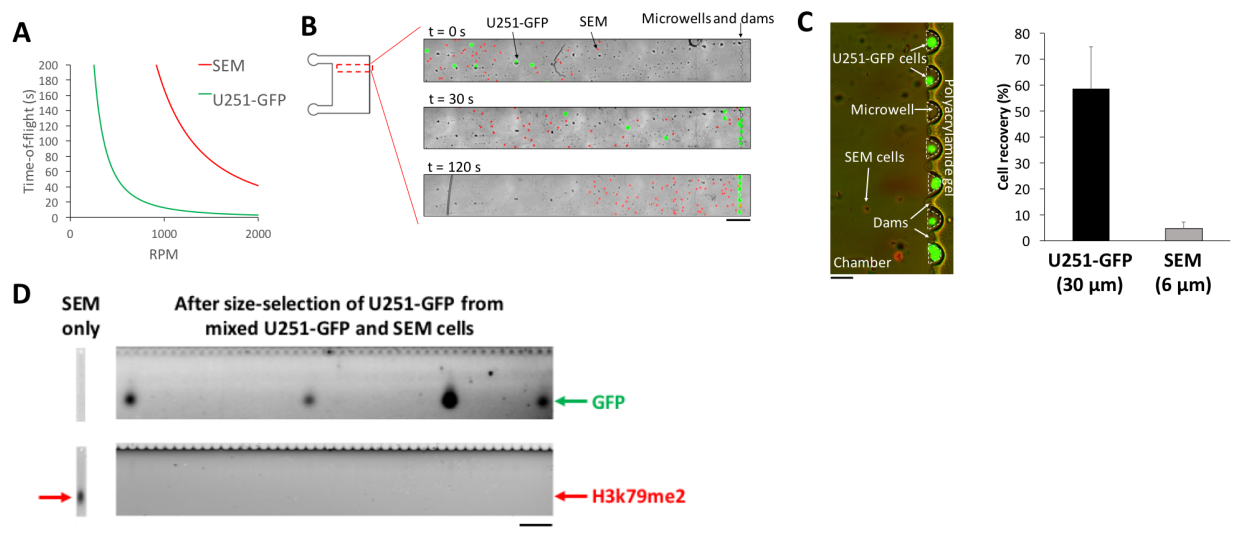

Figure 2.9: Size filtration of leukocyte (SEM) cells from glioblastoma (U251- GFP) by adjusting cell time-of-flight during centrifugation. About 400 SEM cells are spiked into a solution of 100 U251-GFP cells. (A) Time-of-flight for size filtration of SEM cells from U251-GFP cells is calculated by integrating cell drift velocities with respect to radial distance and time. (B) False color epifluorescence micrographs of U251-GFP (green) and SEM (red) cells at different centrifugation time points. When the solution is loaded, both U251-GFP and SEM cells are located near each other in the chamber. Due to a size difference between U251-GFP and SEM cells, U251-GFP cells have a shorter time-of-flight to microwells than SEM cells during centrifugation. At 1000 RPM for 30 s, more than 30% of U251-GFP cells are already placed in microwells. After centrifuging for 1 min at 1000 RPM, a majority of U251-GFP cells are in microwells, while a majority of SEM cells do not reach microwells. Scale bar, 500 µm. (C) After centrifuging for 2 min at 1000 RPM, 58.4% of U251-GFP cells (n = 5, green) are selectively settled in microwells, while 6.4% of SEM cells (n = 5, blue, nucleus stained) are present in microwells. Scale bar, 100 µm. (D) scWesterns after sized-based separation of smaller SEM cells from larger U251-GFP cells. SEM only: micrograph from an scWestern of an SEM cell shows a positive peak for the 17 kDa H3K79me2 protein, a leukemia-specific protein. Micrograph of a scWestern blot for preferential cell seating of U251-GFP cells into microwells, using size-based separation of SEM cells from larger U251-GFP cells. scWestern reports the presence of U251-GFP cells only, as the H3K79me2 protein peak is absent. Scale bar is 500 µm.

Multiplexed protein analysis from sparse cell samples

Lastly, we applied the integrated preparatory and scWestern modules to multiplexed analysis of the proteins GFP (27 kDa), GAPDH (37 kDa), β-TUB (51 kDa), STAT3 (85 kDa) from individual glioblastoma (U251-GFP) cells (Figure 2.10). STAT3 is a transcription factor important in cell proliferation and tumor survival in glioblastoma [39–41]. The total duration

for cell handling was 2 min, with a total cell loss estimated at 25.3%. Seated U251-GFP cells had a mean diameter of 27.97 µm with a 9.2 µm range (IQR) (Figure 2.10A). The sparse starting sample consisted of 24 cells per a 15 µl suspension. Due to a poor sensitivity of total protein staining (>1 ng)[42, 43], separation resolutions are calculated by analyzing fluorescence peaks of STAT3, GAPDH, β-TUB, and GFP. Across 14 cells, the 1.5-mm long protein separation axis resolved all proteins with separation resolution exceeding baseline resolution (Figure 2.10B, Table 2.1). Within the same device, other proteins of interest (up to ~11 targets) can be detected by chemically stripping the gel and reprobing [14, 15].

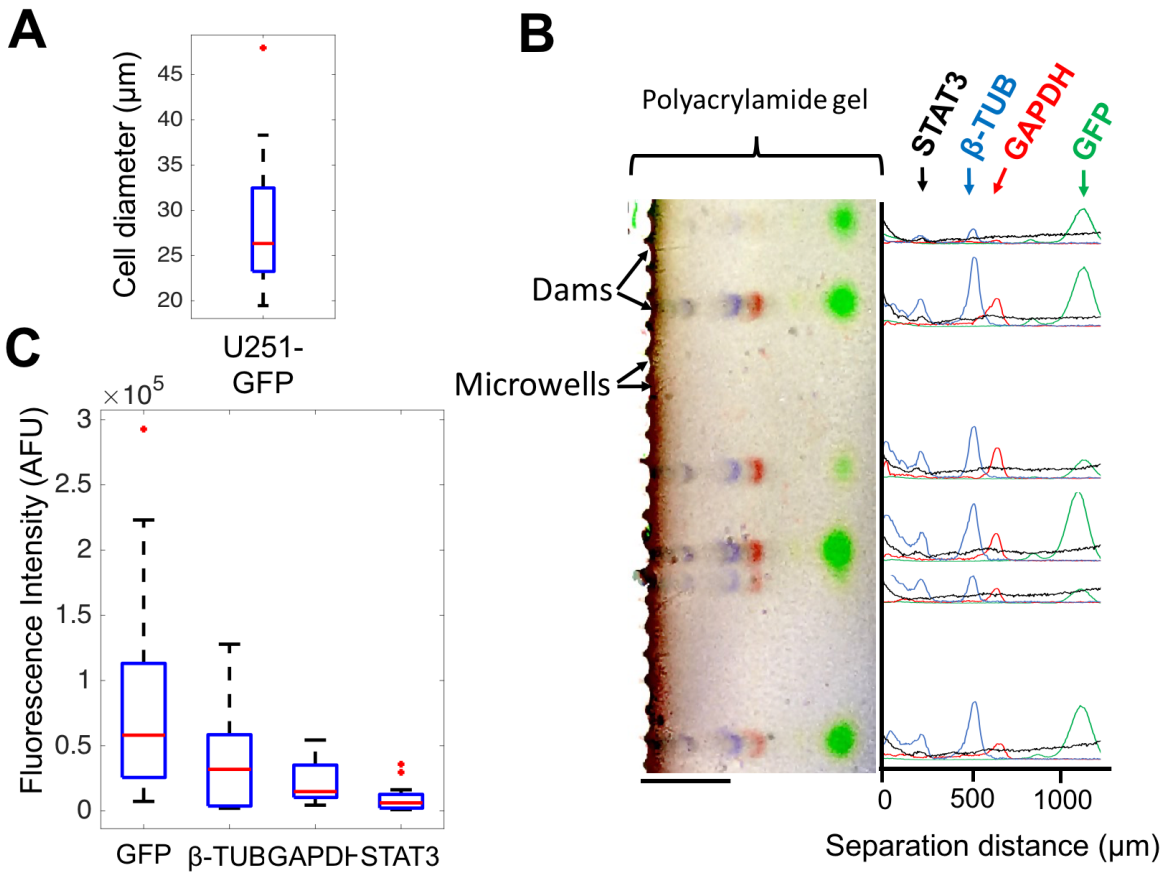

Figure 2.10: Lab-on-a-disc scWestern analysis of 14 single cells from a sparse, 24-cell biospecimen. (A) A box-and-whisker plot shows cellsize distribution of U251-GFP cells settled in microwells. (B) A falsecolor overlay of fluorescence micrographs from GFP (green), β-TUB (blue), GADPH (red), STAT3 (black) proteins with fluorescence intensity profile plots. (C) Box-and-whisker plots of STAT3, GFP, β-TUB, and GAPDH distributions are obtained from an area-under-the-curve analysis. Box ends represent 25th and 75th percentiles; IQR is the difference between the 25th and 75th percentiles; median value is the red line at box middle; whiskers spread to 95% confidence limits; and red dots indicate outliers. Scale bar, 500 μm.

To analyze protein distributions, fluorescence peak intensities (AUC) with a signal-to-noise ratio > 3 were measured after background subtraction (Figure 2.10C). Compared with the planar 2D-array scWestern blot [13], mean peak intensities of GFP, GAPDH, and β-TUB in our lab-on-a-disc device had no significance difference (Figure 2.10C, Figure 2.11). Based on a lower limit of detection (LOD) reported from the 2D-array scWestern blot, the lab-on-a-disc is estimated to have LOD of 45 zeptomoles (27,000 molecules). In the lab-on-a-disc device, a non-uniform background fluorescence signal was observed near microwells

	GFP & GAPDH	GFP & β-TUB	GFP & STAT3	GAPDH & β-TUB	GAPDH & STAT3	β-TUB & STAT3
Mean	2.38	3.02	5.68	1.52	5.66	3.67
STDEV	1.42	1.63	3.33	0.49	3.28	2.05

Table 2.1: Separation resolutions between each protein peak from the lab-on-a-disc scWestern device.

(Figure 2.10B). Gel thickness measurements suggest that a thicker gel region exists near the microwells (as compared to in the separation axis). We hypothesize that this thicker gel leads to preferential trapping of fluorescently labeled antibody probes near the microwells during immunoblotting (Figure 2.12). We are exploring design modifications to reduce gel thickness non-uniformity in this region. Nevertheless, the assay described here provides an analytical sensitivity suitable for an estimated $> 50\%$ of the mammalian proteome, with the LOD sufficiently sensitive for a median protein abundance of 27,000 molecules per cell [15, 44]. MAPK/ERK and apoptosis pathway proteins have been detected using a scWestern conducted using a planar 2D microwell array form factor [13, 14].

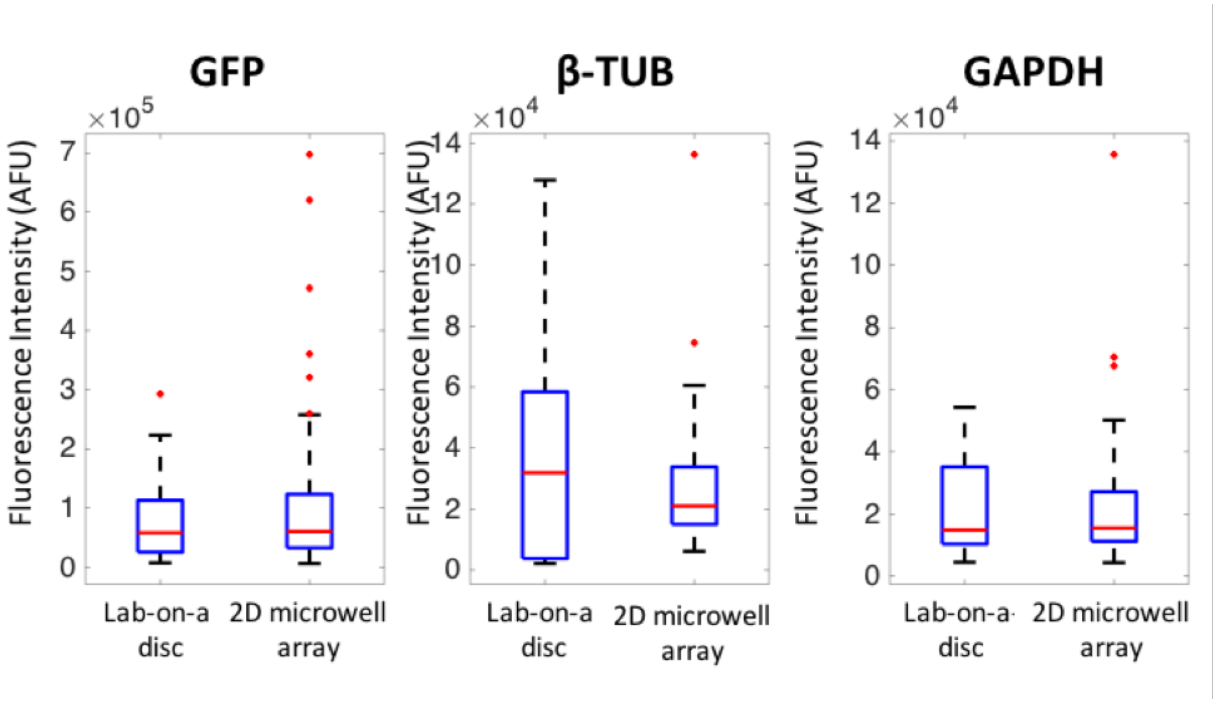

Figure 2.11: GFP, β-TUB, and GAPDH peak intensities from U251-GFP cells are compared between the lab-on-a-disc and the 2D microwell array (with gravity settling) scWesterns. The lab-on-a-disc and the 2D microwell-array scWesterns have no significant difference in fluorescence-intensity boxplots of GFP, β-TUB, and GAPDH. Blue box ends indicate 25th and 75th percentiles; median value is the red line at box middle; whiskers spread to 95% confidence limits; and red dots indicate outliers. (MannWhitney U-test, p-value of GFP = 0.54, p-value of β-TUB = 0.90, p-value of GAPDH = 0.65)

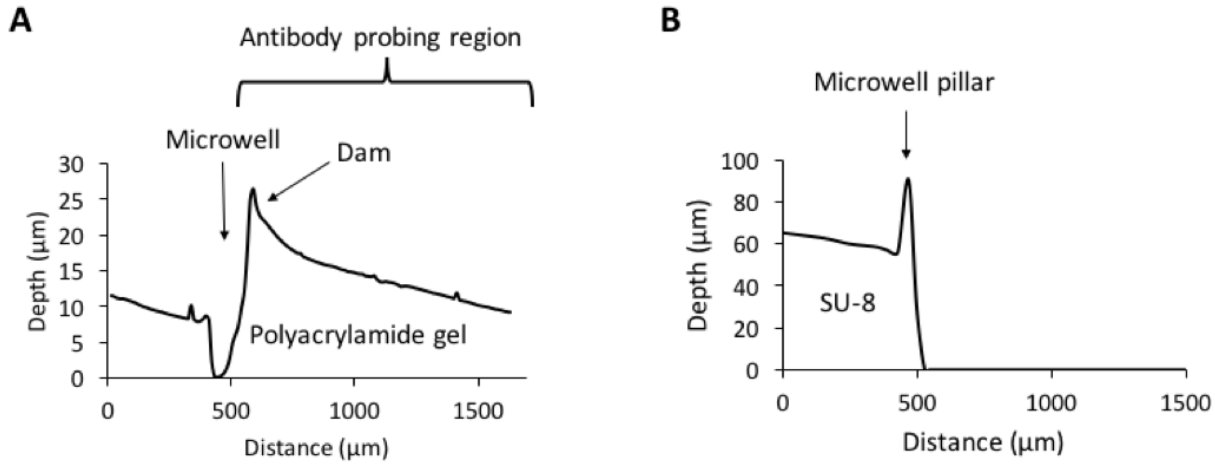

Figure 2.12: Measurement of gel thickness for a lab-on-a-disc device indicates an uneven thickness (height) for a dried gel near the microwell array. (A) A surface profile of the dried polyacrylamide gel device reports a thicker gel near the microwell region, as compared to further along the separation axis. (B) A surface profile of the complement SU-8 mold suggests that the dehydration process used prior to antibody probing could be a source of the gel height non-uniformity [45, 46].

. Surfaces are profiled using Sloan Dektak 3030.

2.4 Conclusion

We report on a multi-step yet integrated assay designed to extend high-specificity protein cytometry to low density (sparse) cell suspensions including dissociated biopsies. Based on operation with workhorse centrifuges, we designed a lab-on-a-disc device that integrates low loss cell handling with subsequent single-cell western blotting. Key design contributions include development of a two-layer soft lithography process for molding of polyacrylamide gel, the molecular sieving matrix required for protein electrophoresis.

After characterizing device and assay operation by identifying suitable operational parameters for sparse cell handling and analysis, we utilized the underlying physics of device operation to demonstrate a 'long-pass filtering mode operation, wherein large cells are preferentially seated into a linear microwell array for subsequent analysis. We view this fractionation based on cell size as having tremendous potential for robust cytology on heterogeneous dissociated cell populations including from clinical tissues.

To advance non-invasive and cost-effective cancer monitoring efforts, new approaches for preparing and interpreting sparse cell samples could complement existing measurements. Automated and rapid analysis of sparingly available cell samples from blood or bodily fluids

will improve diagnosis and prognosis of cancer [47, 48]. Especially in low-resource settings, a dearth of on-site cytotechnicians and cytopathologists has been reported to delay cell preparation and tumor grading for months after fine-needle biopsy collection in developing countries [48, 49]. Robust, integrated tools could also pave the way for the digital transmission of cytology imaging data from distributed settings [48, 49] to well-resourced clinical centers, which could be a step towards alleviating cytopathology bottlenecks already prevalent in less-resourced settings [48, 50, 51].

Bibliography

1. Navin, N. *et al.* Tumour evolution inferred by single-cell sequencing. *Nature.* ISSN: 00280836. doi:10.1038/nature09807 (2011).
2. Lohr, J. G. *et al.* Whole-exome sequencing of circulating tumor cells provides a window into metastatic prostate cancer. *Nat Biotechnol.* ISSN: 1087-0156. doi:10.1038/nbt.2892 (2014).
3. Ma, C. *et al.* Multifunctional T-cell analyses to study response and progression in adoptive cell transfer immunotherapy. *Cancer Discovery.* ISSN: 21598274. doi:10.1158/2159-8290.CD-12-0383. arXiv: NIHMS150003 (2013).
4. Patel, A. P. *et al.* Single-cell RNA-seq highlights intratumoral heterogeneity in primary glioblastoma. *Science.* ISSN: 10959203. doi:10.1126/science.1254257. arXiv: NIHMS150003 (2014).
5. Heath, J. R., Ribas, A. & Mischel, P. S. Single-cell analysis tools for drug discovery and development. *Nature Reviews Drug Discovery.* ISSN: 1474-1776. doi:10.1038/nrd.2015.16 (2015).
6. Bendall, S. C. *et al.* Single-cell mass cytometry of differential immune and drug responses across a human hematopoietic continuum. *Science.* ISSN: 00368075. doi:10.1126/science.1198704. arXiv: NIHMS150003 (2011).
7. Bodenmiller, B. *et al.* Multiplexed mass cytometry profiling of cellular states perturbed by small-molecule regulators. *Nature Biotechnology.* ISSN: 10870156. doi:10.1038/nbt.2317. arXiv: arXiv:1011.1669v3 (2012).
8. Gustafsdottir, S. M. *et al.* Multiplex cytological profiling assay to measure diverse. *PLoS ONE.* ISSN: 19326203. doi:10.1371/journal.pone.0080999 (2013).
9. Stack, E. C. *et al.* Multiplexed immunohistochemistry, imaging, and quantitation: A review, with an assessment of Tyramide signal amplification, multispectral imaging and multiplex analysis. *Methods.* ISSN: 10959130. doi:10.1016/j.ymeth.2014.08.016. arXiv: NIHMS150003 (2014).
10. Ellington, A. A. *et al. Antibody-based protein multiplex platforms: Technical and operational challenges* 2010. doi:10.1373/clinchem.2009.127514.

11. Martinet, W. *et al.* Western blot analysis of a limited number of cells: A valuable adjunct to proteome analysis of paraffin wax-embedded, alcohol-fixed tissue after laser capture microdissection. *Journal of Pathology.* ISSN: 00223417. doi:10.1002/path.1525 (2004).
12. Duncombe, T. A. *et al.* Hydrogel Pore-Size Modulation for Enhanced Single-Cell Western Blotting. *Advanced Materials.* ISSN: 15214095. doi:10.1002/adma.201503939 (2016).
13. Hughes, A. J. *et al.* Single-cell western blotting. *Nature Methods* **11,** 749–755. ISSN: 1548-7091 (2014).
14. Kang, C. C. *et al.* Single-cell western blotting after whole-cell imaging to assess cancer chemotherapeutic response. *Analytical Chemistry* **86,** 10429–10436. ISSN: 15206882 (2014).
15. Kang, C. C. *et al.* Single cell-resolution western blotting. *Nature Protocols.* ISSN: 17502799. doi:10.1038/nprot.2016.089 (2016).
16. Di Carlo, D., Aghdam, N. & Lee, L. P. Single-cell enzyme concentrations, kinetics, and inhibition analysis using high-density hydrodynamic cell isolation arrays. *Analytical Chemistry* **78,** 4925–30. ISSN: 00032700 (2006).
17. Eyer, K. *et al.* A microchamber array for single cell isolation and analysis of intracellular biomolecules. *Lab on a Chip.* ISSN: 14730189. doi:10.1039/c2lc20876h (2012).
18. Plouffe, B. D., Murthy, S. K. & Lewis, L. H. *Fundamentals and application of magnetic particles in cell isolation and enrichment: A review* 2015. doi:10.1088/0034-4885/78/1/016601. arXiv: NIHMS150003.
19. Kuhara, M. *et al.* Magnetic cell separation using antibody binding with protein A expressed on bacterial magnetic particles. *Analytical Chemistry.* ISSN: 00032700. doi:10.1021/ac0493727 (2004).
20. Woelfle, U., Breit, E. & Pantel, K. Influence of immunomagnetic enrichment on gene expression of tumor cells. *Journal of Translational Medicine* **3,** 12. ISSN: 14795876 (2005).
21. Chiou, P. Y., Ohta, A. T. & Wu, M. C. Massively parallel manipulation of single cells and microparticles using optical images. *Nature.* ISSN: 00280836. doi:10.1038/nature03831 (2005).
22. Thomas, R. S., Morgan, H. & Green, N. G. Negative DEP traps for single cell immobilisation. *Lab on a Chip.* ISSN: 14730189. doi:10.1039/b819267g (2009).
23. Voldman, J. *et al.* A microfabrication-based dynamic array cytometer. *Analytical Chemistry.* ISSN: 00032700. doi:10.1021/ac0256235 (2002).
24. Yang, L. *et al.* Effects of Dielectrophoresis on growth, viability and immuno-reactivity of Listeria monocytogenes. *Journal of Biological Engineering.* ISSN: 1754-1611. doi:10.1186/1754-1611-2-6 (2008).

25. Puttaswamy, S. V. *et al.* Enhanced cell viability and cell adhesion using low conductivity medium for negative dielectrophoretic cell patterning. *Biotechnology Journal.* ISSN: 18606768. doi:10.1002/biot.201000194 (2010).

26. Zimmermann, U. *Electric field-mediated fusion and related electrical phenomena* 1982. doi:10.1016/0304-4157(82)90007-7.

27. Kobayashi, H., Watanabe, R. & Choyke, P. L. *Improving conventional enhanced permeability and retention (EPR) effects; What is the appropriate target?* 2014. doi:10.7150/thno.7193.

28. Bandura, D. R. *et al.* Mass cytometry: Technique for real time single cell multitarget immunoassay based on inductively coupled plasma time-of-flight mass spectrometry. *Analytical Chemistry.* ISSN: 00032700. doi:10.1021/ac901049w (2009).

29. Shi, Q. *et al.* Single-cell proteomic chip for profiling intracellular signaling pathways in single tumor cells. *Proceedings of the National Academy of Sciences of the United States of America* **109,** 419–24. ISSN: 1091-6490 (2012).

30. Andreeff, M *et al.* Cellular ras oncogene expression and cell cycle measured by flow cytometry in hematopoietic cell lines. *Blood* **67,** 676–81. ISSN: 0006-4971 (1986).

31. Madou, M. *et al.* LAB ON A CD. *Annual Review of Biomedical Engineering.* ISSN: 1523-9829. doi:10.1146/annurev.bioeng.8.061505.095758. arXiv: arXiv:1011.1669v3 (2006).

32. Yeo, T. *et al.* Microfluidic enrichment for the single cell analysis of circulating tumor cells. *Scientific Reports.* ISSN: 20452322. doi:10.1038/srep22076 (2016).

33. Burger, R. *et al.* Array-based capture, distribution, counting and multiplexed assaying of beads on a centrifugal microfluidic platform. *Lab on a Chip.* ISSN: 14730189. doi:10.1039/c2lc21170j (2012).

34. Gorkin, R. *et al. Centrifugal microfluidics for biomedical applications* 2010. doi:10.1039/b924109d.

35. Ludwig, A., Kretzmer, G. & Schügerl, K. Determination of a "critical shear stress level" applied to adherent mammalian cells. *Enzyme and Microbial Technology.* ISSN: 01410229. doi:10.1016/0141-0229(92)90068-Y (1992).

36. Van Loon, J. J. *et al.* Inertial shear forces and the use of centrifuges in gravity research. What is the proper control? *Journal of biomechanical engineering.* ISSN: 01480731. doi:10.1115/1.1574521 (2003).

37. Durmus, N. G. *et al.* Magnetic levitation of single cells. *Proceedings of the National Academy of Sciences.* ISSN: 0027-8424. doi:10.1073/pnas.1509250112 (2015).

38. Zipursky, A *et al.* Leukocyte density and volume in normal subjects and in patients with acute lymphoblastic leukemia. *Blood.* ISSN: 0006-4971 (1976).

39. Luwor, R. B., Stylli, S. S. & Kaye, A. H. *The role of Stat3 in glioblastoma multiforme* 2013. doi:10.1016/j.jocn.2013.03.006.

40. Mukthavaram, R. *et al.* Effect of the JAK2/STAT3 inhibitor SAR317461 on human glioblastoma tumorspheres. *Journal of translational medicine* **13,** 269. ISSN: 1479-5876 (2015).

41. Sherry, M. M. *et al.* STAT3 is required for proliferation and maintenance of multipotency in glioblastoma stem cells. *Stem Cells.* ISSN: 10665099. doi:10.1002/stem.185 (2009).

42. Butt, R. H. & Coorssen, J. R. Coomassie Blue as a Near-infrared Fluorescent Stain: A Systematic Comparison With Sypro Ruby for In-gel Protein Detection. *Molecular & Cellular Proteomics.* ISSN: 1535-9476. doi:10.1074/mcp.M112.021881 (2013).

43. Neuhoff, V. *et al.* Improved staining of proteins in polyacrylamide gels including isoelectric focusing gels with clear background at nanogram sensitivity using Coomassie Brilliant Blue G???250 and R???250. *ELECTROPHORESIS.* ISSN: 15222683. doi:10.1002/elps.1150090603 (1988).

44. Li, J. J., Bickel, P. J. & Biggin, M. D. System wide analyses have underestimated protein abundances and the importance of transcription in mammals. *PeerJ.* ISSN: 2167-8359. doi:10.7717/peerj.270. arXiv: 1212.0587 (2014).

45. Kudo, K *et al.* Structural changes of water in poly(vinyl alcohol) hydrogel during dehydration. *The Journal of chemical physics.* doi:10.1063/1.4862996 (2014).

46. Vlassakis, J. & Herr, A. E. Joule Heating-Induced Dispersion in Open Microfluidic Electrophoretic Cytometry. *Analytical Chemistry* **89,** 12787–12796. ISSN: 0003-2700 (2017).

47. Stott, S. L. *et al.* Isolation of circulating tumor cells using a microvortex-generating herringbone-chip. *Proceedings of the National Academy of Sciences.* ISSN: 0027-8424. doi:10.1073/pnas.1012539107. arXiv: arXiv:1604.05974v2 (2010).

48. Guggisberg, K., Okorie, C. & Khalil, M. *Cytopathology including fine-needle aspiration in sub-saharan Africa: A cameroon experience* in *Archives of Pathology and Laboratory Medicine* (2011). ISBN: 0003-9985. doi:10.1043/1543-2165-135.2.200.

49. Shetty, M. K. & Longatto-Filho, A. Early detection of breast, cervical, ovarian and endometrial cancers in low resource countries: an integrated approach. *Indian journal of surgical oncology* **2,** 165–71. ISSN: 0976-6952 (2011).

50. Allison, K. H. *et al.* Understanding diagnostic variability in breast pathology: Lessons learned from an expert consensus review panel. *Histopathology.* ISSN: 13652559. doi:10.1111/his.12387. arXiv: 15334406 (2014).

51. Chandanwale, S. *et al.* Pattern of palpable breast lesions on fine needle aspiration: A retrospective analysis of 902 cases. *Journal of Mid-life Health.* ISSN: 0976-7800. doi:10.4103/0976-7800.145164 (2014).

Chapter 3

Microparticle delivery of protein markers for single-cell western blotting from microwells

Materials reproduced from: J.J. Kim*, P.Y. Chan*, J. Vlassakis, A. Geldert, and A.E. Herr, Single-cell immunoblotting benefits from a protein ladder delivered to each cell-laden microwell via magnetic microparticles, 2018

3.1 Introduction

Single-cell analysis tools report biomolecular heterogeneity that drives processes from immune-cell response to cancer progression [1–4], molecular standards are essential [5, 6]. In single-cell sequencing, synthetic spike-ins and unique molecular identifiers (e.g., short-random DNA sequence) directly measure error rates, analytical sensitivity, and biases stemming from sample preparation [7–9]. To calibrate flow cytometry lasers before cell sorting, fluorescent microparticles are used [10, 11]. In microfluidic protein assays (e.g., single-cell barcode assay), estimates of technical variation are inferred from multiple measurements of the same single-cell lysate [11].

Separations more generally also benefit from inclusion of standards, including capillary and microchannel electrophoresis formats [12–15]. In conventional slab-gel protein electrophoresis, the first or last separation lanes of the slab gel are typically employed for concurrent analysis of the protein ladder [16–19]. Comprised of standard protein molecules with known molecular sizes or isoelectric points, the protein ladder components serve as reference markers to compare physicochemical properties with unknown proteins of interest and ensure complete protein transfer to an immunoblotting membrane from the slab gel [20–23].Thus, the protein ladder is an essential quantitative tool to measure protein separation distance and estimate protein molecular sizes.

To isolate and analyze intact cells, arrays of microwells on a planar substrate have found utility [24–26]. Microwell arrays also allow concurrent analysis of cell lysate, from hundreds to thousands of cells [23, 24]. To assess cellular and proteoform heterogeneity in individual dissociated cells including circulating tumor and breast cancer cells [5, 27–31] — we have adopted the microwell array for cell isolation for chemical lysis, followed by polyacrylamide gel electrophoresis (PAGE) of each lysate in the surrounding polyacrylamide gel. After PAGE, the gel is also used for protein blotting (immobilization) and to support probing with immunoreagents. Thus, single-cell immunoblotting reports the presence or absence of each protein target (e.g., truncated isoforms [31]). For the microfluidic single-cell immunoblot, we design a solid phase protein ladder such that the ladder is suitable for (i) loading into the microwell array and (ii) solubilization concurrent with chemical lysis of each cell (e.g., <30 s). The standard proteins are packaged in rapid-release delivery vehicles for simultaneous PAGE of the protein ladder mixture and endogenous cellular protein targets.

Designs and methods for developing microscale carriers for proteins have been studied considerably for applications ranging from protein purification to drug delivery [3, 32–35]. One class of controlled protein delivery utilizes polymer hydrogels [34, 35]. Largely designed for tissue repair and targeted therapy to tumors, the polymer hydrogel packages proteins inside a matrix and serves as a scaffold for a sustained protein release, typically lasting up to several days [32, 33]. In another class of protein carriers, proteins are encapsulated in liposomes [36, 37]. Ranging from nano- to micro-scales, the liposomes are composed of phospholipid bilayers that are capable of carrying hydrophilic and hydrophobic molecules. Despite the ideal molecular compositions of the bilayers that match a cell membrane, liposomes have inherent instability in *in-vitro* handling (i.e. protein leakage due to unsaturated hydrocarbon chains) and non-uniformity in size that are challenging to integrate with the single-cell immunoblot [38].

For robust integration with the single-cell immunoblotting workflow, we investigate the use of Nickel(Ni^{2+})-coated microparticles as carriers of fluorescent protein standards. Here, we investigate the microparticles for quantized delivery and controlled release of fluorescent protein ladder components. Because the microparticles are similar in size to mammalian cells (~10 µm), application of an external magnetic field is feasible for directed loading of microparticles into cell-laden microwells [39–41]. Critically, the microparticles are coated with Ni^{2+}, thereby supporting reversible binding of histidine(His)-tagged proteins as protein ladder components [39, 42]. In designing and developing the microparticles for protein ladder delivery, we characterize protein release kinetics and optimize the cell lysis buffer system to also initiate solubilization of the protein ladder for subsequent injection into single-cell PAGE lanes. Sizing of endogenous protein targets from each cell is observed to be accurate (<20% of molecular mass error), with the robust integration of a co-migrating protein ladder.

3.2 Materials and Methods

Chemicals/Reagents

Acrylamide/bis-acrylamide 40% (wt/wt) solution (A7802), N, N, N', N'-tetramethylethylenediamine (TEMED, T9281), ammonium persulfate (APS, A3678), sodium deoxycholate (D6750), β-Mercaptoethanol (M3148), imidazole (792527), and sodium dodecyl sulfate (SDS, L3771), were obtained from Sigma-Aldrich. Triton X-100 was purchased from Fisher Scientific (BP-151). 10x Tris/glycine buffer was obtained from Bio-Rad (161-0734). PBS, pH 7.4 was obtained from Gibco (10010-023). Tris-HCl, pH 6.8 was purchased from Teknova (T1568). PureProteome nickel magnetic microparticles with 10-µm diameter was obtained from Millipore Sigma (LSKMAGH02). A 6-tube magnetic separation rack was obtained from New England BioLabs (S1506S). N-[3-[(3-Benzoylphenyl)-formamido]propyl] methacrylamide (BPMAC) was custom synthesized by PharmAgra Laboratories. SU-8 developer (Y020100) and photoresist SU-8 2025 (Y111069) were obtained from MicroChem. Deionized water (ddH2O, 18.2 mΩ) was obtained using ultrapure water system (Millipore). Unless stated otherwise, chemicals and reagents were obtained from Sigma Aldrich.

Proteins

Recombinant protein A His Tag (Protein A, ab52953) and recombinant human EpH receptor B4 protein His Tag (EpH, ab167746) were obtained from Abcam. KDR (VEGFR2) recombinant human protein, His Tag (KDR, 10012H08H50), ICAM1 recombinant human protein, hIgG1-Fc. His Tag (ICAM1, 10346H03H5), and CHI3L1 recombinant mouse protein His Tag (CHI3L1, 50929M08H50) were purchased from ThermoFisher Scientific. Unless stated otherwise, His tag proteins were fluorescently labelled using Alexa Fluor 647 NHS ester succinimidyl ester (Life Technologies, A20006). Fluorescently labelled His tag proteins were purified using dye removal columns (ThermoFisher Scientific, 22858) according to the manufacturer protocol. Details of the recombinant proteins used for protein ladder components are listed in Table 3.1.

Primary antibodies to recognize endogenous proteins include rabbit anti-β-tubulin (ab6046, Abcam), goat anti-GAPDH (SAB2500450, Sigma), mouse anti-cytokeratin 8 (C5301, Sigma), rabbit anti-estrogen receptor α(ab16660, Abcam), rabbit anti-STAT3 (79D7, Cell Signaling). For the primary antibody host species, secondary antibodies with Alexa Fluor were purchased from ThermoFisher Scientific: anti-mouse secondary antibody with Alexa Fluor 555 (A31570), anti-rabbit secondary antibody with Alexa Fluor 488 (A21206), anti-goat secondary antibody with Alexa Fluor 555 (A21432).

Protein	Species	Mw (kDa)	Company (Catalog no.)
Recombinant Protein A, His Tag	E. coli	39	Abcam (ab52953)
CHI3L1 recombinant mouse protein, His tag	Mouse	42.3	Thermofisher (50929M08H50)
PDGFRA recombinant human protein (without catalytic activity), His tag	Human	57.7	Thermofisher (10556H08H25)
Recombinant human EpH receptor B4 protein	Human	58	Abcam (ab167746)
KDR (VEGFR2) Recombinant Human Protein, His Tag	Human	84.6	ThermoFisher (10012H08H50)
ICAM1 Recombinant Human Protein, hIgG1-Fc. His Tag	Human	100	ThermoFisher (10346H03H25)

Table 3.1: List of proteins carried by nickel-conjugated magnetic microparticles.

Protein Loading on Nickel Microparticles

Magnetic microparticles (5 µl) were equilibrated with buffer (50 mM sodium phosphate, 300 mM sodium chloride, 10 mM imidazole, pH 8). A 500 µl protein solution containing a mixture of His Tag proteins in 30% (v/v) ethanol/PBS was loaded with the microparticles and mixed gently for 2 h at 4 °C using a rotator. Un-bound proteins were washed 3 times using wash buffer (50 mM sodium phosphate, 300 mM sodium chloride, 20 mM imidazole, pH 8). Residual liquid was separated from the microparticle using a magnetic rack and removed after each of the above steps. The protein bound microparticles were re-suspended in 1x PBS.

In order to determine protein release kinetics, 5 µl of microparticles was loaded with 4.1 µg of Protein A. For electrophoretic separations, 5 µl of microparticles was loaded with either one of two protein mixtures containing: (1) 2 µg of Protein A, or (2) 14.8 µg of CHI3L1, 54.5 µg of EpH, 21.9 µg of KDR, and 7.4 µg of HIgG1-F. The bound His Tag protein was eluted from the microparticles using lysis/electrophoresis buffer prepared with 0 or 1M of imidazole, 2.5 g of SDS, 1.25 g of sodium deoxycholate, 500 µl of TritonTM X-100, 25 ml of 10x Tris/glycine buffer and 474.5 ml of ddH2O.

Cell Culture

The MCF-7 breast cancer cell line was purchased from ATCC and maintained in RPMI 1640 (ThermoFisher Scientific) containing 10% fetal bovine serum and 1 penicillin/streptomycine in a humidified incubator held at 37 °C under 5% CO_2. MCF-7 was tested mycoplasma

negative and authenticated with short tandem repeat analysis.

Fabrication of Single-cell Immunoblot Chip

The master mold comprised a silicon wafer with SU-8 features that was fabricated according to standard photolithography procedure [28]. Single-cell immunoblot devices containing an array of microwells (250 µm well-to-well spacing and 1 mm long separation lane) with feature heights and diameters of 35 µm and 30 µm, respectively, were fabricated by casting a polyacrylamide gel against the mold [28]. The polyacrylamide gel layer was chemically polymerized using 7% T, 3.45 %C, 3 mM BPMAC, 0.08% APS and 0.08% TEMED.

Single-cell Immunoblot Buffer Exchange

After settling cells in microwells by gravity, a chemical lysis buffer (0.5X Tris glycine, 0.5% SDS, 0.25% sodium deoxycholate, 0.1%Triton X-100, 1M Imidazole, pH 9.2, 55°C) was poured into the single-cell immunoblot for 30 s to release protein ladder components from microparticles and solubilize endogenous proteins from mammalian cells. Then, a 2 s electrophoresis at 40 V/cm was applied immediately for protein injection. For protein separation, an electrophoretic buffer (0.5X Tris glycine, 0.5% SDS, 0.25% sodium deoxycholate, 0.1%Triton X-100, pH 8.7, 22°C) was introduced, followed by immediate electrophoresis at 40 V/cm for 23 s.

Fluorescence Imaging

Protein A bound microparticles were prepared and settled into microwells under a magnetic field. Fluorescence protein release from the microparticles in the microwells were visualized using an Olympus IX71 inverted fluorescence microscope equipped with ASI motorized stage, X-cite mercury lamp light source (Lumen Dynamics) and standard Cy5 filter cube (40x objective). Time-lapse images were captured using an iXon+ EMCCD camera (Andor Technology Ltd) controlled by a MetaMorph software (Molecular Devices) with 60 ms exposure time and 2 s time intervals.

Image Analysis and Quality Control

For the release kinetics measurement, image processing was performed using a Python script (Anaconda Python 3.5.3). Circular region of interest (ROI) were manually selected via a Graphical User Interface provided using the cv2 Python package (OpenCV 3.1.0). Image pixel statistics were estimated using the numpy Python package (numpy 1.13.1). Mean fluorescence intensity from a ROI covering the whole microparticle was obtained. Background signal was designated as the mean fluorescence intensity measured from an adjacent empty

microwell. Each Mean fluorescence intensity of the microwell was background subtracted and then normalized to the value at the start of the release process (t = 0).

For the single-cell immunoblot analysis, images of proteins were collected by scanning the single-cell immunoblot devices with a fluorescence microarray scanner (Genepix 4300A, Molecular Devices). The images were processed by applying a median filter with a 2-pixel radius and a threshold value of 50 (ImageJ). Quantitation of proteins from the images was processed by in-house MATLAB (R2016b) scripts [28]. Protein peaks were fitted with Gaussian functions. For quality control, the protein peaks with Gaussian fitting R2 $\geq$ 0.7 and SNR >3 were analyzed [28]. From the curve fitting, protein peak width and location were extracted to determine protein molecular mass from Ferguson analysis [15, 21].

3.3 Results and discussion

To enhance the reproducibility and reliability of single-cell immunoblotting, we design, characterize, and develop a microparticle vehicle for delivery of a 4-component protein ladder to each of hundreds of concurrent single-cell immunoblots. The single-cell immunoblot assay is a multi-stage microfluidic assay, which is comprised of 5 steps including cell preparation and analysis (Figure 3.1): cell settling, microparticle settling, release & lysis, gel electrophoresis & photocapture, immunoprobing. To design for integration into the single-cell immunoblot assay, we selected magnetic microparticles as a vehicle to deliver a 4-component protein ladder to each of thousands of microwells on the single-cell immunoblot device. Protein ladder components were labeled a priori with fluorescent dyes. Here, we scrutinize and adapt the design of the microparticle-based protein sizing ladder in light of the desired performance of the single-cell immunoblot.

Design of the rapid release protein ladder delivery vehicle

A magnetic microparticle delivery system was selected for delivery of a protein ladder to each microwell and single-cell PAGE assay. We employed: (i) an applied magnetic field to actively seat microparticles in microwells (i.e., in contrast to gravity-based particle settling; Figure 3.2A) and (ii) a flexible coordination chemistry on the microparticle surface for protein ladder immobilization and triggered solubilization/release (Figure 3.2B). We utilized two key microparticle characteristics to achieve the desired functionality and performance: (i) magnetic cores for active microparticle seeding in microwells directed via magnetic field and (ii) a Ni^{2+} coating that balances high-yield protein immobilization with rapid protein release (<30 s).

We first sought to assess the efficiency of a two-step microwell loading process. First, we seated MCF-7 breast cancer cells in each microwell by applying a suspension of the cells (~25 µm diameter) onto the polyacrylamide gel housing 1300 microwells. Cells were allowed to sediment via passive gravity for 10 min (Figure 3.3, Figure 3.1, step 1). Gentle

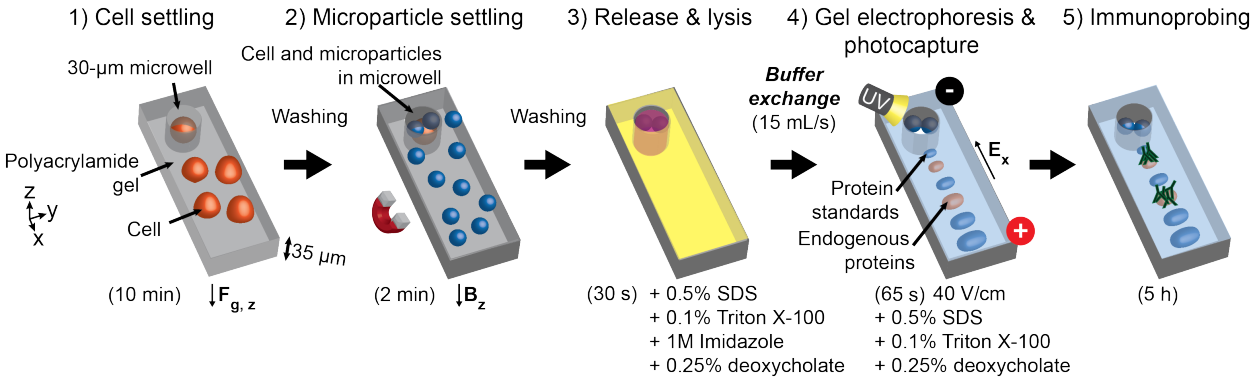

Figure 3.1: Schematic of the single-cell immunoblot workflow utilizing microparticles to introduce protein ladder components (blue peaks) for molecular mass determination of endogenous proteins from cells (orange peaks). The workflow comprises five stages: 1. cell settling by passive gravity ($F_{g,z}$), 2. microparticle settling by applying a magnetic field in the z-direction (B_z), 3. in-situ protein ladder release and cell lysis, 4. electrophoresis and photo-activated immobilization of protein ladder components and cellular proteins in the polyacrylamide gel, 5. in-gel immunoprobing.

washing removed cells that settled onto the surface of the polyacrylamide gel. Next, to deliver our protein ladder into each cell-laden microwell using the microparticle delivery vehicle, a solution of microparticles (106 microparticles/ml) was dispensed onto the single-cell immunoblot device and directed into the microwells using an applied magnetic field for 2 min (Figure 3.1, step 2). The magnet (4 cm diameter x 1.53 cm height) was located under the 2.5 cm x 3.75 cm device and moved across the device to expose all microwells to the applied magnetic field. Gentle washing removed microparticles from the surface of the polyacrylamide gel.

At the completion of the two-stage microwell loading process, we observed via bright-field microscopy nearly 75% of microwells housing >1 microparticle (n = 3 chips, standard deviation σ= 4%, Figure 1B). We observed 38.3% of microwells containing a single MCF-7 cell, similar to performance with cell settling alone (Figure 3.2A) [43]. Overall, we observed 35.3% (n = 3 chips, standard deviation σ= 8.1%) of microwells containing both a single cell and $\geq$ 1 microparticle.

We next sought to quantitatively assess (i) the Ni^{2+} chelation for solid phase immobilization of protein ladder on the microparticle surface and (ii) the subsequent rapid triggered solubilization of ladder components into the PAGE separation stage (Figure 3.2B, C). Given the 30 µm diameter and 35 µm deep microwell design, we opted for 10-µm diameter microparticles comprised of Ni^{2+} that bind to His-tagged proteins comprising the protein ladder. We sought to solubilize and release the protein ladder from the microparticle surface in a pulse release profile with <30 s duration [28], so as to synchronize with the cell lysis and endogenous protein solubilization dynamics observed in the single-cell immunoblot.

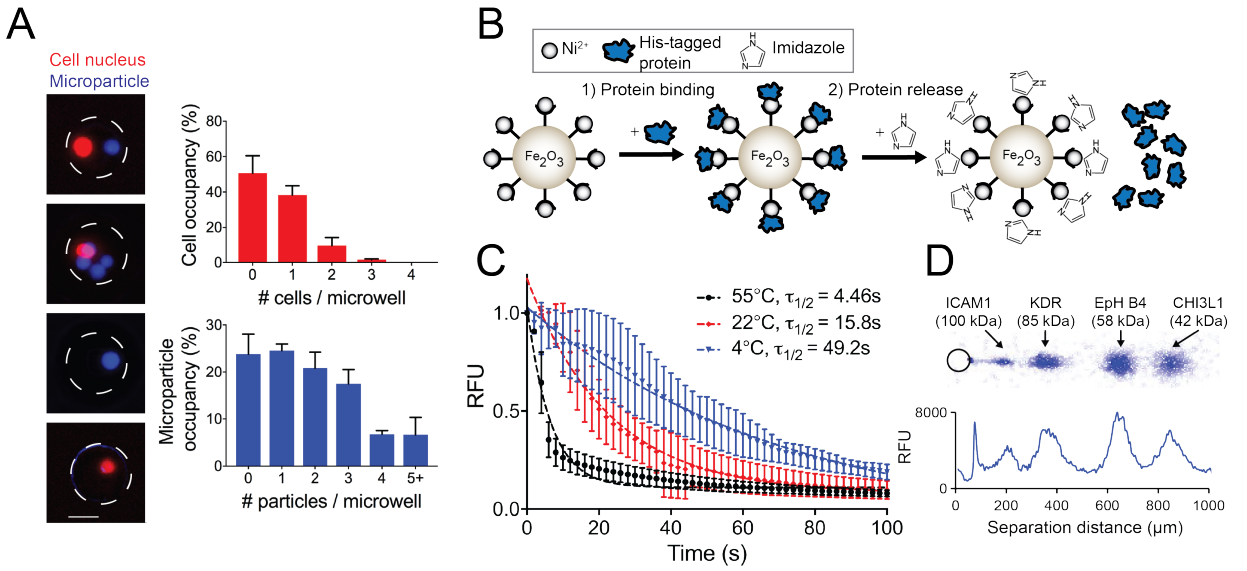

Figure 3.2: Microparticles deliver protein ladder components for mass sizing in single-cell immunoblots.(A) Occupancy rates of MCF-7 cells and microparticles in microwells. False-color micrographs represent microwells with a cell (red, nucleus) and/or microparticles (blue). Scale bar, 15 µm. Bar graphs depict occupancy rates of cells and microparticles per microwell. Error bars are standard deviations of n = 3 chips. (B) Schematic illustrates how His-tagged protein ladder components are bound and released from Ni^{2+}-coated microparticles. (C) Time-lapse plots of the fluorescence intensity, represented as relative fluorescence unit (RFU), of a microwell containing a single protein-loaded microparticle. At different buffer temperatures with 1M Imidazole, fluorescent proteins are released from the microparticle and diffuse out the microwell (n = 3 microwells, error bars are standard deviation). Colored dashed lines represent exponential curve fitting, and a half-life for each buffer temperature is listed. Black: y = 1.04*exp(-0.16t) + 0.11, R^2 = 0.91. Red: y = 1.18*exp(-0.04t) + 0.08, R^2 = 0.90; Blue: y = 1.03*exp(-0.01t) 0.09, R^2= 0.87. (E) Representative false-color micrograph and intensity profile of four standard proteins (ICAM1, 100 kDa; KDR, 85 kDa; EpH B4, 58 kDa; CHI3L1, 42 kDa) that were separated and immobilized in the polyacrylamide gel.

To immobilize the protein ladder on the microparticles, the microparticles were incubated (2 h) in a cocktail of fluorescently labeled and His-tagged proteins (KDR, 21.9 ng/µl; ICAM1, 7.40 ng/µl; EpH B4, 54.5 ng/µl; CHI3L1, 14.8 ng/µl). After incubation with proteins, the microparticles were washed 3 times with washing buffer containing mild imidazole (20 mM). Via flow cytometry, we observed 98% of microparticles coated with the fluorescent protein ladder components (Figure 3.2B, Figure 3.4).

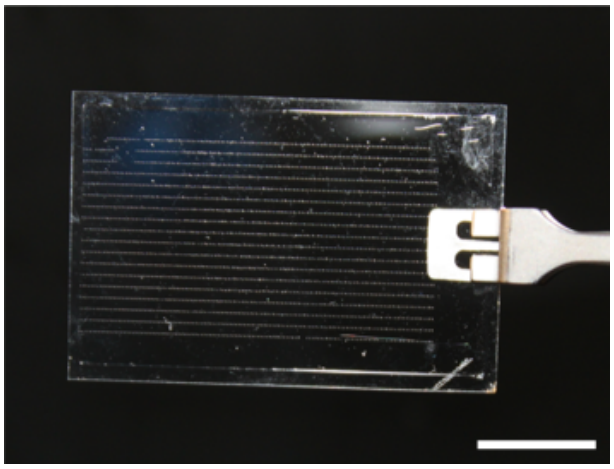

Figure 3.3: Single-cell immunoblotting array of 30-µm microwells patterned in a thin layer of polyacrylamide gel. Scale bar, 1 cm.

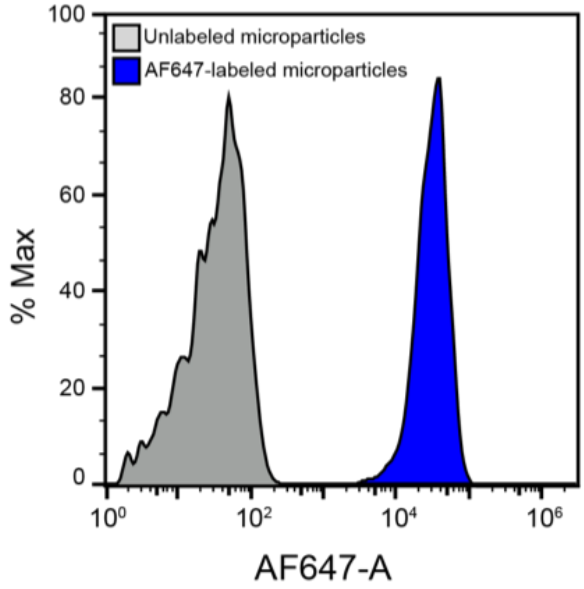

Figure 3.4: Percent of microparticles labeled with AF647-tagged proteins (ICAM1, KDR, EpH B4, CHI3L1) is analyzed by by flow cytometry. Blue histogram represents fluorescence variation and % maximum population of microparticles labeled with AF647-tagged proteins ($n_{labeled}$ = 2587). The blue peak between 103 and 105 indicates 98% of microparticles are tagged with AF647-proteins. Grey histogram represents fluorescence variation and % maximum population of microparticles without AF647-tagged proteins ($n_{unlabeled}$ = 2201).

After identifying microparticle preparation conditions, we examined the release kinetics of His-tagged Recombinant Protein A labeled with Alexa Fluor 647 (AF647), as a represen-

tative protein ladder component. To displace the His-tagged proteins from the microparticle surface, we selected imidazole as a competitive binding ligand. Release of His-tagged Protein A from the microparticles was modeled according to one-state ligand-receptor kinetics (an exponential decay).

In a negative control, lysis buffer without imidazole resulted in release of Protein A with a half-life of 63.4 s and a dissociation rate constant of 0.011 s^{-1} (Figure 3.5). We noted that the observed dissociation rate constant was 10x greater than that previously reported [44] and attribute the discrepancy to the elevated (55 °C) buffer temperature employed here.

Next, we examined cell lysis buffer containing an excess of imidazole (0.015 mmol), as compared the His-tagged Protein A decorating the microparticles (0.12 nmol). Given the orders-of-magnitude differential, we assume that the imidazole concertation is not significantly reduced over the 30-s time course of protein ladder release and cell lysis. The Protein A release kinetics in the presence of imidazole at 4 °C suggest a half-life of 49.2 s and a dissociation rate constant of 0.014 s^{-1} (Figure 3.2C).

As a first corollary, we next elevated the cell lysis buffer temperature and observed dissociation rate constants of 0.044 s^{-1} (at 23 °C) and 0.16 s^{-1} (at 55 °C), with the latter condition yielding a protein release half-life of 4.46 s. Within the 30 s window slot, >80 % of the His-tagged Protein A was released from the microparticles at 55 °C (Figure 3.2C).

As a second corollary, we scrutinized the dissociation rate constant for a range of higher imidazole concentrations at the most elevated temperature condition. We observed the shortest release half-life of 4.46 s with a 1M imidazole concentration (Figure 3.5). Consequently, we selected lysis buffer containing 1M imidazole at 55 °C to release His-tagged protein ladder components from the microparticles during single-cell PAGE.

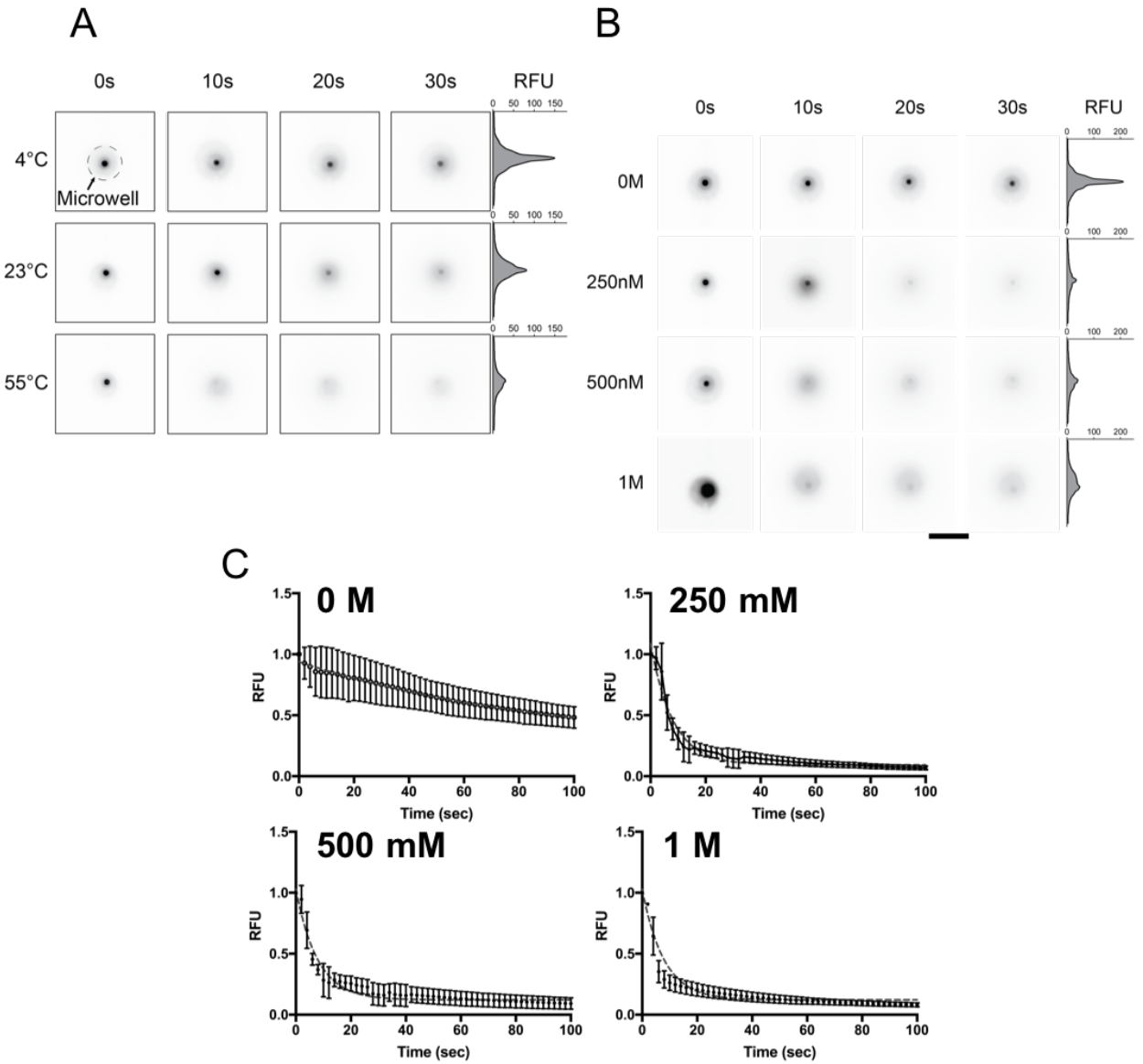

Figure 3.5: The effect of buffer temperature imidazole concentration on AF647-tagged Protein A release kinetics from microparticles. Representative fluorescence false-color micrographs showing protein release from a microparticle in a microwell at different lysis (A) temperatures (4 °C, 23 °C, 55 °C) and (B) imidazole concentrations (0 M, 250 mM, 500 mM, 1 mM). Scale bar, 30 m length. (C) Time-lapse plots of the fluorescence intensity from microwell in buffer with different Imidazole concentrations. Dashed lines represent exponential curve fitting. 0 M: y = 0.94*exp(-0.01t) + 0.25, R^2 = 0.64, 250 mM: y = 1.09*exp(-0.12t) + 0.09, R^2 = 0.90, 500 mM: y = 1.03*exp(-0.13t) + 0.12, R^2 = 0.85, 1 M: y = 1.04*exp(-0.16t) + 0.11, R^2 = 0.91.

Validating the protein ladder as a molecular mass standard

After rapid release of the protein ladder in the microwell, we scrutinized the protein ladder electromigration during single-cell protein PAGE (Figure 3.2D, Figure 3.6). At 30-s of cell lysis and protein ladder release, PAGE was trigged by applying an electric field (E = 40 V/cm) for 25 s. Separated protein peaks were immobilized in the gel matrix using photoblotting, comprised of a 45 s UV exposure of the benzophenone-containing polyacrylamide gel. After immobilization, Ferguson analysis of the observed protein electromigration was performed [15, 21]. In protein sizing (gel electrophoresis with SDS), we expect a log-linear relationship between the molecular mass of each target protein and the observed electrophoretic mobility of that target. Log-linear fitting of the known ladder proteins yielded $R^2 > 0.97$ for > 300 PAGE separation lanes (Figure 3.6A). Technical variation in protein peak location was observed to be minor, having to a coefficient of variance (CV) ranging from 2.2% to 11.0% depending on the ladder component considered (Table 3.2).

	Chip 1			Chip 2			Chip 3		
Protein	Mean (µm)	Standard Deviation (µm)	CV (%)	Mean (µm)	Standard Deviation (µm)	CV (%)	Mean (µm)	Standard Deviation (µm)	CV (%)
ICAM1	180.74	13.85	11.02	125.72	12.75	10.14	175.78	12.44	7.08
KDR	349.37	22.3	7.91	281.76	19.59	6.95	339.42	13.61	4.01
EpH B4	624.28	35.35	6.5	544.14	33.4	6.14	616.48	14.48	2.35
CHI3L1	817.9	49.34	6.65	741.44	47.43	6.4	809.54	17.4	2.15

Table 3.2: Quantitation of peak location for microparticle-delivered protein ladder components from 3 chips ($n_{chip1} = 147$, $n_{chip2} = 104$, $n_{chip3} = 340$). Peak location was determined from the peak center parameter of a Gaussian fit in MATLAB.

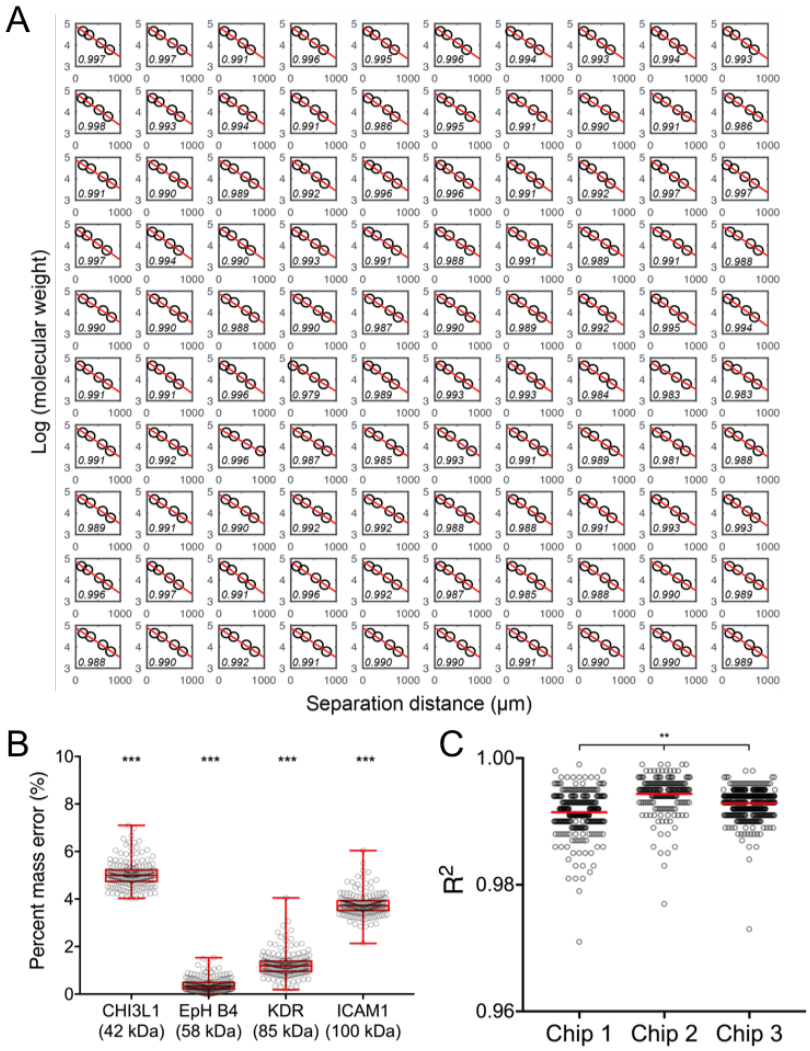

Figure 3.6: Ferguson analyses of the protein ladder and utility as an estimator of molecular mass. (A) Log-linear regression fitting of protein ladder components (ICAM1, KDR, EpH B4, CHI3L1) in 100 representative single-cell PAGE protein separations. R^2 value for each linear fit is shown in lower left of each plot. Black circles, protein ladder components; red lines, linear regression fits. (B) Box and scatter plots of percent mass errors between expected and estimated molecular masses of protein ladder components in a single-cell immunoblot chip. Each black circle represents percent mass error per PAGE separation lane. Box extents indicate 25th and 75th quantiles; black line at box midpoint indicates median value; whiskers extend to minimum and maximum values. Kruskal-Wallis test with Dunns multiple comparisons test, ***$p < 0.0001$, $n = 168$ PAGE separation lanes. (C) Scatter plots indicate chip-to-chip R^2 values for linear regression fits. Black circles indicate R^2 values for PAGE separation lanes; red line indicates mean value for each chip ($\mu_1 = 0.991$, $\mu_2 = 0.994$, $\mu_3 = 0.993$); $n_1 = 327$, $n_2 = 204$, $n_3 = 516$; one-way ANOVA test, $p < 0.001$, Cohens d < 0.2.

Across each device, we found no observable spatial dependence on the y-intercept values of the log-linear regression but did observe a decrease in the slope across the width of the chip (Figure 3.7). Recognizing that a ΔE = ~1 V/cm across the width of the chip (left to right) would result in the observed slope variation; we hypothesized that the apparatus has a slight offset in electrode pair spacing from one end of the chip to the other (Figure 3.7).

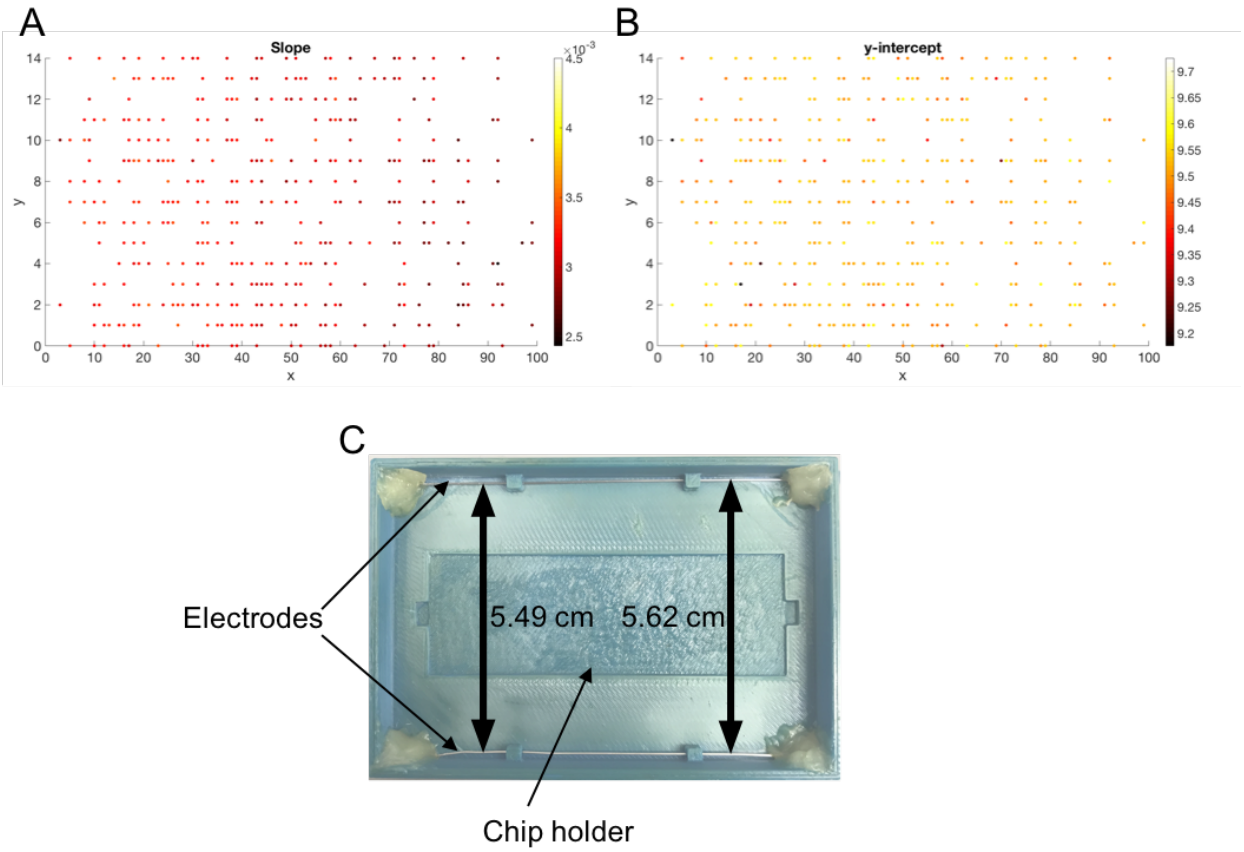

Figure 3.7: Variation of protein ladder electromigration in a single-cell immunoblot chip. (A) Heat map displaying variance of log-linear regression slope values from microwells with protein ladder markers. (B) Heat map displaying variance of log-linear regression y-intercept values from microwells with protein ladder markers. (C) A top view of electrophoretic chamber. The chamber is composed of two electrodes and a holder for the single-cell western blot chip. Distance difference between the electrodes, measured at the ends of the holder in x-axis, leads to ΔE = ~1 V/cm from left to right across the chip.

For each protein marker, we compared the expected molecular mass to the measured molecular mass. An analysis of 168 single-cell PAGE lanes gives a difference between the two values of $< 5\%$, with an interquartile range (IQR) $< 1\%$ (Figure 3.6B), for all protein

markers that passed quality control (see Experimental Section). Interestingly, the percent mass error of the smallest ladder component (CHI3L1, 42 kDa) and the largest ladder component (ICAM1, 100 kDa) were significantly higher than those of EpH B4 (58 kDa) and KDR (85 kDa) ($\mu \pm \sigma$ of percent mass error: ICAM1, 3.77 ± 0.49; KDR, 1.24 ± 0.53; EpH B4, 0.39 ± 0.30; CHI3L1, 5.05 ± 0.57; Kruskal-Wallis test with Dunns multiple comparisons test, ***$p < 0.0001$, n = 168 PAGE separation lanes; Figure 3.6B). We attribute the higher percent mass errors of CHI3L1 and ICAM1 to CHI3L1 and ICAM1 data deviating greater than EpH B4 and KDR from the log-linear regression line, as peak location CV values are not significantly different among all four markers (Figure 3.6A,Table 3.2, n = 3 chips, one-way ANOVA test, $p > 0.5$). High and low molecular mass proteins should be included in each set of protein marker standards for most accurate estimation of molecular mass, which agrees with previous work demonstrating that the use of a pair of high and low molecular mass protein standards controlled for technical variation in migration rate in a capillary gel electrophoresis platform [45].

Next, we examined chip-to-chip variation in molecular mass estimation to assess reproducibility of the protein marker as a size standard (Figure 3.6C, 3.8). Regarding the goodness of the log-linear regression fit, we observed $R^2 > 0.97$ (n = 3 chips; Figure 3.6C). One-way ANOVA tests indicate that the distributions of the R2 values are significantly different among the chips. However, the magnitude of the chip-to-chip difference in R2 values is minimal, with a Cohens $d < 0.2$ (Figure 3.6C). We further investigated technical variation across the chips by analyzing percent mass errors of the protein markers. Although the slight run-to-run difference in the gel electrophoresis duration might contribute to the fact that distributions of percent mass errors are significantly different across chips (Figure 3.8), we observed consistent protein electromigration (CV of peak locations $< 12\%$) and $< 10\%$ mass errors in sizing of the protein markers (42 – 100 kDa protein masses; Figure 3.8, Table 3.2).

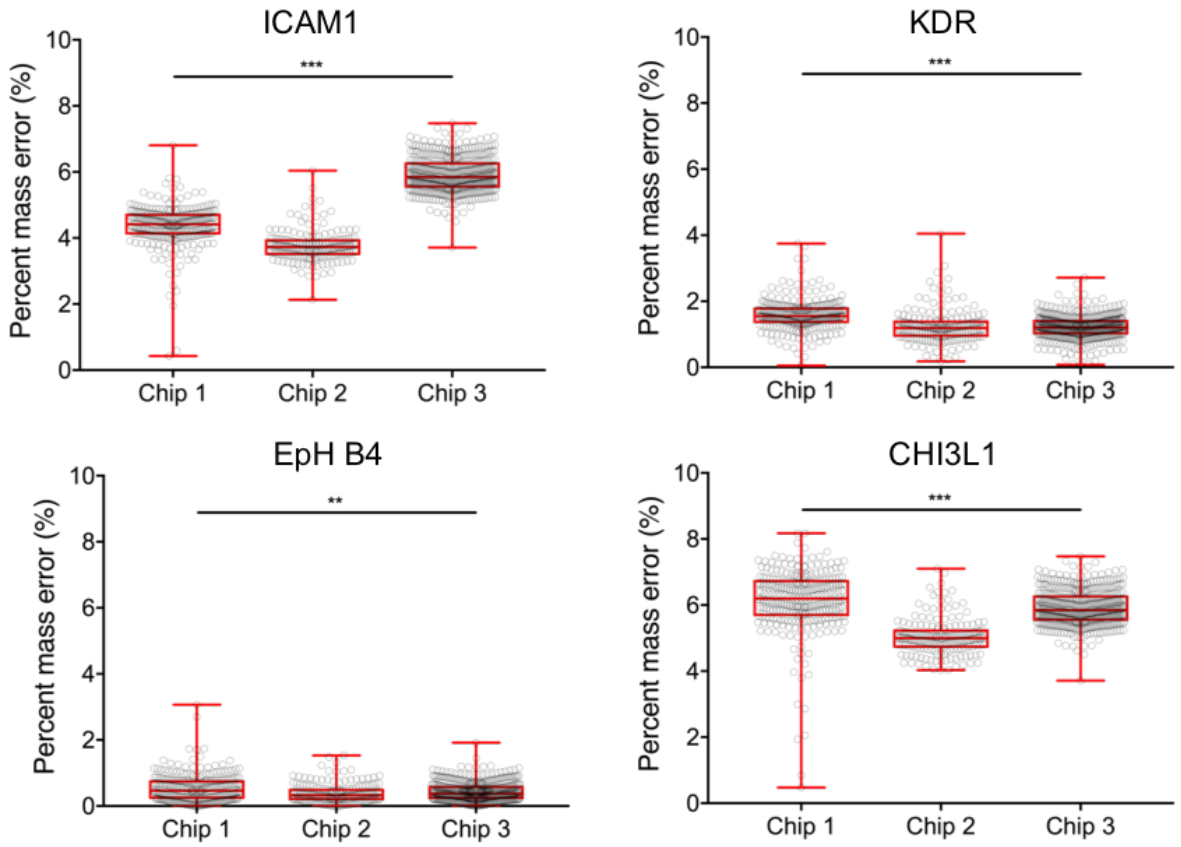

Figure 3.8: Scatter plots of percent mass error between expected and estimated molecular weight of protein markers across 3 chips. Each black circle represents percent mass error per separation lane. Red box ends indicate 25th and 75th quantiles; middle red line at box indicates median value; whiskers extend to minimum and maximum values. Kruskal-Wallis test, ***p $<$ 0.0001, **p $<$ 0.001; $n_{chip1} = 257$, $n_{chip2} = 168$, $n_{chip3} = 415$.

Given that not all cell-containing microwells are populated with microparticles, we sought to understand the limits and constraints on using protein ladder components proximal to single-cell PAGE separations as migration standards. To understand spatial continuity of electromigration, we sought to apply semi-variogram (γ) model [46, 47] to estimate variance of the slope or y-intercept values (Z) from the log-linear regression by comparing pairs (N) of two microwells with protein ladder components at various spacing (h) between the microwell (Equation 5.1):

$$\hat{\gamma} = \frac{1}{2N}\sum_{i=1}^{N}(Z_i - Z_{i+h})^2 \tag{3.1}$$

We used a semi-variogram analysis of the log-linear fitting coefficients and determined that molecular mass estimates of proteins of interest are accurate using protein ladder elec-

tromigration, if the ladder originates from a microwell located $\leq$ 2.5 mm (center-to-center pitch) from the microwell with the proteins of interest (Equation 5.1, Figure 3.9).

We observed no significant difference (Kruskal Wallis test with Dunns multiple comparisons test, p >0.05) in molecular mass error when protein sizing was performed either using the ladder from the same PAGE separation lane as the proteins of interest or the ladder located $\leq$ 2.5 mm from the PAGE separation lane containing the proteins of interest (Figure 3.10).

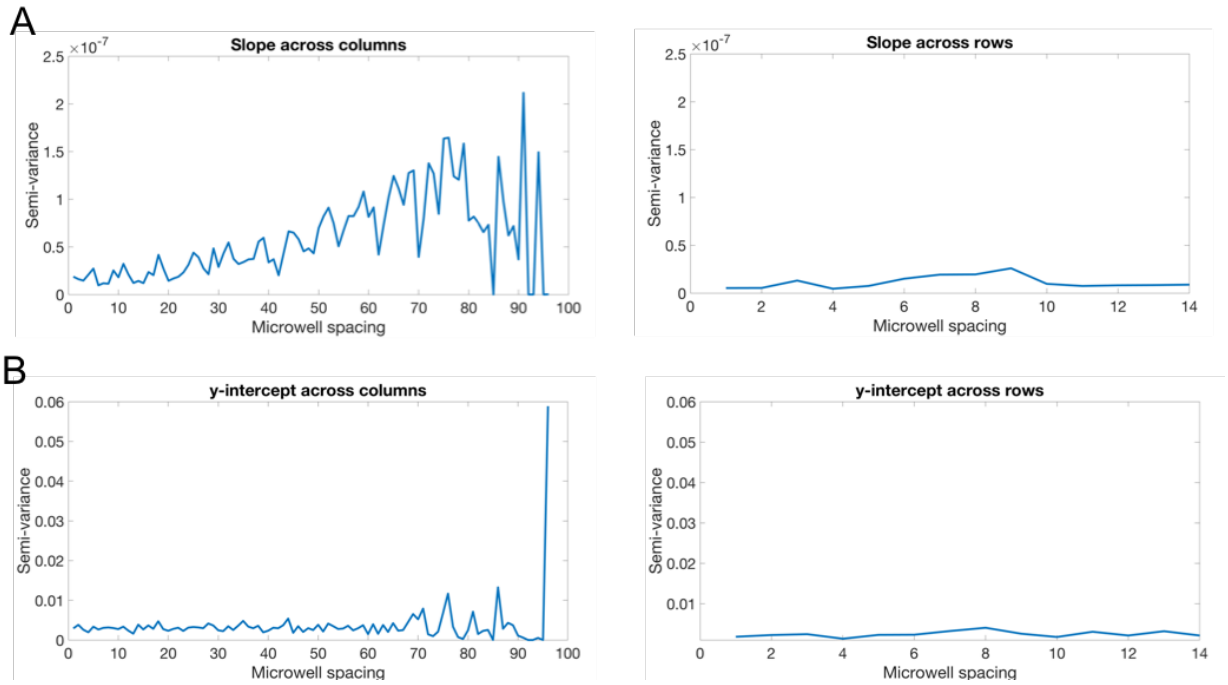

Figure 3.9: Spatial analysis of protein ladder electromigration. (A) Semi-variogram of the slope values at different microwell spacing across the single-cell immunoblot array columns (left) and rows (right). Across the columns, slope variance begins to increase when microwell spacing >10. The slope variance does not vary across rows. Microwell spacing (center-to-center pitch) across columns, 250 µm and across rows, 1 mm. (B) Semi-variogram of the y-intercept values at different microwell spacing across the single-cell immunoblot array columns (left) and rows (right). The y-intercept semi-variograms indicate that variance does not dependent on microwell locations across the device.

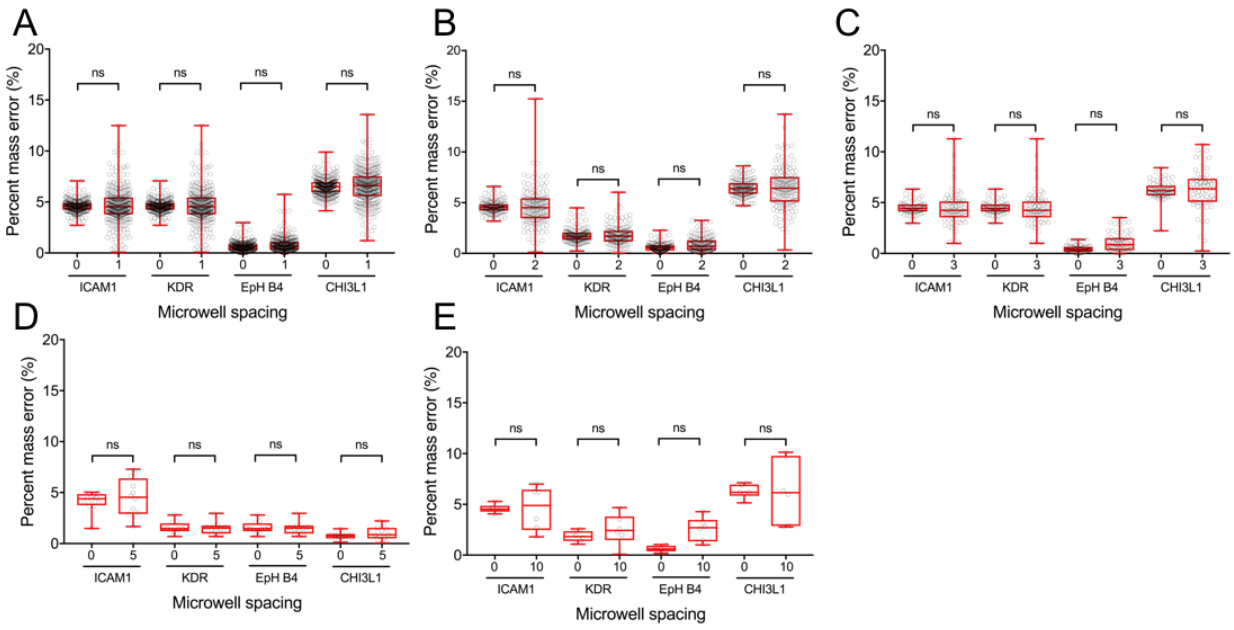

Figure 3.10: Scatter plots indicating percent mass error distribution of protein standards at different microwell spacing (A) 1, (B) 2, (C) 3, (D) 5, (E) 10. Each microwell spacing (center-to-center pitch) is 250 µm. After the log-linear fitting, mass of protein ladder components at proximal microwells are measured with the log-linear regression. Each black circle represents percent mass error per separation lane. Box ends indicate 25th and 75th quantiles; middle black line at box indicates median value; whiskers extend to minimum and maximum values. Kruskal-Wallis test with Dunns multiple comparisons test, ns: p ¿ 0.05, $n_A = 318$; $n_B = 152$; $n_C = 67$; $n_D = 12$; $n_E = 6$.

Imidazole interferes with protein photoblotting

After protein PAGE, photoblotting to immobilize protein peaks in the polyacrylamide gel uses a UV-mediated covalent attachment of proteins to benzophenone incorporated in the polyacrylamide gel. Efficient photoblotting is critical for protein detection and immunoprobing, but we observed low levels of immobilized protein in the imidazole buffer resulting 3.7% yield of separation lanes with protein ladder that passed quality control (Figure 3.11A, B). We hypothesized that, in the presence of a high concentration (1M) of imidazole, the UV-activated benzophenone group incorporated in the polyacrylamide gel abstracts a hydrogen from a secondary amine group in the imidazole and undergoes recombination to form a covalent bond with the imidazole (Figure 3.11C) [48].

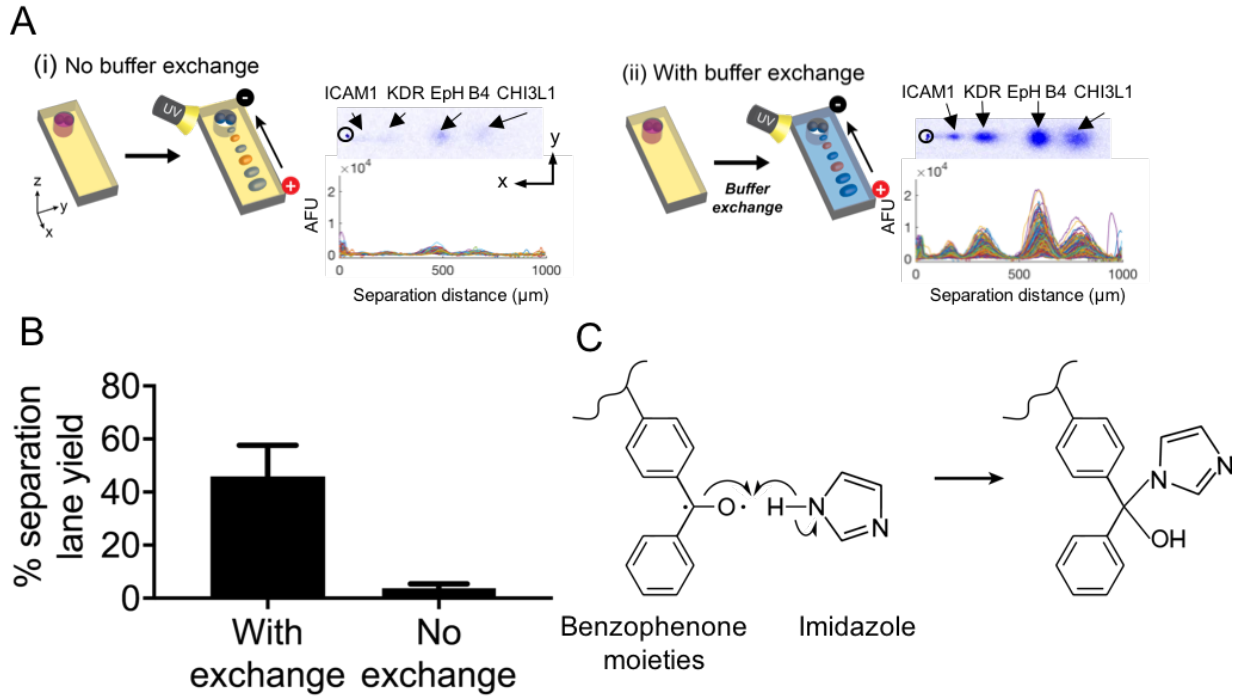

Figure 3.11: Imidazole reduces protein ladder expression levels and contributes to poor yield of separation lanes with protein ladder that passed quality control. (A) False-color representative micrographs of single-cell protein PAGE with 1M imidazole present during photoblotting and with buffer exchange to dilute imidazole prior to photoblotting. Each intensity plot represents the protein ladder resolved along one PAGE separation lane. (B) Bar graph representing fraction of protein ladder components that passed quality control (SNR >3, R^2 for Gaussian curve fitting >0.7). Error bars represent standard deviations. Black circles represent data per PAGE separation lane; red lines represent mean values; unpaired t test, *** p <0.0001, ** p <0.002, ns = no significance (p >0.05). (C) Mechanism for imidazole reacting with UV-activated benzophenone moieties incorporated in the gel.

To investigate this potential confounding mechanism, we included a buffer-exchange step to eliminate the imidazole during the photoblot step (See Experimental Section). The buffer exchange was performed between the chemical cell lysis and the protein PAGE steps to remove imidazole prior to the UV photoblot step [49]. Buffer exchange has been previously employed by our group to reduce Joule heating during single-cell electrophoresis [50]. We calculated SNR for each Gaussian-fitted protein ladder peak (R^2 >0.7) with and without a buffer exchange. The buffer exchange improved SNR for all 4 protein ladder components; comparing mean values, the SNR with the buffer exchange was >20% greater than the SNR without the buffer exchange (Figure 3.12A). We next examined SNR of endogenous protein expression levels with and without the buffer exchange. The buffer exchange restored immunoprobing of β-tubulin (β-TUB), cytokeratin 8 (CK8), and GAPDH to levels obtained

without the imidazole in the chemical lysis step (Figure 3.13).

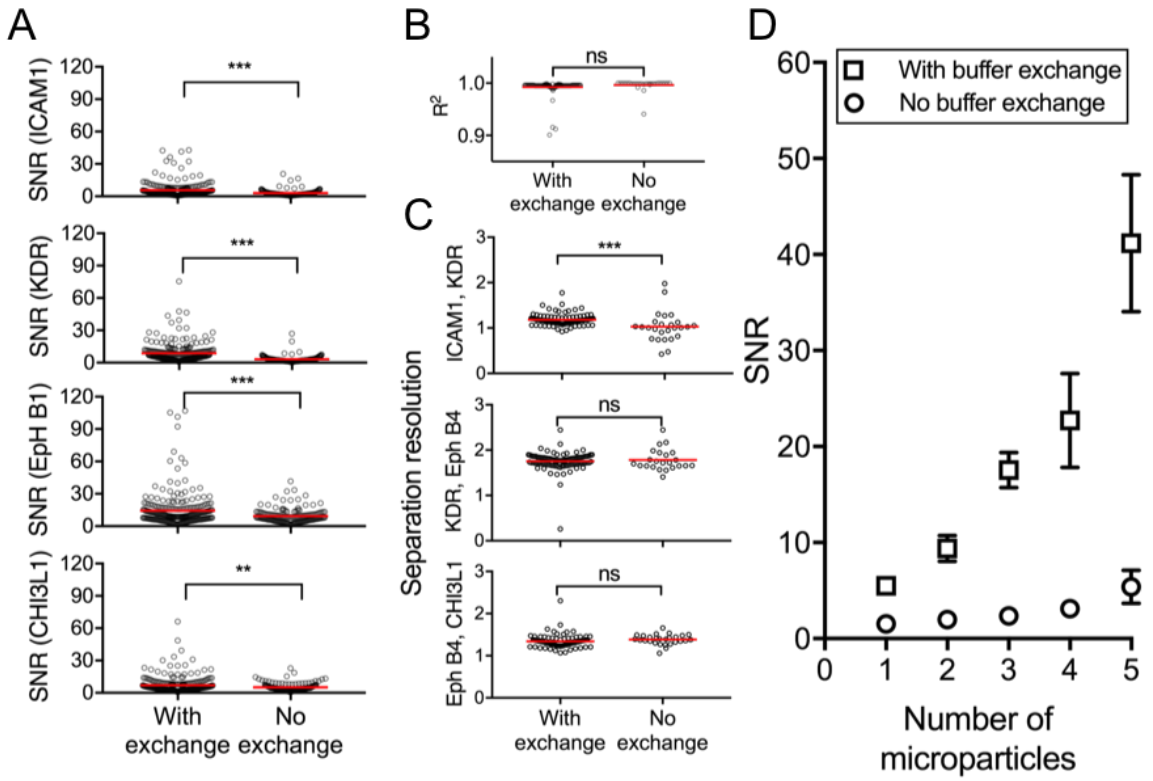

Figure 3.12: Buffer exchange minimizes imidazole interference with ladder protein components. (A) Scatter plots of signal-to-noise ratio (SNR) of protein ladder peaks with and without buffer exchange ($n_{\text{with exchange}} = 249$, $n_{\text{no exchange}} = 149$). (B) Scatter plot indicating R^2 values with and without buffer exchange. ($n_{\text{with exchange}} = 107$, $n_{\text{no exchange}} = 27$). (C) Scatter plots of separation resolution between two protein ladder components with or without buffer exchange ($n_{\text{with exchange}} = 107$, $n_{\text{no exchange}} = 27$). (D) Scatter plot of KDR peak SNR as a function of the number of microparticles in the microwell (n = 4 microwells, error bar is standard deviation). Each square represents a mean SNR value of KDR with buffer exchange. Each circle represents a mean SNR value of KDR without buffer exchange. With buffer exchange, one microparticle per microwell is sufficient to detect all protein ladder components with SNR >3. (F) Bar graph representing fraction of protein ladder components that passed quality control (SNR >3, R^2 for Gaussian curve fitting >0.7). Error bars represent standard deviations. Black circles represent data per PAGE separation lane; red lines represent mean values; unpaired t test, *** $p < 0.0001$, ** $p < 0.002$, ns = no significance ($p > 0.05$).

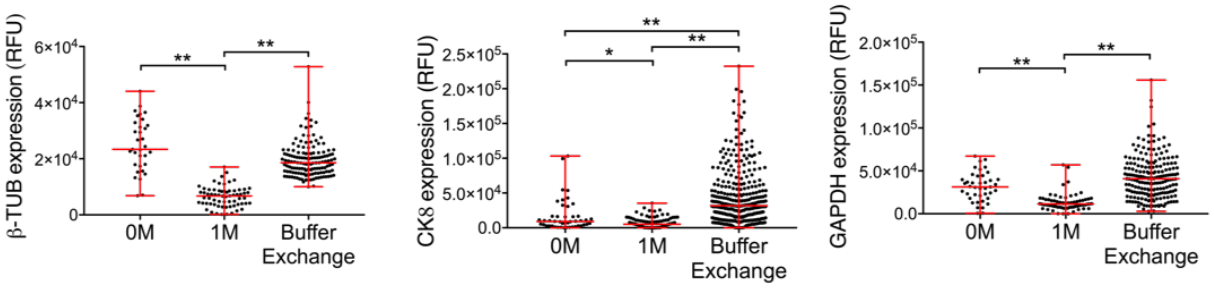

Figure 3.13: Buffer exchange minimizes imidazole interference with cellular endogenous proteins. Scatter plots of β-TUB, CK8, GAPDH expressions under different lysis buffer conditions (Kruskal Wallis test, DunnSidak corrections, *p <0.05, **p <0.0001). After protein lysis and release, buffer exchange eliminates imidazole that interferes with UV-activated protein photocapture. Each black dot represents an endogenous protein from individual cells per microwell. Red lines indicate median with range from maximum to minimum expression values. β-TUB: $n_{0M} = 33$, $n_{1M} = 66$, $n_{\text{Buffer Exchange}} = 141$; CK8: $n_{0M} = 46$, $n_{1M = 116}$, $n_{\text{Buffer Exchange}} = 328$; GAPDH: $n_{0M} = 41$, $n_{1M} = 69$, $n_{\text{Buffer Exchange}} = 201$.

Considering total assay performance, we next asked whether the buffer exchange might affect the goodness of fit in the log-linear regression and separation resolution (SR) of the protein ladder components (Figure 3.12B, C). The goodness of fit distribution of R^2 values with the buffer exchange was not significantly different from that without the buffer exchange (Figure 3.12B; unpaired t test, $p = 0.20$, $n_{\text{with exchange}} = 107$, $n_{\text{no exchange}} = 27$). Furthermore, no decrease in SR between the protein ladder components was detectable (Figure 3.12C). In fact, the median and mean SR between ICAM1 and KDR were slightly greater with the buffer exchange, as compared to the imidazole containing conditions without the buffer exchange (Figure 3.12C). We did not observe reduced Joule heating upon buffer exchange, nor corresponding improvements in SR [50]. The buffer exchange employed here utilized room temperature lysis buffer, which contains high concentrations of conductive ionic detergents that result in heating-induced peak dispersion during electrophoresis.

Minimum number of microparticles per microwell required for detection

We sought to understand the number of microparticles per microwell required to detect protein ladder components with an SNR >3. The KDR protein was used to assess the relationship between SNR of protein peaks (E = 40 V/cm; t = 25 s) and the number of microparticles per microwell. The SNR increased with an increasing number of microparticles per microwell (Figure 3.12D). Without buffer exchange, in excess of 3 microparticles per microwell were required to achieve an SNR >3 (Figure 3.12D). In contrast, the buffer exchange and dilution of imidazole yielded SNR >5 with a single microparticle in a microwell (Figure 3.12D). This increase in SNR means that 55% of the protein ladder components which

passed quality control (see Experimental Section), are qualified as protein molecular mass standards, in contrast to 3.7% of components qualifying without the buffer exchange (Figure 3.11B). Consequently, one microparticle per microwell was sufficient for each single-cell immunoblot.

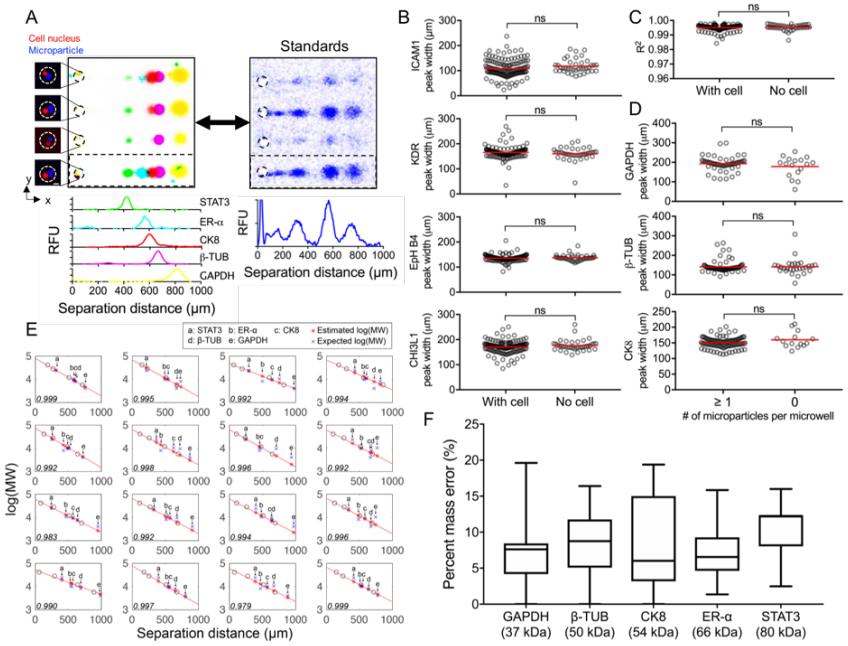

Figure 3.14: Determination of protein mass using single-cell immunoblots benefits from inclusion of a protein ladder with each single-cell PAGE separation.(A) Top: false-color micrographs display microwells containing an MCF-7 cell (red) and microparticles (blue). Scale bar, 10 μm. Bottom: intensity profiles and false-color micrographs of four representative PAGE lanes containing both endogenous proteins (STAT3, 80 kDa; ER-α, 66 kDa; CK8, 54 kDa; β-TUB, 50 kDa; GAPDH, 37 kDa) and a protein ladder (blue). (B) Scatter plots indicate no significant difference in peak widths of protein ladder components with and without cells in microwells. Black circles represent peak width of each ladder component; red lines represent mean values; unpaired t test and F test, ns = no significance ($p > 0.05$); $n_{\text{with cell}} = 141$, $n_{\text{no cell}} = 39$. (C) Scatter plot indicates no significant difference in R^2 values from linear regression with and without a cell in the microwell. Black circles indicate R^2 values per separation lane; red lines represent mean values; unpaired t test and F test, ns = no significance ($p > 0.05$); $n_{\text{with cell}} = 141$, $n_{\text{no cell}} = 39$ (D) Scatter plot representing no significance difference in GAPDH ($n_{\geq 1} = 55$, $n_0 = 17$), β-TUB ($n_{\geq 1} = 77$, $n_0 = 28$), and CK8 ($n_{\geq 1} = 97$, $n_0 = 14$) peak widths in microwells with or without microparticles. Black circles indicate endogenous protein peak width per separation lane; red lines represent mean values; Mann-Whitney test, n_s = no significance ($p > 0.05$). (E) Representative Ferguson plots display estimated (*) and expected (x) molecular masses of endogenous proteins extracted from linear regression of the protein ladder. R^2 value for each log-linear fit is in the lower left of each plot. Black circles, protein ladder; red lines, log-linear regression fitting. (F) Box plots depict % error between estimated and expected molecular masses of STAT3 (n = 95 cells), ER-α (n = 7 cells), CK8 (n = 794 cells), β-TUB (n = 551 cells), and GAPDH (n = 430 cells) from the Ferguson analysis plots.

Determining molecular mass of endogenous protein targets in MCF-7 cells

We estimated molecular masses of endogenous proteins from single cells by employing the protein ladder as a reference standard (Figure 3.14). For microwells containing both individual MCF-7 breast cancer cells and one or more microparticles, we performed single-cell immunoblotting and concurrently resolved protein ladder components and endogenous proteins in each PAGE separation lane (Figure 3.14A).

We sought to identify any confounding interactions when running protein PAGE on the protein ladder and single-cell lysate from the same microwell. We found no significant difference in the distribution of the peak widths of the protein ladder components in the presence ($\mu \pm \sigma$; ICAM1: 108.5 ± 34.47, KDR: 165.6 ± 22.81, EpH B4: 135.8 ± 12.46, CHI3L1: 170.4 ± 24.2) and absence ($\mu \pm \sigma$; ICAM1: 118.1 ± 27.13, KDR: 160.3 ± 25.75, EpH B4: 137.3 ± 12.1, CHI3L1: 176.5 ± 21.88) of cells, suggesting that negligible interference occurred owing to co-loading, concurrent cell lysis and protein ladder solubilization, and concurrent sample injection (Figure 3.14B; unpaired t-test and F-test, $p > 0.05$, $n_{\text{with cell}} = 141$, $n_{\text{no cell}} = 39$). The goodness of the log-linear fit to the protein ladder remained $R^2 > 0.97$ and was not significantly different from conditions with no cells in the microwells (Figure 3.14C, unpaired t test and F test, $p > 0.05$, $n_{\text{with cell}} = 141$, $n_{\text{no cell}} = 39$).

Reciprocally, for microwells with and without microparticles, we analyzed the immunoprobed endogenous proteins to identify any confounding effects. We used GAPDH, β-TUB, CK8 as representative endogenous proteins and found that the protein peak widths ([$\text{median}_{\geq 1 \text{ microparticle}}$, $\text{median}_{0 \text{ microparticle}}$]; GAPDH [193.4, 192.5], β-TUB [134.3, 136.9], CK8 [151.3, 151.9]; Mann-Whitney test, $p > 0.05$) were not notably affected by the presence of protein-loaded microparticles in the same microwells (Figure 3.14D).

Using the protein ladder, we next determined the molecular mass of a set of endogenous protein targets in the MCF-7 cells. Here, we utilized the log-linear regression equation developed from the protein ladder and the measured peak location for each target (for ladders and single-cell immunoblots performed within the ≤ 2.5 mm mentioned earlier). We analyzed >100 PAGE separation lanes with protein ladders that passed quality control (see Experimental Section) and a R^2 exceeding 0.97 for the log-linear regression. In these cases, the molecular masses of GAPDH (39.6 kDa), β-TUB (47.0 kDa), CK8 (54.3 kDa), and ER-α(66 kDa) and the reported molecular masses determined by conventional slab-gel western blots agreed with both median and mean mass errors of <10% (Figure 3.14E, F). For STAT3 (80 kDa), we observed a slightly larger mean mass error at 10.3% and median mass error at 12.2% (Figure 3.14F). Note that conventional slab-gel western blotting reported three protein peaks within the 70 — 100 kDa range using the STAT3 antibody (Figure 3.15), possibly slightly reducing the accuracy of sizing this target.

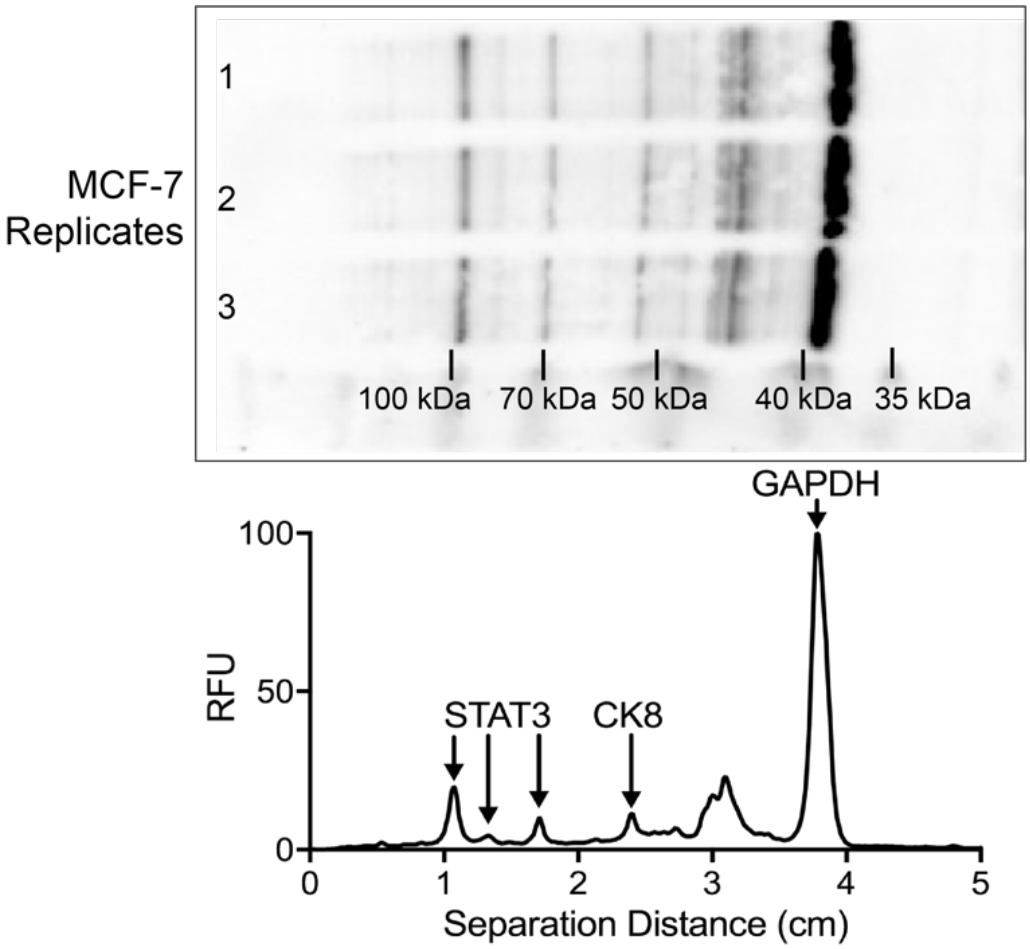

Figure 3.15: Slab-gel western blots of STAT3, CK8, GAPDH, with MCF-7 cells.

Overall, single-cell PAGE with the protein ladder resulted in mean and median mass errors $< 12\%$ for all endogenous protein targets from the MCF-7 cells (Figure 3.14F). When microwells within a 2.5 mm x 10 mm region were considered, the log-linear regression with the microparticle-delivered protein ladder performed target mass estimation more accurately than using other endogenous immunoprobed protein targets. The mean and median mass errors for CK8 were >40% lower when determined by the protein ladder rather than by known endogenous cellular protein targets (Figure 3.16). With optimization of cell lysis and antibody probing, we anticipate the microparticle protein ladder vehicle will find utility in assigning molecular masses to proteoforms, including truncated isoforms with >20% molecular mass differences from the full-length protein (Figure 3.14F) [51–53].

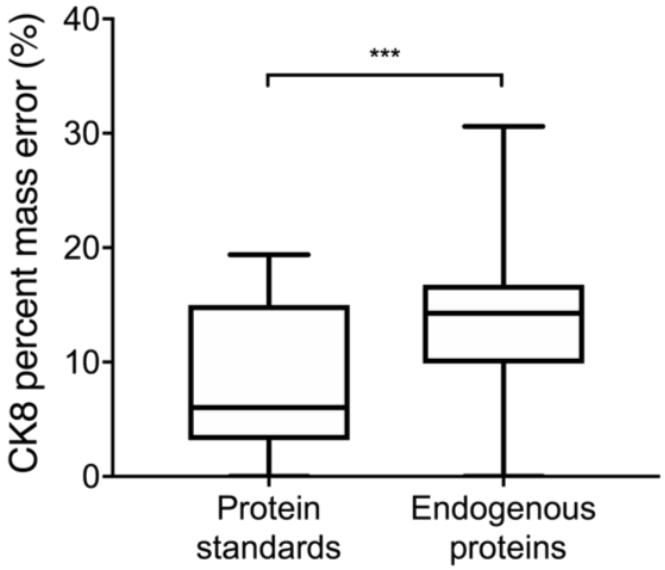

Figure 3.16: Protein ladder performs molecular sizing of CK8 more accurately than cellular proteins as standards. Scatter plots indicating percent mass error distribution of CK8, estimated by performing log-linear regression with protein standards or four cellular proteins (GAPDH, β-TUB, ER-α, STAT3). For protein sizing with the protein standards (n = 794), the protein standards located $\leq$ 10 microwell spacing apart from CK8 protein peaks were used. For protein sizing with the endogenous proteins (n = 8820), every combination of GAPDH, β-TUB, ER-α, STAT3, and CK8 peaks within $\leq$ 10 microwell spacing was computed and evaluated. Mann Whitney test, *** $p < 0.0001$.

3.4 Conclusion

As single-cell resolution assays emerge and mature, an increased emphasis on reliability and reproducibility is also emerging. Complementing single-cell resolution genomics and transcriptomics are single-cell protein assays (flow cytometry, immunofluorescence, immunohistochemistry, mass cytometry/CyTOF). Especially critical to direct measurement of proteoforms (isoforms, splice variants, etc.) and protein interactions is single-cell resolution immunoblotting. To establish a molecular mass standard for single-cell immunoblots, we design, characterize, and apply a protein migration ladder delivered in solid-phase using a magnetic microparticle vehicle. The microparticle delivery and chemically triggered ladder release allows concurrent analysis of the protein ladder with each electrophoretic separation of lysate from single cells. Endogenous protein targets are identifiable, with appreciable confidence stemming from the dual measurements of molecular mass and reactivity with an immunoprobe.

Going forward, we see a promising role for standards in single-cell protein separations, for

the understanding (or simply measurement) sources of technical variation and for identification of unknown protein species. Each stage of the microfluidic immunoblot from cell lysis to immunoprobing can now be assessed to determine dominant contributors to variation in measurements of peak location and protein expression. With careful design to deliver controlled (and known) quantities of standard proteins to each microwell, protein ladders have the potential to aid in absolute protein quantitation from each single-cell lysate.

Bibliography

1. Amir, E. A. D. *et al.* ViSNE enables visualization of high dimensional single-cell data and reveals phenotypic heterogeneity of leukemia. *Nature Biotechnology* **31,** 545–552. ISSN: 10870156 (2013).
2. Powell, A. A. *et al.* Single Cell Profiling of Circulating Tumor Cells : Transcriptional Heterogeneity and Diversity from Breast Cancer Cell Lines. **7.** doi:10.1371/journal.pone.0033788 (2012).
3. Werner, M. *et al.* Microfluidic Single-Cell Analysis with Affinity Beads. *Small* **11,** 2607–2613. ISSN: 16136810 (2015).
4. Zhang, X. *et al.* Quantitative Analysis of Multiple Proteins of Different Invasive Tumor Cell Lines at the Same Single-Cell Level. *Small* **14,** 1703684. ISSN: 16136810 (2018).
5. Sinkala, E. *et al.* Profiling protein expression in circulating tumour cells using microfluidic western blotting. *Nature Communications* **8,** 14622. ISSN: 2041-1723 (2017).
6. Streets, A. M. *et al.* Microfluidic single-cell whole-transcriptome sequencing. *Proceedings of the National Academy of Sciences of the United States of America* **111,** 7048–53. ISSN: 1091-6490 (2014).
7. Arzalluz-Luque, Á. *et al.* Delineating biological and technical variance in single cell expression data. *International Journal of Biochemistry and Cell Biology* **90,** 161–166. ISSN: 18785875 (2017).
8. Jiang, L. *et al.* Synthetic spike-in standards for RNA-seq experiments. *Genome Research* **21,** 1543–1551. ISSN: 10889051 (2011).
9. Islam, S. *et al.* Quantitative single-cell RNA-seq with unique molecular identifiers. *Nature Methods* **11,** 163–166. ISSN: 15487091 (2014).
10. Schwartz, A. *et al. Standardizing flow cytometry: A classification system of fluorescence standards used for flow cytometry* 1998. doi:10.1002/(SICI)1097-0320(19981001)33:2<106::AID-CYTO4>3.0.CO;2-H.
11. Shi, Q. *et al.* Single-cell proteomic chip for profiling intracellular signaling pathways in single tumor cells. *Proceedings of the National Academy of Sciences of the United States of America* **109,** 419–24. ISSN: 1091-6490 (2012).

12. Hu, S *et al.* Capillary sodium dodecyl sulfate-DALT electrophoresis of proteins in a single human cancer cell. *Electrophoresis* **22,** 3677–3682. ISSN: 0173-0835 (2001).

13. Chen, X. *et al.* Single-Microchannel, Multistep Assay Reports Protein Size and Immunoaffinity. *Analytical Chemistry* **83,** 6573–6579. ISSN: 0003-2700 (2011).

14. Hughes, A. J. & Herr, A. E. Microfluidic Western blotting. *Proceedings of the National Academy of Sciences* **109,** 21450–21455 (2012).

15. Herr, A. E. & Singh, A. K. Photopolymerized cross-linked polycrylamide gels for on-chip protein sizing. *Analytical Chemistry* **76,** 4727–4733. ISSN: 00032700 (2004).

16. Gomis, D. B. *et al.* Size-based separations of proteins by capillary electrophoresis using linear polyacrylamide as a sieving medium: Model studies and analysis of cider proteins. *Electrophoresis* **24,** 1391–1396. ISSN: 01730835 (2003).

17. Kyhse-Andersen, J. Electroblotting of multiple gels: a simple apparatus without buffer tank for rapid transfer of proteins from polycrylamide to nitrocellulose. *Journal of Biochemical and Biophysical Methods* **10,** 203–209. ISSN: 0165-022X (1984).

18. Mahmood, T. & Yang, P.-C. Western blot: technique, theory, and trouble shooting. *North American journal of medical sciences* **4,** 429–34. ISSN: 1947-2714 (2012).

19. Uliana, C. V. *et al.* Fully disposable microfluidic electrochemical device for detection of estrogen receptor alpha breast cancer biomarker. *Biosensors and Bioelectronics* **99,** 156–162. ISSN: 09565663 (2018).

20. Shapiro, A. L., Viñuela, E. & V. Maizel Jr., J. Molecular weight estimation of polypeptide chains by electrophoresis in SDS-polyacrylamide gels. *Biochemical and Biophysical Research Communications* **28,** 815–20. ISSN: 10902104 (1967).

21. Ferguson, K. A. Starch-gel electrophoresis–application to the classification of pituitary proteins and polypeptiedes. *Metabolism: clinical and experimental* **13,** 985–1002. ISSN: 0026-0495 (1964).

22. Burnette, W. N. "Western Blotting": Electrophoretic transfer of proteins from sodium dodecyl sulfate-polyacrylamide gels to unmodified nitrocellulose and radiographic detection with antibody and radioiodinated protein A. *Analytical Biochemistry* **112,** 195–203. ISSN: 10960309 (1981).

23. Bowen, B. *et al.* The detection of DNA-binding proteins by protein blotting. *Nucleic Acids Research* **8,** 1–20. ISSN: 03051048 (1980).

24. Rettig, J. R. & Folch, A. Large-scale single-cell trapping and imaging using microwell arrays. *Analytical Chemistry* **77,** 5628–34. ISSN: 00032700 (2005).

25. Revzin, A. *et al.* Development of a microfabricated cytometry platform for characterization and sorting of individual leukocytes. *Lab on a Chip* **5,** 30–7. ISSN: 14730197 (2005).

26. Di Carlo, D., Aghdam, N. & Lee, L. P. Single-cell enzyme concentrations, kinetics, and inhibition analysis using high-density hydrodynamic cell isolation arrays. *Analytical Chemistry* **78,** 4925–30. ISSN: 00032700 (2006).

27. Duncombe, T. A. *et al.* Hydrogel Pore-Size Modulation for Enhanced Single-Cell Western Blotting. *Advanced Materials.* ISSN: 15214095. doi:10.1002/adma.201503939 (2016).

28. Kang, C. C. *et al.* Single cell-resolution western blotting. *Nature Protocols.* ISSN: 17502799. doi:10.1038/nprot.2016.089 (2016).

29. Kim, J. J., Sinkala, E. & Herr, A. E. High-selectivity cytology via lab-on-a-disc western blotting of individual cells. *Lab on a Chip* **17,** 855–863. ISSN: 1473-0197 (2017).

30. Kang, C. C. *et al.* Single-cell western blotting after whole-cell imaging to assess cancer chemotherapeutic response. *Analytical Chemistry* **86,** 10429–10436. ISSN: 15206882 (2014).

31. Kang, C.-C. *et al.* Electrophoretic cytopathology resolves ERBB2 forms with single-cell resolution. *npj Precision Oncology* **2,** 10. ISSN: 2397-768X (2018).

32. Lee, K. Y. & Yuk, S. H. Polymeric protein delivery systems. *Progress in Polymer Science* **32,** 669–697. ISSN: 0079-6700 (2007).

33. Varghese, S. & Elisseeff, J. H. in, 95–144 (Springer, Berlin, Heidelberg, 2006). doi:10.1007/12_072.

34. Prokop, A. *et al.* in *Filled Elastomers Drug Delivery Systems* 119–173 (Springer Berlin Heidelberg, Berlin, 2002). doi:10.1007/3-540-45362-8_3.

35. Janes, K., Calvo, P. & Alonso, M. Polysaccharide colloidal particles as delivery systems for macromolecules. *Advanced Drug Delivery Reviews* **47,** 83–97. ISSN: 0169-409X (2001).

36. Huang, C.-H. Phosphatidylcholine vesicles. Formation and physical characteristics. *Biochemistry* **8,** 344–352. ISSN: 0006-2960 (1969).

37. Bangham, A. D. Lipid Bilayers and Biomembranes. *Annual Review of Biochemistry* **41,** 753–776. ISSN: 0066-4154 (1972).

38. Fonseca, M. J., Alsina, M. A. & Reig, F. Coating liposomes with collagen (Mr 50,000) increases uptake into liver. *Biochimica et biophysica acta* **1279,** 259–65. ISSN: 0006-3002 (1996).

39. McFadden, M. J., Junop, M. S. & Brennan, J. D. Magnetic "Fishing" Assay To Screen Small-Molecule Mixtures for Modulators of Protein-Protein Interactions. *Analytical Chemistry* **82,** 9850–9857. ISSN: 0003-2700 (2010).

40. Ohyama, K. *et al.* Immune complexome analysis of serum and its application in screening for immune complex antigens in rheumatoid arthritis. *Clinical chemistry* **57,** 905–9. ISSN: 1530-8561 (2011).

41. Carrick, B. H. *et al.* A Novel Recombinant DNA System for High Efficiency Affinity Purification of Proteins in Saccharomyces cerevisiae. *G3 (Bethesda, Md.)* **6,** 573–8. ISSN: 2160-1836 (2015).

42. Ananth, A. *et al.* Reversible Immobilization of Proteins in Sensors and Solid-State Nanopores. *Small* **14,** 1703357. ISSN: 16136810 (2018).

43. Hughes, A. J. *et al.* Single-cell western blotting. *Nature Methods* **11,** 749–755. ISSN: 1548-7091 (2014).

44. Khan, F., He, M. & Taussig, M. J. Double-hexahistidine tag with high-affinity binding for protein immobilization, purification, and detection on Ni-nitrilotriacetic acid surfaces. *Analytical Chemistry* **78,** 3072–3079. ISSN: 00032700 (2006).

45. Luo, S., Feng, J. & Pang, H. M. High-throughput protein analysis by multiplexed sodium dodecyl sulfate capillary gel electrophoresis with UV absorption detection. *Journal of Chromatography A* **1051,** 131–134. ISSN: 00219673 (2004).

46. Matheron, G. Principles of geostatistics. *Economic Geology* **58,** 1246–1266. ISSN: 1554-0774 (1963).

47. Cressie, N. Fitting variogram models by weighted least squares. *Journal of the International Association for Mathematical Geology* **17,** 563–586. ISSN: 0020-5958 (1985).

48. Becker, G. *et al.* Surface-attached poly(phosphoester)-hydrogels with benzophenone groups. *Polymer Chemistry* **9,** 315–326. ISSN: 1759-9954 (2018).

49. Sundberg, R. J. & Martin, R. B. Interactions of histidine and other imidazole derivatives with transition metal ions in chemical and biological systems. *Chemical Reviews* **74,** 471–517. ISSN: 0009-2665 (1974).

50. Vlassakis, J. & Herr, A. E. Joule Heating-Induced Dispersion in Open Microfluidic Electrophoretic Cytometry. *Analytical Chemistry* **89,** 12787–12796. ISSN: 0003-2700 (2017).

51. Martegani, M. P. *et al.* Structural variability of CD44v molecules and reliability of immunodetection of CD44 isoforms using mAbs specific for CD44 variant exon products. *The American journal of pathology* **154,** 291–300. ISSN: 0002-9440 (1999).

52. Figtree, G. A. *et al.* Truncated Estrogen Receptor α 46-kDa Isoform in Human Endothelial Cells. *Circulation* **107,** 120 –126 (2003).

53. Inoue, K. & Fry, E. A. Aberrant Splicing of Estrogen Receptor, HER2, and CD44 Genes in Breast Cancer. *Genetics & epiGenetics* **7,** 19–32 (2015).

Chapter 4

Single-cell electrophoretic cytology resolves estrogen receptor isoforms and refines taxonomy for understanding hormonal responses in breast cancer

Materials reproduced from: J.J. Kim, C.C. Kang, M.D. Pegram, and A.E. Herr, Single-cell electrophoretic cytology resolves estrogen receptor αisoforms and refines taxonomy for understanding hormonal responses in breast cancer, 2018

4.1 Introduction

Breast cancer (BCa) is a heterogeneous disease, classified into 4 subtypes based on amplification of estrogen receptor (ER), progesterone receptor (PR), and human epidermal growth factor receptor 2 (HER2/neu) via immunohistochemistry staining [1–3]. Annually, almost 80% of BCa cases is ER-α^+, and the ER-α protein mediates cancer proliferation by translocating into nucleus [1, 4]. Patients with ER-α^+ usually receive hormone therapy (e.g., tamoxifen – which turns into antiestrogen metabolites that bind to estrogen receptors and prevent transcription of estrogen-responsive genes) and have an estimated 5-year survival rate of 84% [5–7]. In contrast, BCa subtypes with an absence of ER-αusually exhibit aggressive phenotypes and develop resistance to hormone therapy [1, 8–10].

Despite of progress in genomic sequencing to identify driver mutations at a single-cell level [11–13], protein variation needs to be further measured to understand hormone resistance and other complex biological processes [14, 15]. In BCa, variants of estrogen receptors (ER-α66, ER-α46, ER-α36) are consisted of different molecular structures and functions due to alternative splicing, localized in different subcellular compartments, and involved in dif-

ferent signaling pathways (genomic vs. non-genomic) that respond cancer cells differently to tamoxifen and hormone drugs [16–21]. Elucidating how cancers change from 'responsive' to 'resistant' may enhance the efficacy of hormone cancer therapies by unlocking knowledge that could 'switch' drug-resistant cancers back to drug-responsive cancers. While the mechanisms of drug resistance are unclear, overexpression of a truncated ER-α isoform (ER-α46) partially recovers hormone therapy responses in hormone-resistant BCa cell lines [19, 22].

Consequently, to understand the drug resistance mechanism, we report on a high-selectivity cytometry capable of classifying BrCa using both truncated ER-α46 and full-length ER-α66 proteins. Such a single-cell assay is unavailable, as immunoassays are insufficiently selective owing to a high percentage of amino-acid sequence overlap between ER-α46 and ER-α66 [22]. We report on design and application of a high-throughput microdevice that distinguishes large (canonical) and small (truncated) proteins from single cells by prepending an electrophoretic separation of proteins to a backend immunoassay [23, 24]. The single-cell western blot (scWestern) is a two-stage assay design that allows us to utilize existing antibodies for ER-α while offering a selectivity (based on molecular-mass differences) unachievable with immunoassays. With the scWestern, we investigate changes in ER-αsignaling pathways in BCa cell lines by multiplexing protein targets at a single-cell resolution.

4.2 Materials and Methods

SU-8 soft lithography and scWestern fabrication

A polyacrylamide gel was polymerized against a silicon wafer with SU-8 micropillars for microwells. After cleaning a mechanical grade silicon wafer (University Wafers) surface with isopropanol and acetone, a 30 µm SU-8 3050 (Y311075; MicroChem) layer was coated by spinning at 4000 RPM for 30 s and soft baked at 95 °C for 15 min. Then, the wafer was soft baked at 95 °C for 15 min, and exposed to UV (40 mW/cm ^{2}, 5 s) under a Mylar mask with the microwell array design (250 µm well-to-well spacing and 1 mm long separation lane). Followed by post-exposure baking (65 °C for 1 min, 95 °C for 5 min), the wafer was immersed in SU-8 developer (Y020100; Microchem) to reveal the micropillars. Before casting a polyacrylamide gel, the wafer was coated with 100 µl hydrophobic dichlorodimethylsilane (DMDCS, 440272; Sigma-Aldrich) via vapor-deposition for 40 min under vacuum. The SU-8 mold's thickness was measured by using a surface profilometer (Sloan Dektak 3030) with a 0.10 mN stylus force. By casting on the SU-8 mold, the 30-µm polyacrylamide gel layer with patterned microwells was chemically polymerized using 8% T, 3.45% C, 3 mM BPMAC, 0.08% APS and 0.08% TEMED.

Cell lines and cell culture

MCF-7, MDA-MB-231, SKBR3, HEK293, and ZR-75-1 were obtained from the American Type Culture Collection (ATCC). BT474 was obtained from Dr. Mark Pegrams laboratory.

SKBR3 was cultured in McCoys 5A (16600082; Thermofisher Scientific) supplemented with 1% penicillin/streptomycin (P/S; 15140122; Thermofisher Scientific) and 10% fetal bovine serum (FBS; 100-106; Gemini Bio-Products). HEK293 was cultured in Eagle's Minimum Essential Medium (EMEM) (30-2003; ATCC) supplemented with 1% P/S and 10% FBS. MCF-7, MDA-MB-231, ZR-75-1, and BT474 were maintained in RPMI 1640 (11875-093; Thermofisher Scientific), supplemented with 1% P/S and 10% FBS. All cell lines were incubated in a humidified incubator held at 37 °C under 5% CO_2. All cell lines were authenticated using short tandem repeat analysis by UC Berkeley Cell Culture Facility.

Tamoxifen and E2 treatment

Prior to drug treatment, cells were incubated in phenol free RPMI1640 (11835030; Thermofisher Scientific) and charcoal stripped FBS (A3382101; Thermofisher Scientific) with 1% P/S for 48 h. Tamoxifen (T5648; Sigma-Aldrich) and E2 (E8875; Sigma-Aldrich) were dissolved in 100% EtOH and prepared at 1 mM concentration. Cells were treated with E2 or TAM with final concentration of 1 M for 24 h. For negative control, cells were treated with 100% EtOH with equal volume of E2 or TAM treatment for 24 h. After the treatment, cells were detached from cell culture dish with 10 mM EDTA (AM9260G) and proceeded with the scWestern assay.

scWestern assay procedure

The scWestern assay is composed of a 30-µm thick polyacrylamide gel (8%T, 2.7%C) patterned with an array of 30-µm microwells on a standard microscope glass slide. First, cells at 25,000 cells/ml in 1x PBS (10010023; Thermofisher Scientific) were seated in the microwells by gravitational sedimentation for 10 min. The seated cells were lysed in situ for 30 s by pouring 15 ml of chemical lysis buffer. The chemical lysis buffer is comprised of 8M Urea (U5378, Sigma Aldrich), 1% SDS (L3771; Sigma Aldrich), 0.1% Triton X-100 (X100; Sigma Aldrich), 1x Tris-glycine (D6750; Sigma Aldrich). Following the cell lysis, an electric field at 40 V/cm was applied across the scWestern device for protein acrylamide gel electrophoresis. Immediately after electrophoresis, electromigrated proteins were covalently bounded into the gel with benzophenone moieties by applying UV (Lightningcure LC5; Hamamatsu) for 45 s. Then, the scWestern device was washed with 1x TBS with Tween 20 (TBST, 77500; Affymetrix) for 1 h prior to immunoprobing. For immunoprobing, 0.1 g/l of primary and secondary antibodies (0.1 g/l) were diluted with 1x TBST with 2% BSA and probed the device for 2 h and 1 h, respectively. Between and after each probing, 1x TBST was used for washing for 1 h. Lastly, the device was dried and scanned with a fluorescence microarray scanner (4300A; Genepix).

Antibodies

Primary antibodies of α-actinin (6487; Cell Signaling), β-tubulin (ab6046; Abcam), CD44 (3570; Cell Signaling), ER-α(sp-10; Sigma Aldrich), cleaved caspase 8 (9496; Cell Signaling), cJUN (60A8; Cell Signaling), EGFR (2322; Cell Signaling), GAPDH (Sab2500450; Sigma Aldrich), Phospho-AKT(Ser473, 9231; Cell Signaling), p38 MAPK (8690; Cell Signaling), S6-ribosomal protein (Ser240/244) (5364; Cell Signaling) were immunoprobes for BCa cell lines. Secondary antibodies of anti-goat antibody with Alexa Fluor 555 (A-21432; ThermoFisher), anti-mouse antibody with Alexa Fluor 594 (A-11032), and anti-rabbit antibody conjugated with Alexa Fluor 647 (A-21245) were used as secondary antibodies. Secondary antibodies to goat IgG pre-labelled with AlexaFluor 488 and 555 (A11055 and A21432), mouse IgG pre-labelled with AlexaFluor 488 (A21202), and rabbit IgG pre-labelled with AlexaFluor 488 and 647 (A21206 and A31573) were used as prepared by the vendor (Invitrogen). For slab-gel western blotting, secondary antibodies to goat (A15999), rabbit (31460), mouse (31430) IgG labelled with HRP were used as prepared by the vendor (ThermoFisher).

Slab-gel western blotting

Cells from a 10 cm petri dish at 80% confluency were lysed with a radioimmunoprecipitation buffer and centrifuged to collect proteins. Each sample was boiled at 95°C for 5 min and separated on a 10% SDS-PAGE and transferred on a nitrocellulose membrane using a semi-dry blot machine (Pierce Power Blotter; ThermoFisher). The membrane was blocked with 1X TBST buffer with 5% FBS for 1 h. The membrane was incubated with a primary antibody (1:15,000) for overnight at 4 °C and washed with 1X TBST buffer for 1 h. The membrane was then incubated with secondary antibodies labelled with HRP for 1 h at room temperature. After washing with 1X TBST for 1 h, the membrane was incubated with HRP chemiluminescent substrate (SuperSignal West Dura Substrate, 34076; ThermoFisher) for 5 min and detected with a CCD imager (ChemiDoc XRS+, Bio-Rad).

Cell fixing and flow cytometry

MCF-7 and MDA-MB-231 cells were collected at 10^6 cells/ml. The cells were fixed with 4% formaldehyde (12606; Cell Signaling) for 10 min at 37 °C. The cells were permeabilized with 90% MeOH for 30 min on ice. After washing the cells with an incubation buffer (1x PBS with 2% FBS) twice, the cells were resuspended in 100 µl of primary antibody (1:50) and incubated at room temperature for 1 h. The cells were washed again with the incubation buffer and incubated with secondary antibody (1:150) for 30 min at room temperature. The cells were washed again with the incubation buffer and analyzed by using Attune NxT Flow Cytometer (Thermo Fisher Scientific). Viable cells were gated on size and shape using forward and side scatters. The cytometer was set at 200 cells/ml. FITC fluorescence was collected in the BL1 channel using a 480/500 nm band-pass filter.

scWestern data analysis and processing

Images were processed by applying a median filter with a 2-pixel radius and a threshold value of 50 (ImageJ). Protein peaks from the scWestern were quantitated with in-house MATLAB scripts [23]. The peaks were fitted by Gaussian functions in MATLAB (R2016b) and processed by extracting Gaussian parameters for peak width, location, and area-under-curve for protein expression. The protein peaks with Gaussian fitting $R^2 \geq 0.7$ and SNR $>$ 3 were analyzed [23].

4.3 Results and Discussion

Validation of ER-α antibodies with BCa cell lines

In order to distinguish ER-α66 and ER-α46, we sought to screen for a specific and sensitive antibody by testing a panel of antibodies with model BCa cell lines in conventional immunoassays. The cell lines are mycoplasma negative and authenticated with 100% match in the short tandem repeat analysis. Largely, commercial antibodies recognize the ER-α C-terminus, which is conserved in both ER-α66 and ER-α46 (Figure 4.1A, S1). The difference in amino acid sequence between ER-α66 and ER-α46 is the AF1 transactivation domain at the N-terminus (Figure 4.1A). Validation of three commercial anti-ER-α antibodies (SP-1, H226, and HC-20) was carried out by slab-gel western blotting of lysates pooled from 10^6 cells. The SP-1 and HC-20 antibodies bind to epitopes in the ligand-binding region at the C-terminus, while H226 recognizes a hinge region in both ER-α isoforms. The SP-1 antibody detected ER-α66 and ER-α46 in an MCF-7 lysate but only detected ER-α46 in MDA-MB-231 and HEK293 lysates (Figure 1B). Comparing the population-average ER-α46 expression ratio (ER-α46/GAPDH), the MDA-MB-231 lysate had a 1.8-fold higher ER-α46/GAPDH expression ratio than the HEK293 lysate (Figure 4.1B). The H226 and HC-20 antibodies, which detected similar ER-α expression patterns across the model cell lines, generated non-specific protein expressions in locations near the expected ER-α isoforms. Using slab-gel western blotting to test ER-α antibodies with $>$ 4 BCa cell lines, we found that SP-1 was capable of correctly identifying ER-α isoforms, with only a single band of non-specific binding at 100 kDa (Figure 4.1B, Table 4.1, Figure S1).

ER-α Antibody	**Epitope region**	**Isoforms**	**Company (catalog no.)**
SP-1	C-terminus (578 595 aa)	ER-α66, ER-α46	Abcam (ab16660)
HC-20	C-terminus	ER-α66, ER-α46	Santa Cruz (sc-543)
MC-20	C-terminus	ER-α66	Santa Cruz (sc-542)
C3 (H-300)	C-terminus (579 599 aa)	ER-α66, ER-α46	Santa Cruz (sc-20137)
H226	Hinge region D	ER-α66, ER-α46, ER-α36	Santa Cruz (sc-53493)
F-10	C-terminus (576-595 aa)	ER-α66, ER-α46	Santa Cruz (sc-8002)
D-12	N-terminus (2-185 aa)	ER-α66	Santa Cruz (sc-8005)

Table 4.1: List of commercial ER-α antibodies tested in conventional western blotting for ER-α selectivity

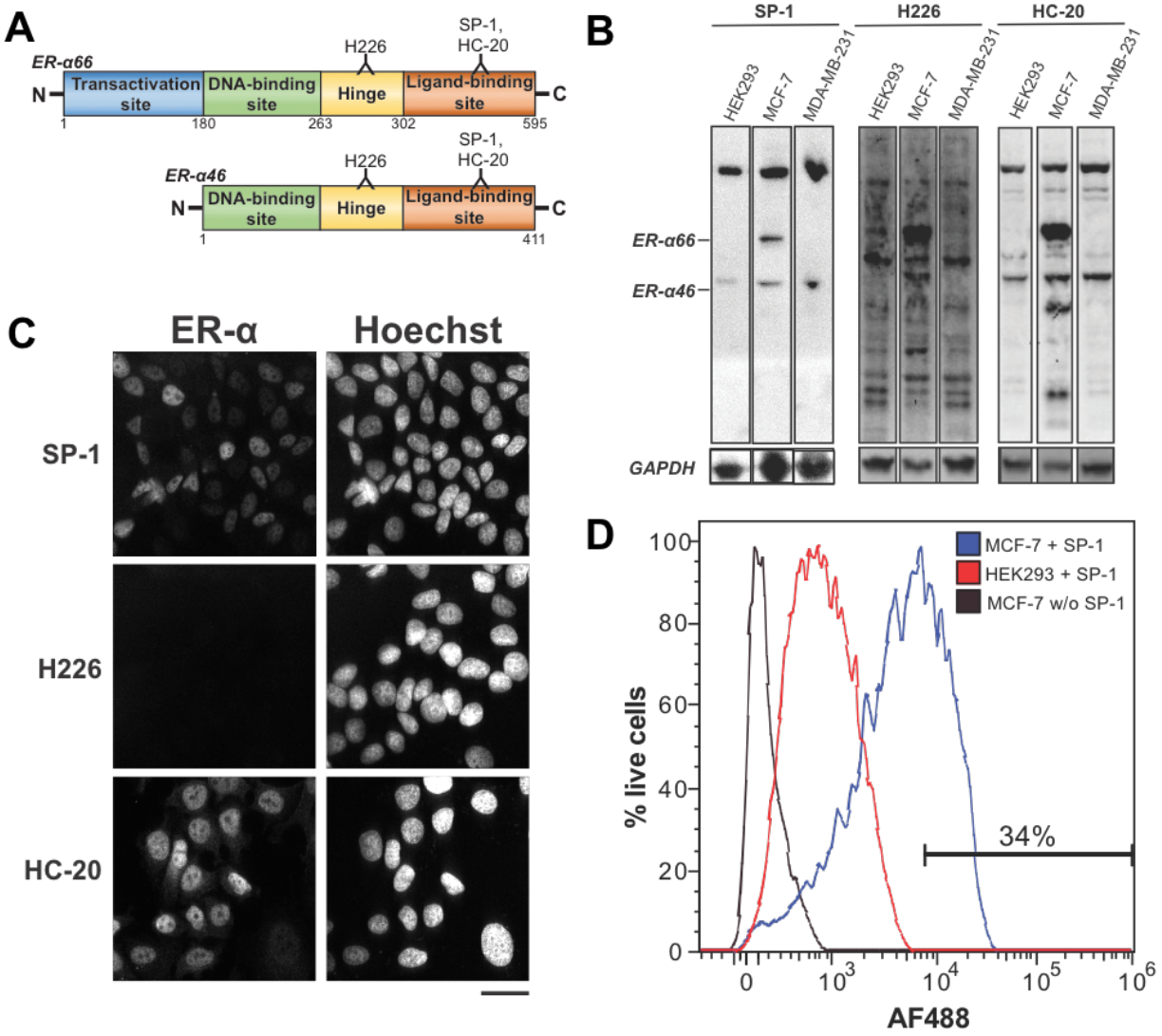

Figure 4.1: Quantitative measurement of estrogen receptor α (ER-α) isoforms is limited by antibody selectivity and non-specificity. (A) An illustration of two ER isoforms (ER-α66, ER-α46) and ER-αantibody binding locations. (B) Slab-gel western blotting with ER-αantibodies. Molecular sizing renders additional specificity to detect ER-αisoforms and non-specific signals. (C) Confocal images of MCF-7 cells fixed and probed with ER-αantibodies. Scale bar, 50 µm. (D) Line histogram of percent live cells with ER-α in fluorescence-activated cell sorting. $n_{\text{MCF-7+SP-1}} = 8691$, $n_{\text{MCF-7 without SP-1}} = 5399$, $n_{\text{HEK293 + SP-1}} = 9155$.

A

Lane	1	2	3	4	5	6
Cell Line	BT474	HEK293	MCF-7	MDA-MB-231	SKBR3	ZR-75-1

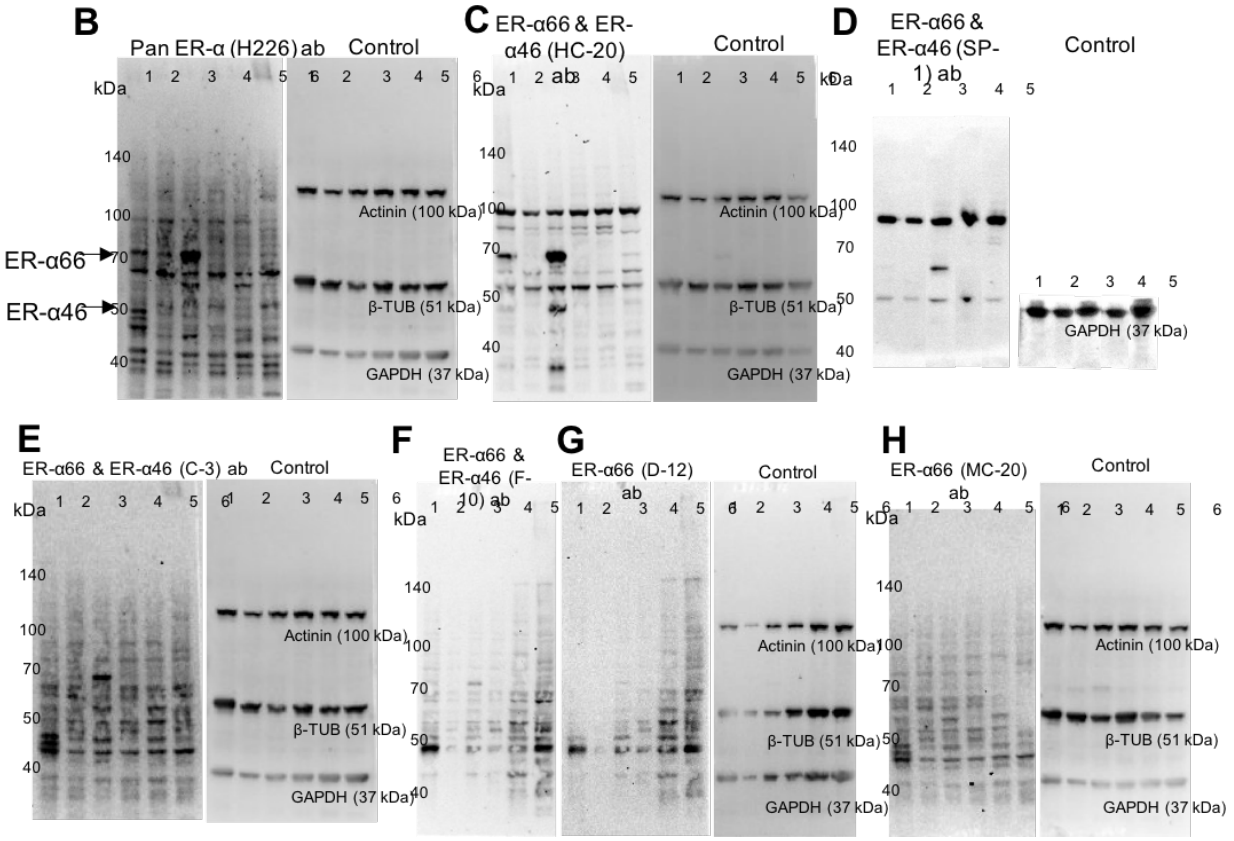

Figure 4.2: Conventional western blots to validate ER-αantibodies with model breast and kidney cancer cell lines. (A) Table of cell lines to test antibodies: BT474 (ER-α66$^+$), HEK293 (ER-α66$^-$), MCF-7 (ER-α66$^+$), MDA-MB-231 (ER-α66$^-$), SKBR3 (ER-α66$^-$), ZR-75-1 (ER-α66$^+$). Conventional western blots of ER-αwith (C) H226, (D) HC-20, (E) SP-1, (F) C-3, (G) F-10, (H) D-12, (I) MC-20 antibodies.

Next, we continued the validation testing of the three ER-α antibodies using immunocytochemistry (ICC, Figure 1C). Since ER-α is a family of nuclear receptors, we performed ICC staining in order to verify that ER-α probing is dominantly expressed in the cell nucleus. In MCF-7 cells, SP-1 and HC-20 antibody staining overlapped with Hoechst staining, which indicates the presence of ER-α receptors in the cell nucleus (Figure 4.1B). In contrast, H226 antibodies failed to detect any ER-α, possibly because of the masking of the hinge amino acid region in fixed cells, rendering it unavailable for antibody binding. ICC with SP-1 and

HC-20 antibodies was capable of confirming the presence of ER-α by spatial localization, but was not able to selectively distinguish between ER-α66 and ER-α46 (Figure 4.1C). Quantitatively, using fluorescence-activated cell sorting (FACS), we discovered that SP-1 was capable of identifying 34% of the ER- in the MCF-7 cells, compared with the ER-α^- HEK293 cells (Figure 4.1D). Given the same gating, $<$ 1% of the MDA-MB-231 cells are detected with ER-α^+ in the MDA-MB-231 cells (Figure 4.3). With the ER-αantibodies validated across immunoassays, we were able to perform scWestern assays to discern the presence of ER-α46 and ER-α66 at a single-cell resolution.

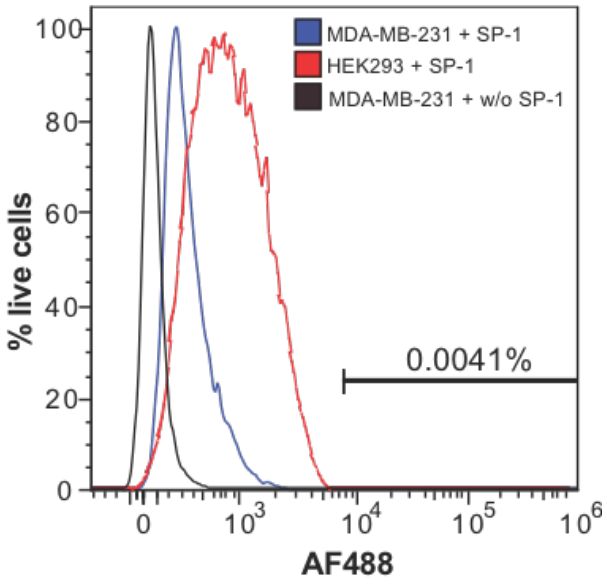

Figure 4.3: Line histogram of percent live MDA-MB-231 cells with ER-αin fluorescence-activated cell sorting. HEK293 cell line was used as a negative control. $n_{\text{MDA-MB-231+SP-1}} = 24229$, $n_{\text{MDA-MB-231 without SP-1}} = 24653$, $n_{\text{HEK293 without SP-1}} = 9155$.

Single-cell measurement of proteins and analysis of expression and signal to noise ratio variations

For analysis of ER-α isoforms, we performed quality control on the scWestern data and investigated the variability of signal-to-noise ratio (SNR) and expression (area under the curve, AUC) of β-TUB from individual cells in the scWestern. Due to the phenomenon of diffusion during electrophoresis, protein peaks are normally distributed and accordingly fitted by a Gaussian function along the separation axis for each region of interest (ROI) (Figure 4.4A). For each individual separation, the Gaussian constants from fitting represent scWestern parameters (peak amplitude, location, and width), and are used to calculate the AUC and SNR values. For quality control, we excluded the single-cell data below 0.7 for R^2 and 3 for SNR (Figure 4.4A).

Next, we assessed variations in scWestern data by analyzing AUC and SNR of β-TUB within the device and across two device replicates, from MCF-7 and MDA-MB-231 cells without any treatments. Within each replicate, we calculated the coefficient of variation (CV) based on the AUC of individual β-TUB peaks. The CV values for the AUC in the two MCF-7 replicates were 68% and 60% (Figure 4.4B). Similarly, the CV values for the SNR in the MCF-7 replicates were 60% and 59%. In the MDA-MB-231 cells, we observed greater CV values for SNR (77% and 98%) than for AUC (102% and 112%, Figure S3C). Of note, the CV values were greater than a technical variation cutoff of 32.4%, reported in a previous scWestern [25]. For the device-to-device variations, as expected, we observed no significant differences in AUC and SNR distributions between two replicates for either MCF-7 or MDA-MB-231 cells (Figure Figure 4.4B,C).

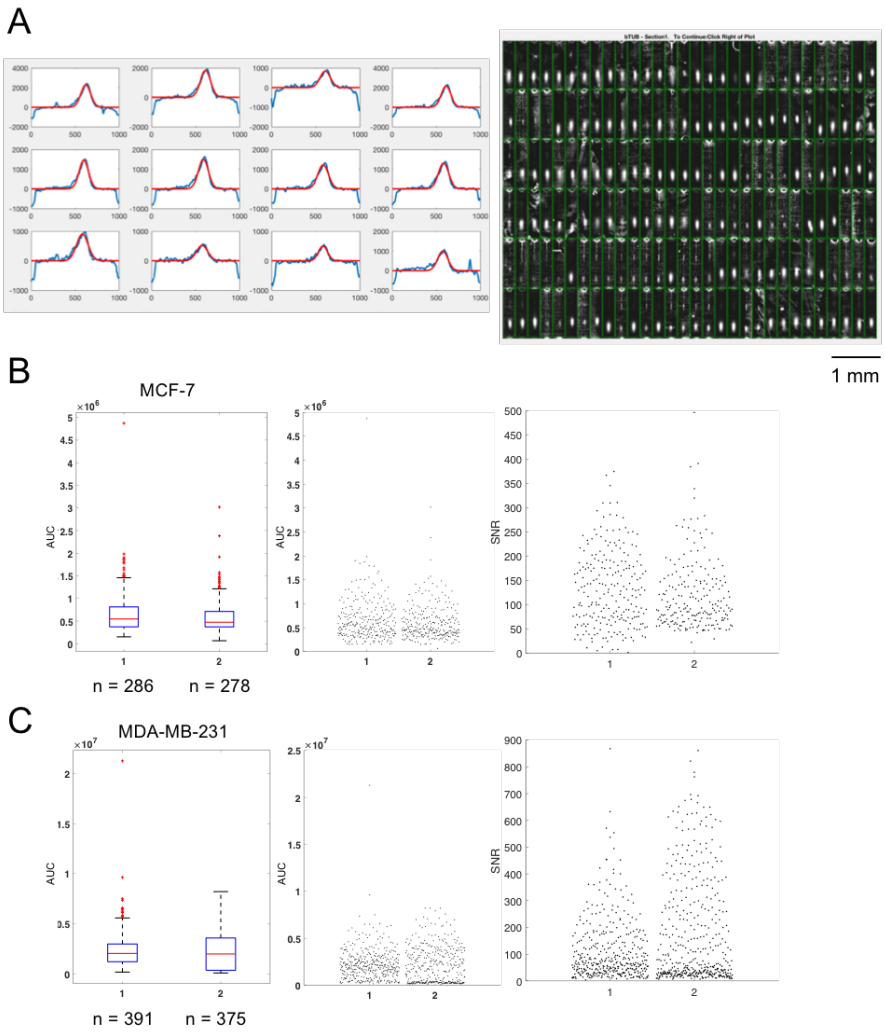

Figure 4.4: SNR and AUC variability of β-TUB within a scWestern device and between two replicate devices. (A) Gaussian curve fit and quality control ($R^2 \geq 0.7$, SNR ≥ 3) are performed for each β-TUB peak. Left: a montage of intensity plots with a blue line indicating a β-TUB signal and a red line denoting a Gaussian curve fit. Right: ROI images of β-TUB are displayed after performing quality check on curve fitting. AUC and SNR of β-TUB of individual (B) MCF-7 and (C) MDA-MB-231 cells from two device replicates are illustrated by boxplots and beeswarm plots. Each dot represents β-TUB expression of individual cell. For MCF-7: $n_1 = 286$, $n_2 = 278$; $CV_{AUC,1} = 68\%$, $CV_{AUC,2} = 60\%$, $CV_{SNR,1} = 60\%$, $CV_{SNR,2} = 59\%$; pAUC = 0.08, pSNR = 0.07. For MDA-MB-231: $n_1 = 391$, $n_2 = 375$; $CV_{AUC,1} = 77\%$, $CV_{AUC,2} = 98\%$, $CV_{SNR,1} = 102\%$, $CV_{SNR,2} = 112\%$; $p_{AUC} = 0.07$, $p_{SNR} = 0.17$. Kruskal-Wallis is done for all statistical tests.

scWestern enables detection of ER-α isoforms

We designed and optimized a high-throughput microdevice to resolve ER-α isoforms from individual cells. The isoform-specific scWestern identifies proteins by prepending an electrophoretic separation of proteins to a backend immunoassay. The two-stage assay design allows the utilization of ER-α antibodies that are compatible with ICC and FACS while offering both selectivity (based on molecular-mass differences) and single-cell resolution, which would be unachievable with conventional immunoassays. The isoform-specific scWestern consists of a 30 µm-thick polyacrylamide gel patterned with an array of 30 µm-diameter microwells. Each device is capable of settling ~1000 cells (Figure 4.5A). Once a solution of dissociated cells is introduced onto the scWestern, individual cells sediment into the microwells for *in-situ* cell lysis. After the cells are lysed, the proteins inside each cell are electrophoresed and sequentially immobilized by UV-activated benzophenone moieties incorporated in the polyacrylamide. To detect target proteins, we introduced antibodies labeled with different fluorescent dyes and increased multiplexing by antibody stripping and reprobing (Figure 4.5A).

In the scWestern, the *in-situ* cell lysis affects the downstream workflow of protein detection. Consequently, the cell lysis components need to be optimized for protein solubility. As ER-α binds to DNA and is dominantly present in the cell nucleus rather than the cytoplasm, we sought different detergent conditions for chemical cell lysis (Figure 4.1C, 4.5B). In the scWestern, detergent components affect protein solubility, thereby influencing protein separation resolution. We therefore tested sodium dodecyl sulfate (SDS), an anionic detergent that disrupts protein membranes and denatures proteins, at 1% and 2% (m/v) concentrations for the cell lysis. Increasing SDS concentration from 1% to 2% decreased separation resolution between ER-α66 and GAPDH from 0.73 to 0.41 (Figure 4.5B). The low separation resolution at the 2% SDS was caused by peak broadening of GAPDH and ER-α66 due to an increase in the lysis buffer conductivity (Figure 4.6). Another component we included in order to optimize cell lysis conditions was a chaotrope, urea. Urea is commonly incorporated in lysis buffers to denature proteins by disrupting hydrogen bonds and lowering detergent critical micelle concentration [26] Furthermore, 8M urea has been applied before in 2D slab-gel western blotting to solubilize ER binding complexes in the nucleus for MALDI-MS analysis [27]. In our scWestern, the inclusion of 8M urea in the lysis buffer improved separation resolution of ER-α66 and GAPDH from 0.62 to 1.72 without diminishing signal-to-noise ratio (Figures 4.5B, 4.6).

After optimizing the lysis buffer conditions with 1% SDS and 8M urea, the scWestern was performed with the three ER-α antibodies (SP-1, H226, and HC20) to identify ER-α isoforms in MCF-7, MDA-MB-231, and HEK293 cells (Figure 4.5C). The H226 and HC20 antibodies generated non-specific peaks in HEK293 and MDA-MB-23 cells, respectively (4.5C). In contrast, the SP-1 antibody distinguished ERα66 and ER-α46 in the MCF-7 cells, without producing any non-specific signals in any of the cell lines (4.5C). Hence, we decided to use the SP-1 antibody to investigate the frequency and expression levels of ER-α isoforms in

BCa cell lines.

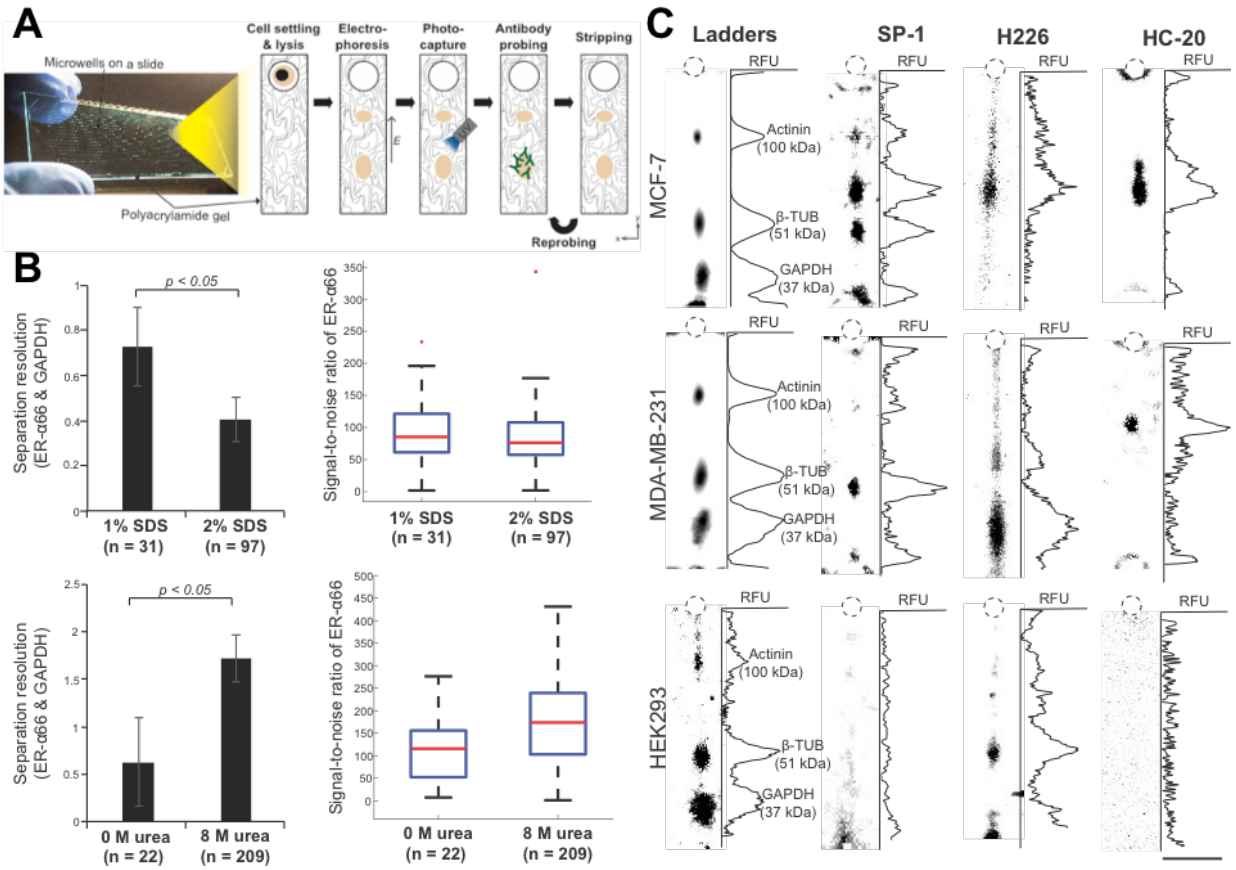

Figure 4.5: scWestern with optimized chemical-lysis conditions enables detection of ER-α66 and ER-α46 isoforms from hormone-sensitive (MCF-7) and -insensitive (MDA-MB-231) BCa cell lines. (A) Schematic procedures for the scWestern. A microarray of 30µm microwells on a slide coated with polyacrylamide gel was utilized to perform single-cell western blotting. In this method, once a cell settles down into a microwell, the cell is chemically lysed. The lysis products are then separated by electrophoresis in the polyacrylamide gel (40 V/cm, 30 s) to resolve proteins according to their molecular masses. The proteins are then photo-immobilized and probed with antibodies for specific detection. (B) Characterization of solubility and electrophoretic separation of ER-α66 under different chemical lysis conditions. Chemical lysis in gels containing 1% SDS and 8M urea yielded improved separation resolution between ER-α66 and GAPDH while maintaining a similar signal-to-noise ratio to gels without the added components. Unpaired t test for paired data was used for statistical comparison between different detergent conditions. P values < 0.05 were considered significant. (C) False-colored single-cell micrographs of ER-α isoforms detected with different ER-αantibodies from MCF-7, MDA-MB-231, and HEK293 cell lines

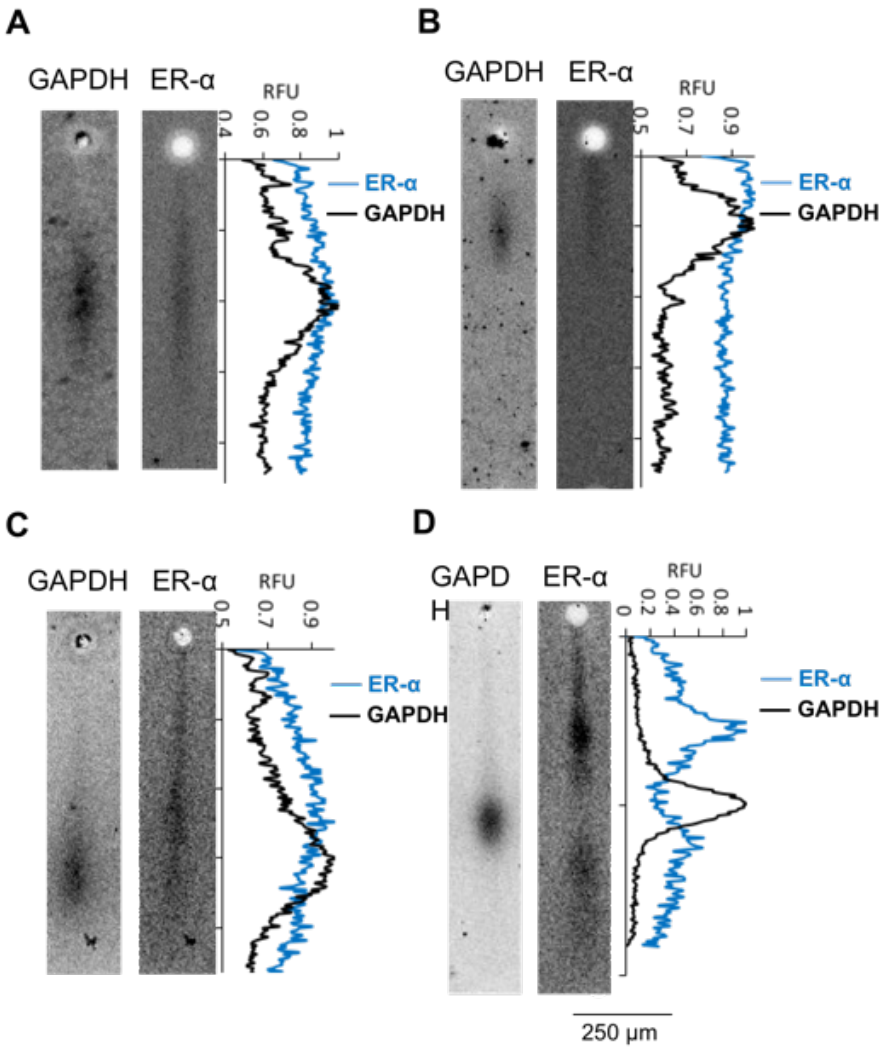

Figure 4.6: Lysis component and time optimization for detecting denatured ER isoforms in scWestern. False-color micrographs of GAPDH and ER-α and relative fluorescence units are plotted in (A) 1% SDS with 20 s lysis, (B) 2% SDS with 20 s lysis, (C) 1% SDS with 30 s lysis, (D) 1% SDS and 7M urea with 30 s lysis. ER-αand GAPDH proteins are fully denatured in (D). Following the cell lysis, an electric field at 40 V/cm is applied for 20 s to electrophorese proteins through the 8% T gel.

scWestern reveals subpopulations of ER-α isoforms in hormone-sensitive BCa

Next, we sought to investigate SP-1 antibody detection of ER-αisoforms from individual cells in the scWestern, and to measure cell-to-cell variations. To validate ER-αpeaks by

separation, three housekeeping proteins – α-actinin, β-tubulin (β-TUB), and GAPDH – were used as reference standards for the Ferguson plot analysis (Figure 4.5C, 4.7A). The higher-mass peak seen close to the microwell, lying between the α-actinin (100 kDa) and β-TUB (51 kDa) peaks, indicates ER-α66 (66 kDa) (Figure 4.7A). The lower-mass peak that is positioned below β-TUB (51 kDa) and above GAPDH (37 kDa) denotes ER-α46 (46 kDa) (Figure 4.7A). Under electrophoresis in an 8%T polyacrylamide gel, protein mobility follows a linear and negative association with the log of molecular mass [28, 29]. After conducting electrophoresis in a constant electric field (40 V/cm) for 30 s, we performed a linear regression of the protein peak location versus the log of the molecular mass. From the linear fit, we obtained 0.99 for the R^2 value, which confirmed the detection of ER-α66 and ER-α46 in the scWestern with the SP-1 antibody (Figure 4.7A).

Following the validation of the two ER-α isoforms, we sought to determine the population frequencies of these ER-α isoforms in MCF-7 cells. Based on the expression of ER-α66 and ER-α46, we discovered subpopulations with four phenotypes: ER-α66$^+$/ER-α46$^-$, ER-α66$^-$/ER-α46$^+$, ER-α66$^+$/ER-α46$^+$, ER-α66$^-$/ER-α46$^-$ (Figure 4.7B). The ER-α66$^-$/ER-α46$^-$ subpopulation constitutes 65.31% of the population, while 36.65% and 4.25% of the population express ER-α66$^+$ or ER-α46$^+$, respectively (Figure 4.7B). A small subset (2.29%) of the population expresses both ER-α isoforms. The frequencies of cells expressing ER-α as determined by the scWestern agreed with the frequency of ER-α as determined by FACS as well as by population-average expression levels of ER-α in slab-gel western blots (Figure 4.1D, 4.7C). The frequency ratio of ER-α66$^+$ to ER-α46$^+$ was 8.62 in the scWestern, which is comparable to the population-average expression ratio of ER-α66$^+$ to ER-α46$^+$ (8.67) in the slab-gel Western (Figure 4.7C).

After assessing the frequencies of both ER-α isoforms, we sought to scrutinize the expression of these ER-α isoforms in individual MCF-7 cells by summing up fluorescence signals under the ER-α peaks (Figure 4.7D). Protein peaks were calculated by performing Gaussian fitting with an $R^2 > 0.65$ and SNR > 3. In the cells expressing ER-α isoforms, the median expression level of ER-α66$^+$ was higher than that of ER-α46$^+$ ($\text{Median}_{\text{ER-α66}} = 1.18$ 10^6, $n_{\text{ER-α66}} = 189$; $\text{Median}_{\text{ER-α46}} = 8.51$ 10^5, $n_{\text{ER-α46}} = 42$). ER-α66$^+$ expression was also less dispersed than that of ER-α46$^+$ ($CV_{\text{ER-α66}} = 45.2\%$, $CV_{\text{ER-α46}} = 99.0\%$; Figure 4.7E). Interestingly, we noticed a lower median ($\text{Median}_{\text{ER-α66textsuperscript-/ ER-α46}^+} = 5.26$ 10^5, $n_{\text{ER-α66}^-\text{/ ER-α46}^+} = 6$) and a narrower distribution ($CV_{\text{ER-α66}^-\text{/ ER-α46}^+} = 36.4\%$) of ER-α46 in the subpopulation with only ER-α46$^+$ cells, compared with subpopulations expressing both ER-α isoforms, ER-α46 and ER-α66 (Figure 4.7E). Further, in the subpopulation expressing both ER-α isoforms, expression levels were linearly correlated with the Pearsons correlation coefficient of 0.70 (Figure 4.7E).

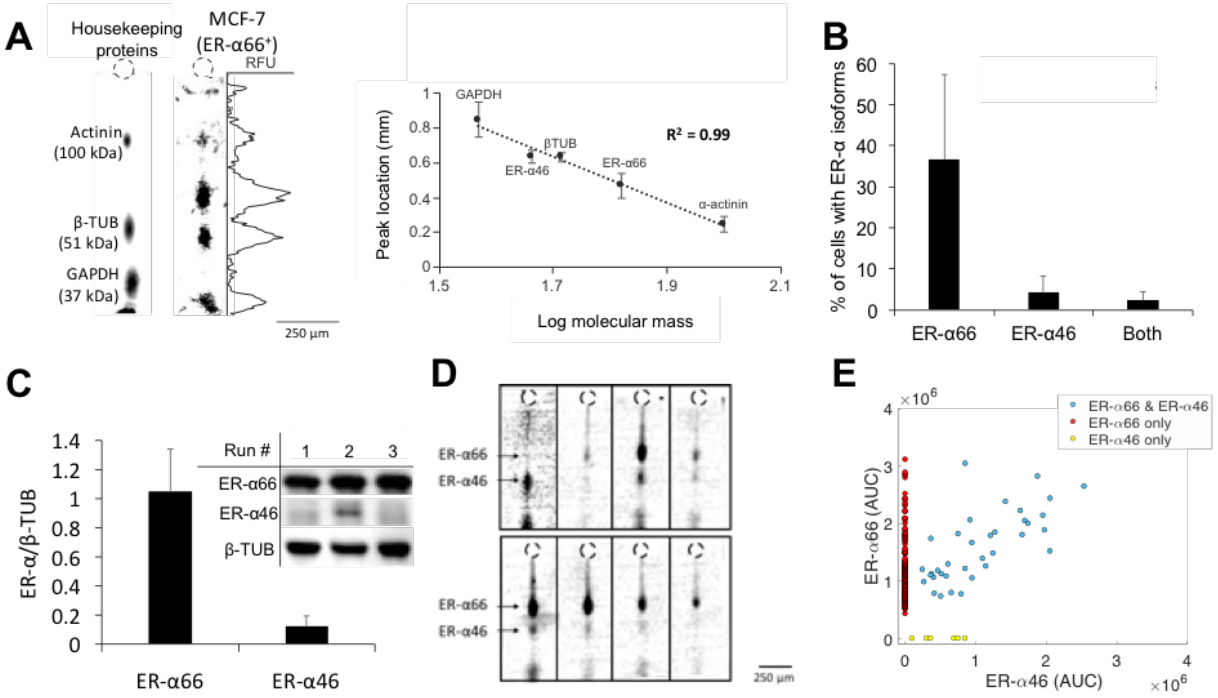

Figure 4.7: Hormone-sensitive MCF-7 cells exhibit four subpopulations ER-α66$^+$/ER-α46$^-$, ER-α66$^-$/ER-α46$^+$, ER-α66$^+$/ER-α46$^+$, and ER-α66$^-$/ER-α46$^-$, as identified by the scWestern. (A) Validation of ER-α66 and ER-α46 by comparing peak locations of these ER isoforms with those of housekeeping proteins. Micrographs of housekeeping proteins and ER-α isoforms from an MCF-7 cell are shown on the left. Ferguson plot analysis (molecular weight vs. protein peak location) with linear regression among housekeeping proteins and ER-α isoforms (y = -1.33x + 2.90, R^2 = 0.99, n = 17 for each protein peak, E = 40 V/cm) is also shown. (B) Bar graph showing subpopulation percentage of MCF-7 cells expressing ER-α isoforms (n = 5 devices). (C) Bar graph depicting population-average expression of ER-α isoforms relative to β-TUB in slab-gel western blotting. Micrographs showing protein peaks for ER-α isoforms and β-TUB from three replicates of slab-gel western blotting. (D) A sample of eight single-cell montage micrographs demonstrates bimodal expression of ER-α isoforms in MCF-7 cells. (E) A false-colored scatter plot represents expression levels of ER-α isoforms from MCF-7 subpopulations. Each dot represents an individual MCF-7 cell.

scWestern detects a rare subpopulation of truncated ER-α46 in hormone-insensitive MDA-MB-231 BCa cells

After characterizing ER-α isoforms in MCF-7 cells, we sought to understand the heterogeneity of ER-α46 expression in MDA-MB-231 cells. MDA-MB-231 is a triple-negative BCa cell line that lacks the full-length ER-α66 protein. Cancers with the triple negative genotype ex-

hibit highly invasive phenotypes [30]. As expected from previous studies, we did not discern any ER-α66 peaks from individual MDA-MB-231 cells in scWestern blots (Figure 4.8A). Further, we detected a low-frequency (2.38%) ER-α46$^+$ subpopulation in MDA-MB-231 cells (Figure 4.8A, 4.8C). This frequency in MDA-MB-231 cells was not significantly different from the frequency in MCF-7 cells (Figure 4.8C). Interestingly, the single-cell ER-α46 median expression was appreciably greater in MDA-MB-231 cells than in MCF-7 cells (Figure 4.8B). The CV of ER-α46 expression was lower in MDA-MB-231 cells (72.8%) than in MCF-7 cells (99.0%), indicating narrower ER-α46 dispersion in MDA-MB-231 cells (Figure 4.8B). The heterogeneous ER-α46 expression pattern suggests that ER-α46 may be involved in non-classical ER-α signaling pathways and thereby may affect hormone therapies differently in patients with hormone-insensitive BCa.

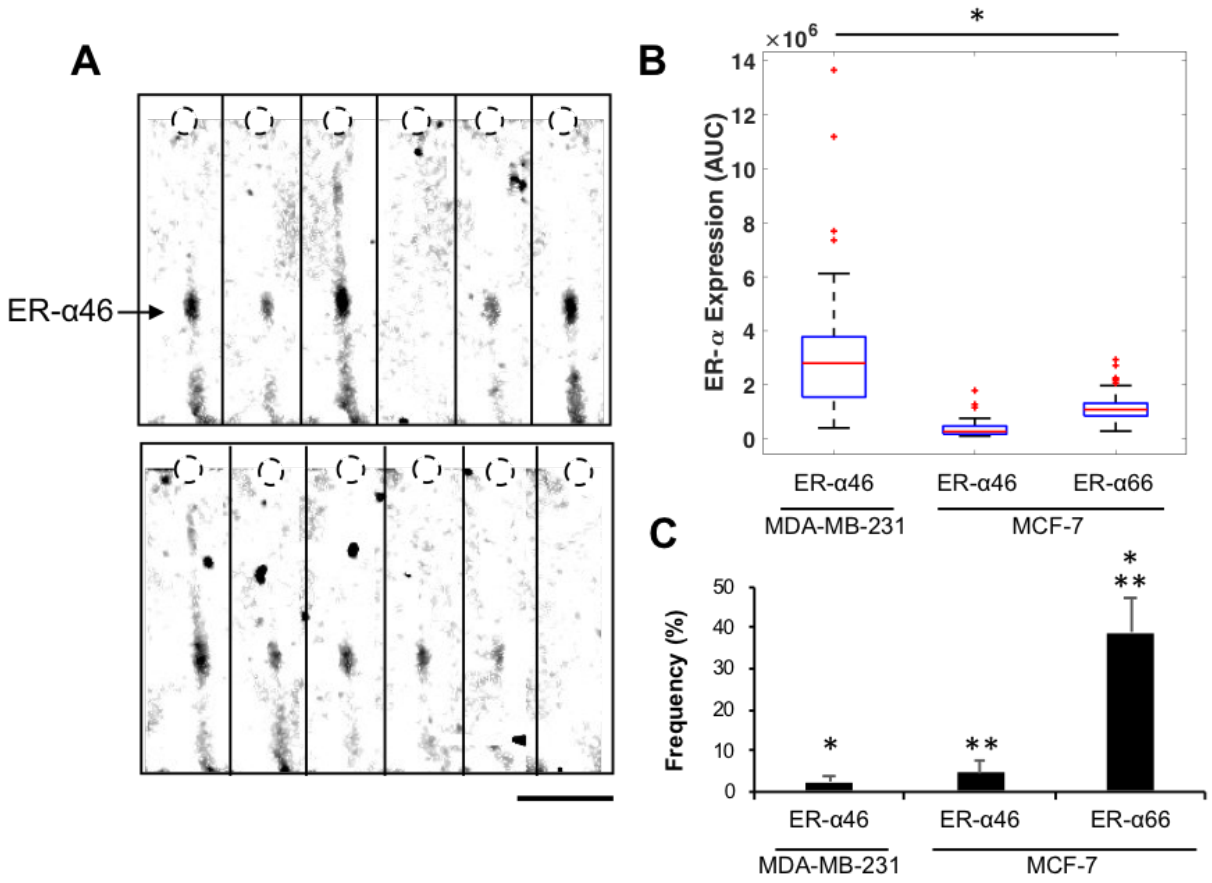

Figure 4.8: scWestern measuring ER-α46 isoform in hormone-insensitive triple-negative MDA-MB-231 BCa cells. (A) A sample of 12 false coloured single-cell montage micrographs represents cell-to-cell variations in ER-α46 expression in MDA-MB-231 cells. Scale bar, 250 µm. (B) Boxplots depict ER-αexpression levels and variation, showing differences between MCF-7 and MDA-MB-231 cells in both expression levels and expression variation (Kruskal-Wallis test with Dunn and Sidak correction, $n_{\text{MDA-MB-231}} = 64$ cells, $n_{\text{MCF-7, ER-α66}} = 18$ cells, $n_{\text{MCF-7, ER-α66}} = 139$ cells, $p < 0.001$). (C) Bar graphs illustrate the frequencies of ER-αisoforms in MDA-MB-231 and MCF-7 cells (n = 5 devices, Anova with Dunn and Sidak correction, *: significant difference between ER-α46 in MDA-MB-231 cells and ER-α66 in MCF-7 cells, **: significant difference between ER-α46 and ER-α66 in MCF-7 cells, $p < 0.05$). Differences between ER-α46 in MDA-MB-231 and MCF-7 cells were not significant.

Hormone-sensitive and hormone-insensitive BCa cells respond differently to E2 and TAM treatments

In accordance with previous studies, treatment with high-concentration (1 µM) E2 or TAM decreases population-average ER-α66 expression [31–33]. In hormone-sensitive BCa cells, E2 stimulation sustains activation of ER-α at the genomic level by inducing proteasome-dependent degradation of ER-α66 [31, 34, 35]. Given the capability of measuring ER-α isoforms at a basal level, we sought to investigate the effects of E2 and TAM on ER-α isoforms at a single-cell resolution. Before the ligand stimulation, we incubated the cells in charcoal-stripped media for 48 h to eliminate any estrogen activity originating from serum steroids. Then, we treated cells with 1 µM of either E2 or TAM for 24 h and detached the cells to perform the scWestern (Figure 4.9A) [36, 37].

In MCF-7 cells, we detected an appreciable decrease in ER-α66 expression in the E2 and TAM treatment groups, compared with the basal ER-α66 level in the non-treated group (Figure 4.9B). Intriguingly, the sizes of the ER-α66 subpopulations were not significantly different between the treated and non-treated groups (Figure 4.9B). In contrast, both the ER-α46 expression level and the size of the ER-α46 subpopulation remained consistent in the non-treated and treated MCF-7 groups (Figure 4.9B). We further delved into analyzing the subpopulation with the ER-α46$^+$/ER-α66$^+$ proteotype and uncovered a decrease in both ER-α isoforms in response to TAM, yet no difference in ER- isoforms between the non-treated and E2-treated groups (Figure 4.9C). The decreased expression levels of both ER-αisoforms in the TAM-treated group concurred with the finding that ER-α66 and ER-α46 coexpression sensitizes cells to TAM treatment (Figure 4.9C) [19].

In MDA-MB-231 cells, we discovered that ER-α46 expression levels were significantly lower in the E2- and TAM-treated groups than in the non-treated group (Figure 4.9D). The decrease in ER-α46 expression level alongside the absence of ER-α66 suggests that MDA-MB-231 and MCF-7 cells have different molecular mechanisms underlying ER-α expression. With regard to subpopulation incidence, TAM and E2 do not significantly affect the frequency of ER-α46$^+$ MDA-MB-231 cells (Figure 4.9D).

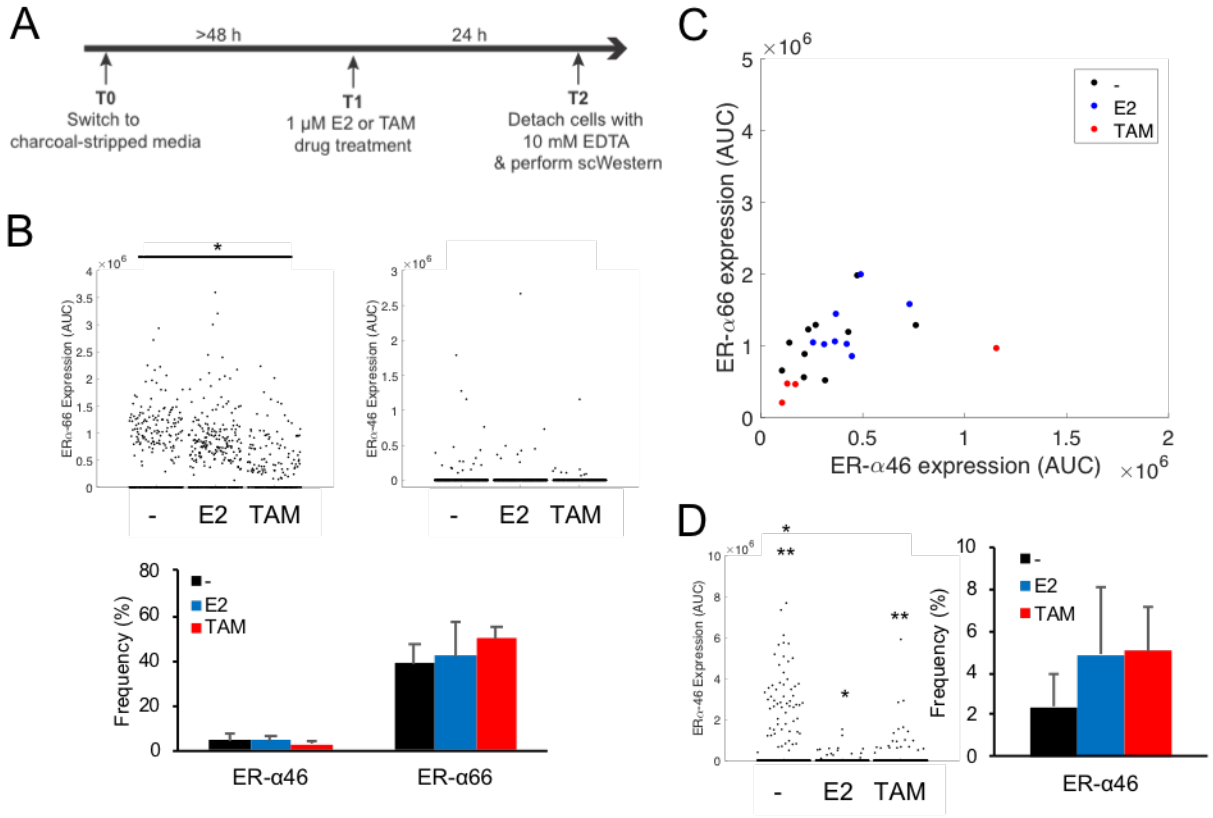

Figure 4.9: Tamoxifen and E2 treatments perturb ER-α isoforms in MCF-7 and MDA-MB-231 cells. (A) Experimental timeline for drug treatment. (B) Scatter plots (top panel) represent ER-α expression levels from individual MCF-7 cells with no treatment, E2 treatment, or TAM treatment (Kruskal-Wallis test with Dunn and Sidak correction, *$p < 0.001$). Bottom panel: frequencies of cells expressing ER-αisoforms in no-treatment, E2, and TAM groups (n = 3 devices). (C) Scatterplot representing subpopulations of ER-α46$^+$/ER-α66$^+$ in no-treatment (black), E2 (blue), and TAM (red) groups. Each dot represents ER-α expression from an individual cell.

Dissection of changes in ER-α signaling pathways in response to E2 and TAM

Given the multiplexing capability of the scWestern, we scrutinized ER-α signaling pathways in response to E2 and TAM at a single-cell resolution. ER-α isoforms are associated with estrogen response (ERE)-dependent, non-ERE, and extra-nuclear ER-α signaling pathways (Figure 4.10A) [38, 39]. We targeted two proteins associated with each of these signaling pathways (Figure 4.10B). In the nucleus, ER-αinteracts with p38-MAPK and EGFR in the ERE-dependent signaling pathway [38, 40]. The alternative, non-ERE signaling pathway is

associated with CD44 and cJUN [41, 42]. Lastly, extra-nuclear ER-α interacts with pS6 and pAKT (phosphorylation at Ser473), which are involved in the PI3K/AKT signaling pathway and modulate the non-genomic ER-α signaling pathway [38, 43]. Further, we measured cleaved caspase-8, a biomarker for cell apoptosis [44].

First, we sought to understand the effects of E2 and TAM on protein expression levels and subpopulation frequencies. In MCF-7 cells, TAM reduced the expression levels of CD44, cJUN, p38-MAPK, pS6, and cleaved caspase 8 (Figure 4.10C). Similarly, E2 lowered the expression levels of p38 MAPK and pS6 (Figure 4.10C). In contrast, we did not detect any significant changes in pAKT, cleaved caspase 8, or EGFR (Figure 4.11A). Interestingly, we also did not observe any significant changes in subpopulation frequencies, with the exception of the subpopulation expressing p38-MAPK, which decreased in frequency in response to TAM treatment (Figure 4.11B). In MDA-MB-231 cells, we found different trends in protein expression levels after E2 and TAM treatment. In particular, TAM treatment elevated the expression of cJUN, p38 MAPK, pS6, and cleaved caspase 7, yet lowered pAKT expression (Figure 4.10C). In conjunction with the elevated cJUN expression level, the subpopulation frequency of cells expressing cJUN increased after TAM treatment (Figure 4.11B). Similarly, E2 treatment elevated the expression of cJUN, p38 MAPK, and pS6, yet lowered pAKT expression. Comparing E2 and TAM expression, we observed a significant increase in p38 MAPK expression and a decrease in pS6 in the TAM group (Figure 4.10D). In both hormone-sensitive and insensitive BCa, we discovered that E2 and TAM perturbed the expression of proteins associated with ER-α signaling pathways.

Given the measurement of ER-α-associated proteins at the single-cell level, we mapped correlation networks that characterize associations between ER-α isoforms and proteins associated with ER-α signaling pathways. For the analysis, we used Spearmans correlation coefficients (ρ) with Dunn and Sidak correction and a p value < 0.05. At a basal level, ER-α46 is strongly associated ($\rho > 0.7$) with pS6 and p38-MAPK, while ER-α66 is weakly associated ($0.4 < \rho < 0.5$) with pS6 and p38-MAPK in MCF-7 cells (Figure 4.12A, Top). However, after treatment with E2 and TAM, we discovered different patterns of the correlation map (Figure 4.12A, Top). After E2 treatment, the ER-α46 subpopulation was strongly associated with the ER-α66 subpopulation (Figure 4.12A). This strong association implies a molecular mechanism in which ER-α46 and ER-α66 form heterodimers in the presence of E2 [19, 45].

In the E2 and TAM groups, ER-α46 was no longer significantly associated with p38-MAPK and pS6. Further, we expanded our analysis of proteins associated with the ER-α signaling pathway by dissecting the MCF-7 cells into subpopulations with respect to ER-α isoforms (Figure 4.12B, C). In the MCF-7 subpopulation expressing ER-α46, E2 treatment did not significantly change p38-MAPK expression (Figure 4.12B). In contrast, TAM treatment significantly decreased p38-MAPK expression in MCF-7 cells, regardless of ER-α presence (Figure 4.12B). Alternatively, ER-α66 increased interconnectivity with p38-MAPK and CD44 in response to E2 and TAM treatment (Figure 4.12A). The subpopulation that ex-

clusively expressed ER-α66 (ER-α66$^+$/ ER-α66$^-$) exhibited an appreciable decrease in CD44 expression after the E2 and TAM treatments (Figure 4.12B). The only subpopulations that responded to E2 and TAM treatment with a change in pS6 expression were ER-α66$^+$/ER-α46$^-$ and ER-α66$^-$/ER-α46$^-$ MCF-7 cells (Figure 4.12B).

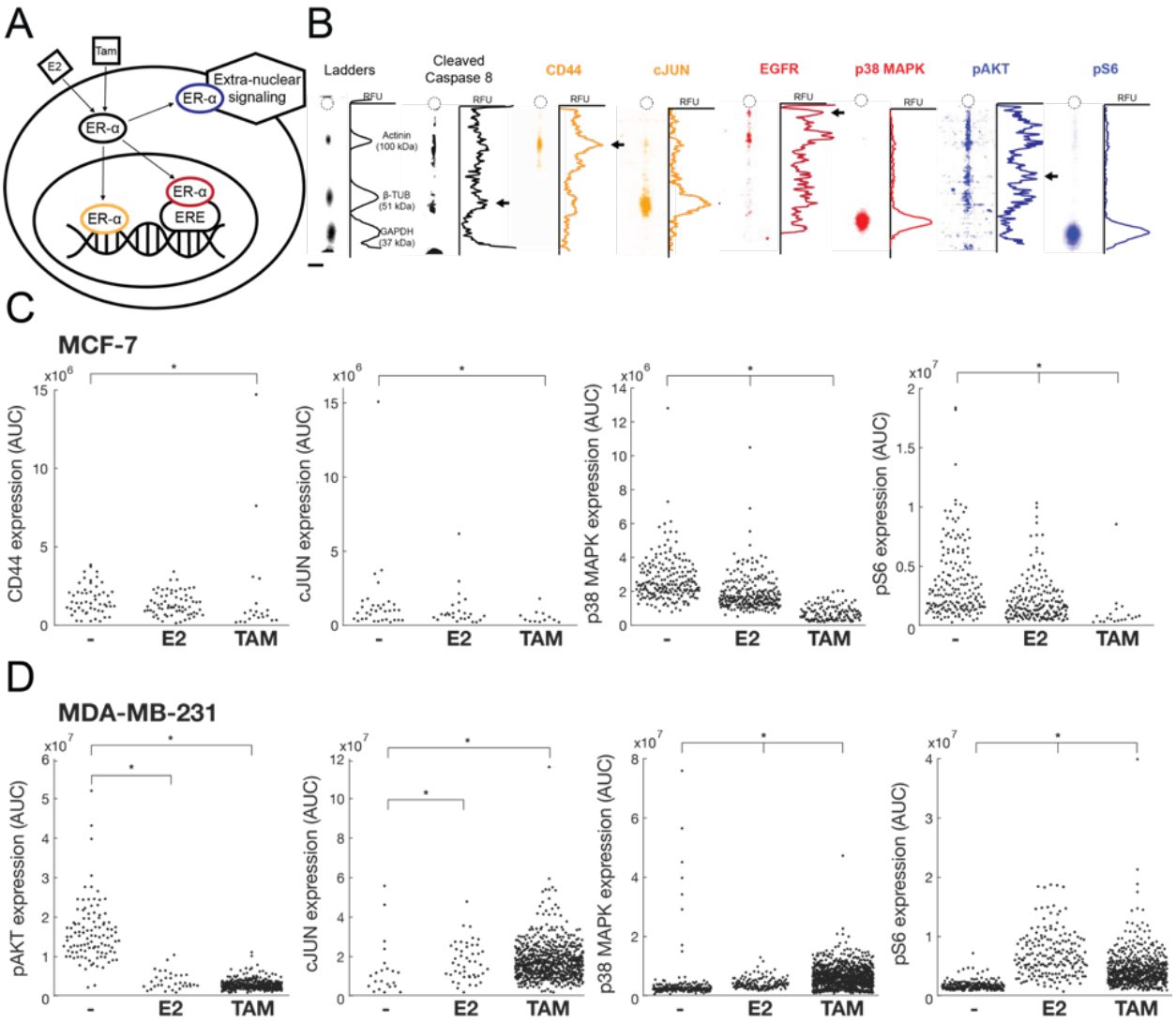

Figure 4.10: E2 and TAM effects on proteins associated with ER-α signaling pathways. (A) Schematic illustrating three different ER-α signaling pathways (ERE-independent, ERE-dependent, and extra-nuclear). (B) A panel of false-colored micrographs of proteins associated with ER-α signaling pathways. E2 and TAM treatment affects single-cell expression levels of proteins related to ER-α signaling pathways in (C) MCF-7 and (D) MDA-MB-231 cells (Kruskal-Wallis test with Dunn and Sidak correction, $p < 0.05$).

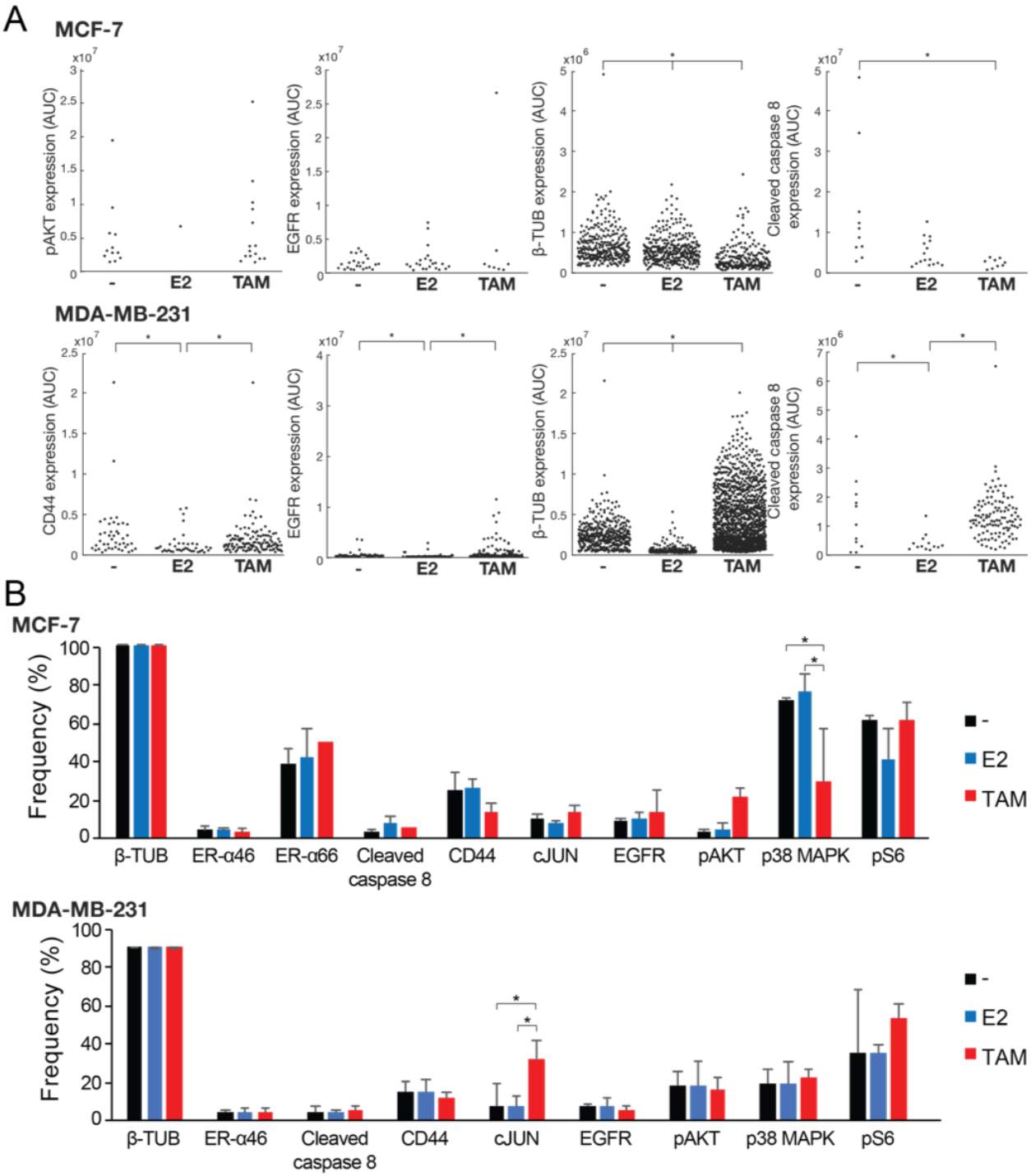

Figure 4.11: E2 and TAM effects in MCF-7 and MDA-MB-231 cells. (A) Scatter plots representing changes in expression levels of proteins related to ER-α signaling pathways in MCF-7 and MDA-MB-231 cells (Kruskal-Wallis test with Dunn and Sidak correction, $p < 0.05$). (B) Bar graphs showing subpopulation frequencies before and after E2 or TAM treatments (Unpaired t test, $p < 0.05$).

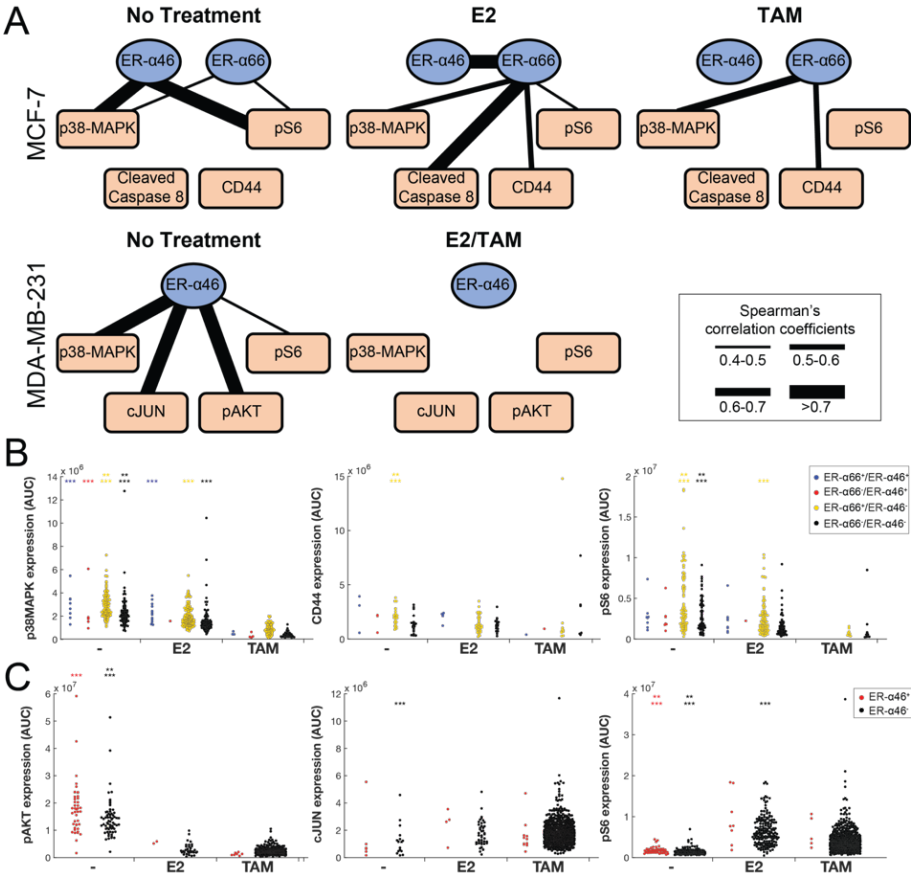

Figure 4.12: Estradiol stimulation and ER-α inhibition by TAM perturbs ER-α signaling pathways in MCF-7 and MDA-MB-231 cells. (A) Interaction mapping of ER-α isoforms with protein targets related to ER-α signaling pathways. Interactions are mapped, with Spearmans correlations indicated by line thickness as shown in the key, for the E2, TAM, and no-treatment conditions. Only interactions with the ER-α isoforms are shown, and all indicated correlations were confirmed with a Dunn and Sidak corrected p-value test ($p < 0.05$). (B) Scatter plots represent p38-MAPK, CD44, and pS6 expression levels in MCF-7 subpopulations with different ER-α isoforms, before and after the E2 and TAM treatments. (C) Scatter plots representing pAKT, cJUN, and pS6 expression levels in MDA-MB-231 subpopulations with and without ER-α46 before and after the E2 and TAM treatments. (**: significant difference from the E2 group, ***: significant difference from the TAM group, Kruskal-Wallis test with Dunn and Sidak correction, $p < 0.05$).

In the MDA-MB-231 cells, ER-α46 was associated with p38-MAPK, cJUN, pAKT, and pS6 at the basal level (Figure 4.12A, Bottom). However, after treatment with either E2 or TAM, associations between ER-α46 and any of the other targeted proteins were lost (Figure 4.12A). This striking loss of interconnectivity with ER-α46 after E2 and TAM perturbations indicates that the ER-α signaling pathways in MDA-MB-231 cells are wired differently from

those in MCF-7 cells. Specifically, the pAKT expression level decreased in the ER-α46$^+$ MDA-MB-231 subpopulation after TAM treatment (Figure 4.12C). In contrast, E2 and TAM treatment increased pS6 expression in the ER-α46$^+$ subpopulation (Figure 4.12C). Regarding cJUN expression, TAM significantly affected only the subpopulation that lacked ER-α46 (Figure 4.12C). The correlation mapping and the assessment of ER-α subpopulations suggest that potential targets of TAM include CD44 and pS6 for ER-α66$^+$/ER-α46$^-$ BCa, p38MAPK for ER-α66$^+$/ER-α46$^+$ BCa, and pAKT for ER-α66$^-$/ER-α46$^+$ BCa.

4.4 Discussion and Conclusion

Accumulating evidence for the importance of ER-α isoforms in hormonal therapy has indicated the need for single-cell technology for measuring isoform heterogeneity and delineating interactions with proteins associated with the ER-α isoforms in BCa. Consequently, we report on an scWestern approach capable of distinguishing between full-length ER-α66 and truncated ER-α46 by coupling electrophoretic separation of proteins to antibody multiplexing for detection. Such a single-cell cytometry method has not been previously available, as immunoassays are insufficiently selective due to the high percentage of amino-acid sequence overlap between ER-α46 and ER-α66.

After exhaustive antibody validation and lysis optimization, the scWestern readily measured, for the first time, the abundance of cells expressing the different ER-α isoforms and variations in ER-α isoform expression, from hundreds of BCa cells. We found four different subpopulations within MCF-7 cells, based on ER- isoform expression: bimodal ER-α (ER-α66$^+$/ ER-α46$^+$), unimodal ER-α(ER-α66$^+$/ ER-α66$^-$, ER-α66$^-$/ ER-α46$^+$), and lacking ER-α (ER-α66$^-$/ER-α46$^-$). In the bimodal ER-α subpopulation, ER-α66 and ER-α46 expression levels were positively correlated, both at the basal level and after E2 treatment. The positive correlation between the ER-α isoforms complements the previous finding that ER-α46, a splice variant of ER-α66, dimerizes with ER-α66 to modulate BCa proliferation [19].Although the subpopulation of MCF-7 cells expressing ER-α46 was small ($<$ 10% of cells), this subpopulation was more dispersed than the subpopulation expressing ER-α66. Thus, the diverse subpopulations and variations of cells expressing ER-α indicate that ER-α transcription activity may widely affect response to E2 and TAM ligands.

Traditionally thought to be non-respondent to TAM treatment, MDA-MB-231 is a classical triple-negative BCa cell line (full length ER-α66$^-$, PR$^-$, HER2$^-$). However, several studies have reported that 5-10% of ER-α66- BCa are sensitive to TAM, presenting the possibility of a role for splice variants in TAM sensitivity [1, 5]. Here, we report that ER-α46 is expressed in MBA-MD-231 cells. In fact, we detected a small subpopulation (2%) of MDA-MB-231 cells that have a higher expression level of ER-α46 than MCF-7 cells. This ER-α46 heterogeneity in the absence of ER-α66 implies that ER-α signaling pathways are regulated differently in MDA-MB-231 cells. By extension, this raises the possibility that ER-αsignaling pathways are regulated differently in triple negative BCa, compared with ER-α$^+$ BCa.

Besides characterization of ER-α isoforms in BCa, we perturbed the ER-α signaling pathways with E2 and TAM treatments and analyzed the effects of these treatments through multiplexing of ER-α isoforms and upstream proteins that interact with ER-α. In agreement with previous studies, the E2 and TAM treatments reduced ER-α66 expression in MCF-7 cells [46]. Further, the scWestern found that TAM lowered ER-α46 expression in the MCF-7 subpopulation that expressed both the ER-α66 and ER-α46 isoforms. The TAM treatment also significantly lowered p38-MAPK expression levels in these subpopulations, suggesting the involvement of an ERE-dependent mechanism in the ER-α signaling pathway. Alternatively, the reduced CD44 and pS6 expression levels in the ER-α66^{+}/ ER-α46^{-} subpopulation after the TAM and E2 treatments suggest that both non-ERE and extra-nuclear mechanisms also play significant roles in BCa hormonal regulation. Interestingly, a decrease in pAKT and an increase in pS6 in the ER-α46^{+} MDA-MB-231 cells after TAM treatment implies that ER-α46 is involved in extra-nuclear ER-αsignaling mechanisms.

Taken together, the scWestern unveiled the presence of ER-α isoform heterogeneity in both hormone-sensitive and hormone-insensitive BCa. Further investigation of p38 MAPK, CD44, pAKT, and pS6 needs to be performed to clarify the exact mechanisms underlying the genomic and non-genomic ER-α signaling pathways. Such research could also uncover potential biomarkers for hormonal therapy response. Finally, we will measure ER-α isoforms in patient-derived biospecimens before and after hormonal therapy. Given the sweeping importance of truncated oncoprotein isoforms in the development of drug resistance and as potential therapeutic targets, high-selectivity cytometry assays – such as that described here – are a critical missing component for pinpointing cancer with personalized therapies to benefit patients.

Bibliography

1. Manna, S. & Holz, M. K. Tamoxifen Action in ER-Negative Breast Cancer. *Signal Transduction Insights.* ISSN: 1178-6434. doi:10.4137/STI.S29901 (2016).
2. Hoefnagel, L. D. C. *et al.* Discordance in ERalpha, PR and HER2 receptor status across different distant breast cancer metastases within the same patient. *Annals of Oncology* **24,** 3017–3023. ISSN: 1569-8041 (2013).
3. Onitilo, A. A. *et al.* Breast cancer subtypes based on ER/PR and Her2 expression: comparison of clinicopathologic features and survival. *Clinical medicine & research* **7,** 4–13. ISSN: 1554-6179 (2009).
4. García-Becerra, R. *et al. Mechanisms of resistance to endocrine therapy in breast cancer: Focus on signaling pathways, miRNAs and genetically based resistance* 2013. doi:10.3390/ijms14010108.
5. Johnston, S. R., Dowsett, M & Smith, I. E. Towards a molecular basis for tamoxifen resistance in breast cancer. *Annals of oncology : official journal of the European Society for Medical Oncology* **3,** 503–11. ISSN: 0923-7534 (1992).
6. Shou, J. *et al.* Mechanisms of tamoxifen resistance: Increased estrogen receptor-HER2/neu cross-talk in ER/HER2-positive breast cancer. *Journal of the National Cancer Institute.* ISSN: 00278874. doi:10.1093/jnci/djh166 (2004).
7. Hall, J. M., Couse, J. F. & Korach, K. S. *The Multifaceted Mechanisms of Estradiol and Estrogen Receptor Signaling* 2001. doi:10.1074/jbc.R100029200.
8. Snozek, C. L., O'Kane, D. J. & Algeciras-Schimnich, A. *Pharmacogenetics of solid tumors: Directed therapy in breast, lung, and colorectal cancer - A paper from the 2008 William Beaumont Hospital symposium on molecular pathology* 2009. doi:10.2353/jmoldx.2009.090003.
9. Mazhar, D. & Waxman, J. *Early chemotherapy in prostate cancer* 2008. doi:10.1038/ncpuro1204.
10. Yoshida, T *et al.* Distinct mechanisms of loss of estrogen receptor alpha gene expression in human breast cancer: methylation of the gene and alteration of trans-acting factors. *Carcinogenesis.* ISSN: 0143-3334 (2000).
11. Navin, N. *et al.* Tumour evolution inferred by single-cell sequencing. *Nature.* ISSN: 00280836. doi:10.1038/nature09807 (2011).

12. Yates, L. R. *et al.* Genomic Evolution of Breast Cancer Metastasis and Relapse. *Cancer Cell.* ISSN: 18783686. doi:10.1016/j.ccell.2017.07.005 (2017).

13. Youn, A. & Simon, R. Identifying cancer driver genes in tumor genome sequencing studies. *Bioinformatics* **27,** 175–181. ISSN: 1460-2059 (2011).

14. Fan, W., Chang, J. & Fu, P. Endocrine therapy resistance in breast cancer: current status, possible mechanisms and overcoming strategies. *Future medicinal chemistry* **7,** 1511–9. ISSN: 1756-8927 (2015).

15. Osborne, C. K. & Schiff, R. Mechanisms of Endocrine Resistance in Breast Cancer. *Annual Review of Medicine* **62,** 233–247. ISSN: 0066-4219 (2011).

16. Wang, Z. Y. & Yin, L. *Estrogen receptor alpha-36 (ER-α36): A new player in human breast cancer* 2015. doi:10.1016/j.mce.2015.04.017.

17. Su, X. *et al. Er-α36: A novel biomarker and potential therapeutic target in breast cancer* 2014. doi:10.2147/OTT.S65345.

18. Omarjee, S *et al.* The molecular mechanisms underlying the ERα-36-mediated signaling in breast cancer. *Oncogene* **36,** 2503–2514. ISSN: 0950-9232 (2017).

19. Klinge, C. M. *et al.* Estrogen receptor alpha 46 is reduced in tamoxifen resistant breast cancer cells and re-expression inhibits cell proliferation and estrogen receptor alpha 66-regulated target gene transcription. *Molecular and Cellular Endocrinology.* ISSN: 03037207. doi:10.1016/j.mce.2010.03.013 (2010).

20. Figtree, G. A. *et al.* Truncated Estrogen Receptor α 46-kDa Isoform in Human Endothelial Cells. *Circulation* **107,** 120 –126 (2003).

21. Li, L., Haynes, M. P. & Bender, J. R. Plasma membrane localization and function of the estrogen receptor alpha variant (ER46) in human endothelial cells. *Proceedings of the National Academy of Sciences of the United States of America* **100,** 4807–12. ISSN: 0027-8424 (2003).

22. Flouriot, G. Identification of a new isoform of the human estrogen receptor-alpha (hER-alpha) that is encoded by distinct transcripts and that is able to repress hER-alpha activation function 1. *The EMBO Journal.* ISSN: 14602075. doi:10.1093/emboj/19.17.4688. arXiv: arXiv:1011.1669v3 (2000).

23. Kang, C. C. *et al.* Single cell-resolution western blotting. *Nature Protocols.* ISSN: 17502799. doi:10.1038/nprot.2016.089 (2016).

24. Hughes, A. J. *et al.* Single-cell western blotting. *Nature Methods* **11,** 749–755. ISSN: 1548-7091 (2014).

25. Sinkala, E. *et al.* Profiling protein expression in circulating tumour cells using microfluidic western blotting. *Nature Communications* **8,** 14622. ISSN: 2041-1723 (2017).

26. Peach, M. *et al.* in *Western Blotting: Methods and Protocols* (2015). ISBN: 9781493926947. doi:10.1007/978-1-4939-2694-7_8.

27. Nalvarte, I., Schwend, T. & Gustafsson, J.-A. Proteomics analysis of the estrogen receptor alpha receptosome. *Molecular & cellular proteomics : MCP.* ISSN: 1535-9484. doi:10.1074/mcp.M900457-MCP200 (2010).

28. Ferguson, K. A. Starch-gel electrophoresis–application to the classification of pituitary proteins and polypeptiedes. *Metabolism: clinical and experimental* **13,** 985–1002. ISSN: 0026-0495 (1964).

29. Herr, A. E. & Singh, A. K. Photopolymerized cross-linked polycrylamide gels for on-chip protein sizing. *Analytical Chemistry* **76,** 4727–4733. ISSN: 00032700 (2004).

30. Wang, Z. *et al.* A variant of estrogen receptor-{alpha}, hER-{alpha}36: transduction of estrogen- and antiestrogen-dependent membrane-initiated mitogenic signaling. *Proceedings of the National Academy of Sciences of the United States of America* **103,** 9063–8. ISSN: 0027-8424 (2006).

31. Yeh, W. L. *et al.* Fulvestrant-induced cell death and proteasomal degradation of estrogen receptor alpha protein in MCF-7 cells require the CSK c-Src tyrosine kinase. *PLoS One* **8.** doi:10.1371/journal.pone.0060889 (2013).

32. Jordan, V. Effects of tamoxifen in relation to breast cancer. *British medical journal,* 1534–1535. ISSN: 0007-1447 (1977).

33. Tzukerman, M. T. *et al.* Human estrogen receptor transactivational capacity is determined by both cellular and promoter context and mediated by two functionally distinct intramolecular regions. *Molecular endocrinology (Baltimore, Md.)* **8,** 21–30. ISSN: 0888-8809 (1994).

34. Fan, M., Nakshatri, H. & Nephew, K. P. Inhibiting proteasomal proteolysis sustains estrogen receptor-alpha activation. *Molecular endocrinology (Baltimore, Md.)* **18,** 2603–15. ISSN: 0888-8809 (2004).

35. Powers, G. L. *et al.* Proteasome inhibition represses ERalpha gene expression in ER+ cells: a new link between proteasome activity and estrogen signaling in breast cancer. *Oncogene* **29,** 1509–18. ISSN: 1476-5594 (2010).

36. Rondon-Lagos, M *et al.* Effect of low doses of estradiol and tamoxifen on breast cancer cell karyotypes. *Endocr Relat Cancer* **23,** 635–650. ISSN: 14796821 (2016).

37. Liu, C.-Y. *et al.* Tamoxifen induces apoptosis through cancerous inhibitor of protein phosphatase 2A–dependent phospho-Akt inactivation in estrogen receptor–negative human breast cancer cells. *Breast Cancer Research* **16,** 431. ISSN: 1465-542X (2014).

38. Roforth, M. M. *et al.* Dissection of Estrogen Receptor Alpha Signaling Pathways in Osteoblasts Using RNA-Sequencing. *PLoS ONE* **9** (ed Migliaccio, A.) e95987. ISSN: 1932-6203 (2014).

39. Marino, M, Galluzzo, P & Ascenzi, P. Estrogen signaling multiple pathways to impact gene transcription. *Curr Genomics* **7,** 497–508. ISSN: 13892029 (2006).

40. Qi, X. *et al.* p38 Mitogen-activated Protein Kinase (MAPK) Confers Breast Cancer Hormone Sensitivity by Switching Estrogen Receptor (ER) Signaling from Classical to Nonclassical Pathway via Stimulating ER Phosphorylation and c-Jun Transcription * S. doi:10.1074/jbc.M112.349357 (2012).

41. Inoue, K. & Fry, E. A. Aberrant Splicing of Estrogen Receptor, HER2, and CD44 Genes in Breast Cancer. *Genetics & epiGenetics* **7,** 19–32 (2015).

42. Madeo, A *et al.* c-Jun activation is required for 4-hydroxytamoxifen-induced cell death in breast cancer cells. *Oncogene* **29,** 978–991 (2009).

43. Yanai, A. *et al.* Activation of mTOR/S6K but not MAPK pathways might be associated with high Ki-67, ER+, and HER2- breast cancer. *Clinical Breast Cancer.* ISSN: 19380666. doi:10.1016/j.clbc.2014.12.002 (2015).

44. Tang, D., Lahti, J. M. & Kidd, V. J. Caspase-8 activation and Bid cleavage contribute to MCF7 cellular execution in a caspase-3-dependent manner during staurosporine-mediated apoptosis. *Journal of Biological Chemistry* **275,** 9303–9307. ISSN: 00219258 (2000).

45. Denger, S *et al.* ERalpha gene expression in human primary osteoblasts: evidence for the expression of two receptor proteins. *Molecular endocrinology (Baltimore, Md.)* **15,** 2064–2077. ISSN: 0888-8809 (2001).

46. Penot, G. *et al.* The Human Estrogen Receptor-α Isoform hERα46 Antagonizes the Proliferative Influence of hERα66 in MCF7 Breast Cancer Cells. *Endocrinology* **146,** 5474–5484. ISSN: 0013-7227 (2005).

Chapter 5

Integrating sample preparation and size exclusion electrophoresis to measure binding affinity

5.1 Introduction

Receptor-ligand interactions dictate cellular processes involving metabolism [1, 2], growth [3, 4], differentiation [5, 6], and migration [7, 8]. Quantitatively analyzing the receptor-ligand kinetics would be essential in delineating biological processes as well as engineering drugs to treat cancer and other chronic diseases. For instance, G-protein-coupled receptor (GPCR) is an exemplary protein target that highlights the importance of quantitating binding kinetics. To engineer ligands for the GPCR in pharmacology, equilibrium dissociation rate (K_D) based on three different conformations of the GPCR complex needs to be carefully considered [2]. In addition to the equilibrium kinetics of the GPCR and the ligand, binding and dissociating rates at a non-equilibrium state are critical parameters as the activation efficiency of the GPCR signal transduction relies on the life span of the GPCR-ligand complex [1, 2].

Standard analytical assays to measure the ligand-receptor interactions involve surface modifications or electrophoresis. In the surface-based methods, surface plasmon resonance [9, 10] and enzyme linked immunosorbent assays (ELISA) [11, 12] are conventionally used to assess KD of a ligand-receptor complex. Despite the accurate KD measurements from these assays, the transport limited regime in the surface reaction considerably delays the equilibrium time and leads to high sample consumption [9, 11, 13]. More importantly, these surface-based assays do not directly measure association and dissociation rates that are crucial in analyzing the cellular signaling transduction. Alternative method to detect molecular interactions uses separation by physicochemical properties of proteins (e.g. size, charge) in capillary or microfluidic platforms [14–19]. These solution-based and homogeneous assays enable high throughput kinetic measurement in a microfluidic array format that reduces sample consumption [18, 19]. Yet, these surface-based and separation-based assays require

to prepare samples with serial dilution points of ligand with ¿2 orders of magnitude in the concentration range [11, 16, 18, 19].

The sample preparation can be further realized and improved by exploiting physics at the microscale. In a typical microchannel with ¡ 1 mm in one dimension, viscous forces dominate over inertial forces that molecular diffusion governs the mass transport in a predictable manner. This microscale diffusion is leveraged in T-sensor and H-filter microfluidic devices to generate serial dilutions and gradient generations of molecules for applications in analytical chemistry [20–22]. In this chapter, by generating a spatial concentration gradient of receptor and loading an uniform concentration of ligand, we minimize possible handling errors and reduce sample consumption and preparation time required to make serial dilutions. With careful design and calculations, we design, characterize, and develop a microfluidic platform that improves sample preparation and integrate with a backend electrophoretic assay to measure the receptor-ligand binding kinetics in a single device run.

5.2 Materials and Methods

Reagents and Samples

Isopropanol and 10x tris-glycine buffer for washing and electrophoretic buffer were purchased from Sigma Aldrich. Alexa Fluor 488 labelled ovalbumin anti-mouse antibody (sc-65984) was purchased from Santa Cruz Biotechnology. Alexa Fluor 555 labelled ovalbumin (OVA) and bovine serum albumin (BSA) were purchased from Thermofisher Scientific. For polyacrylamide polymerization, 30% (w/v) (29:1) acrylamide/bisacrlyamide (Sigma Aldrich) and VA-086 photo initiator (Wako Chemicals) N-[3-[(3-Benzoylphenyl)-formamido]propyl] methacrylamide (BPMAC, PharmAgra Laboratories) were used. GelBond polyester film was purchased from Lonza. The mylar photomask was printed from CAD/Art Services.

Microfluidic Affinity Device Fabrication

The 3M adhesive layer with the channel design and the polyester lid patterned with inlet and outlets were cut with a laser cutter (H-Series Desktop CO_2 Laser, Full Spectrum Laser) and cleaned by vacuuming and applying scotch tape along all features on the layer. After carefully aligning the polyester layers with the adhesive layer, heat and pressure were applied using a laminator (Omega Laminator A4).

Polyacrylamide Gel Fabrication in the Mircrofluidic Affinity Device

The microfluidic device was pre-treated with 6% BPMAC in isopropanol for 30 s and cleaned with water twice. A 10% acrylamide solution with 1% (w/v) VA-086 photoinitiator was

degassed for 5 min and filled in the microfluidic device via ports. The photomask (CAD/Art Services) was aligned below the microfluidic device and exposed to UV (OAI model 30 collimated UV light source) for 60 s at 20 mW/cm^2.

Imaging

Inverted epifluorescence microscope (Olympus IX51) with a motorized stage (Applied Scientific Instrumentation, MS-2000) and an X-cite mercury light source (Lumen Dynamic) was used for imaging inside the microfluidic device. With 200 msec exposure time, 2x-objective (N.A. = 0.08, Olympus) brightfield and fluorescence images were taken with a Peltier cooled charge-coupled device (CCD) camera (CoolSNAP HQ2, Roper Scientific). Standard FITC/GFP (Chroma 41017) and Cy3, Texas Red (Omega XF1112) filter cubes were used to detect fluorescence-tagged proteins. Image analysis was performed with ImageJ software.

Finite Element Simulation

We simulated the protein loading in a 2D environment using COMSOL Multiphysics version 5.0 (COMSOL Inc.). The device geometry was drawn in Adobe Illustrator and exported to COMSOL. Laminar flow module was used with no-slip wall boundary conditions. For a migration of proteins due to pressure-driven flow and electric field, the 'Transport of Diluted Species' physics module was applied. We assumed that protein concentrations do not affect physical properties of fluids or gels. For an electrical field, a voltage of 600V is applied across the channel length. The 600 voltage potential difference gives an electrical field of 300 V/cm.

5.3 Results and Discussion

Integrating size exclusion electrophoresis with protein sample preparation in adhesive microfluidics

We sought to increase throughput with sample handling and collection by developing an adhesive microfluidics system that integrates polyacrylamide gel filtration with sample preparation. The microfluidic affinity assay consists of the sample preparation module with capillary loading of ligand and receptor proteins (Figure 5.1). By modulating the capillary driven flow in the H-filter channel design, a spatial gradient with receptor concentration was generated within minutes as a surrogate for a standard sample preparation for K_D measurement, which involves serial dilutions of the receptor (Figure 5.1B). Following the sample preparation module, the gel filtration module measures ligand-receptor interaction by using size exclusion to immobilize ligand-bounded receptors (i.e. antibody) at a solution-to-gel interface (Figure 5.1B).

The adhesive microfluidic is a cost-effective (< \$5 per device) technique that enables rapid fabrication and iterations with various channel designs. The microfluidic device is comprised of an adhesive sheet pressured and laminated between two Gelbond® flexible polyester films (Figure 5.1A). After laser cutting with a specific channel design, the adhesive sheet with 60-µm thickness served as a channel wall and enabled fluid transport between the hydrophobic surfaces of the two polyester films (Figure 5.1A). With multiple inlet and outlet ports, a precursor solution of polyacrylamide gel was filled inside the channel and left out at room temperature for 5 min to equilibrate pressure inside the channel (Figure 5.1B). Using a photomask with a rectangular hole, a polyacrylamide gel was photo-polymerized below the size exclusion zone by exposing under UV for 30 s (Figure 5.1B).

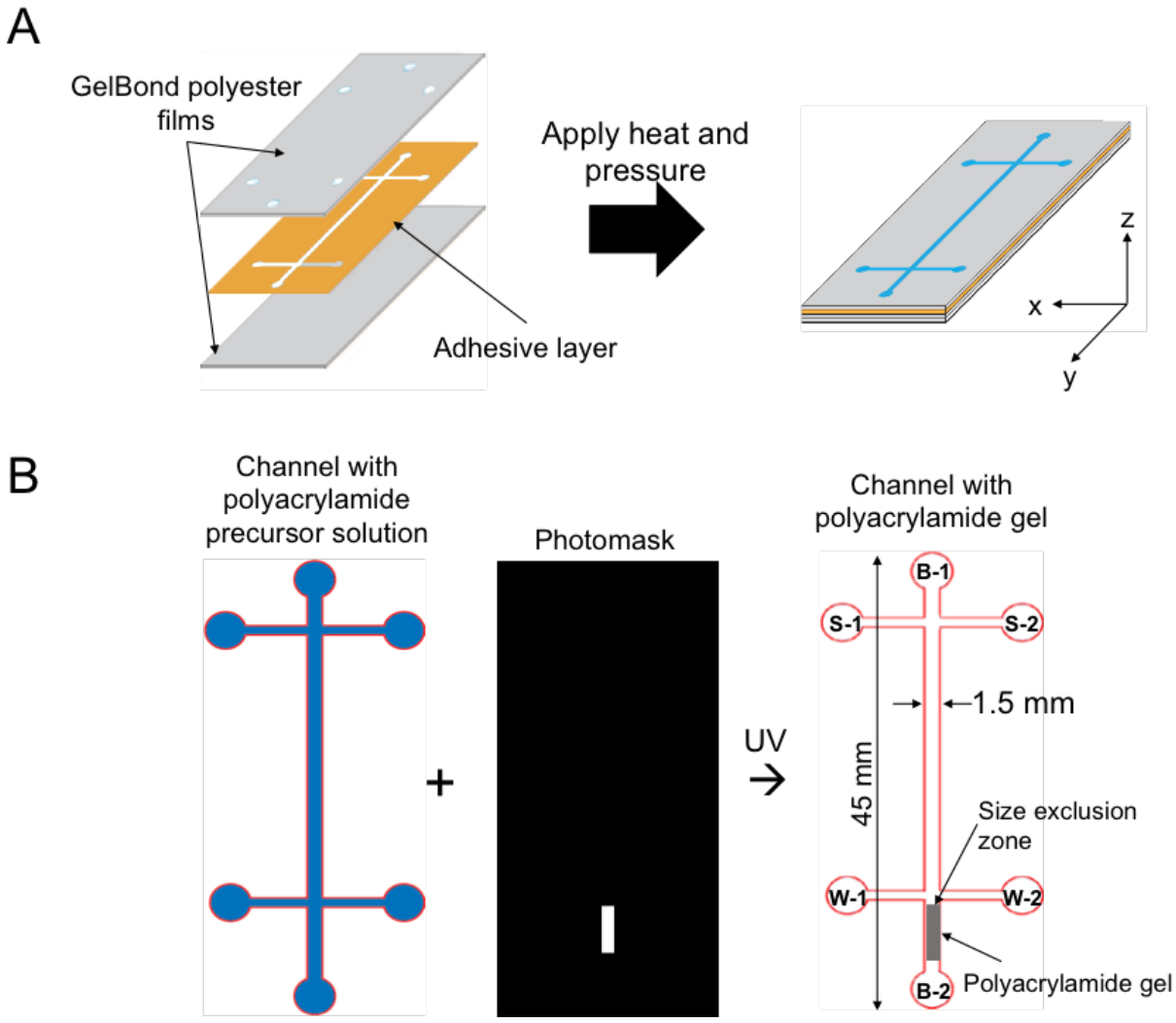

Figure 5.1: Design and fabrication of the microfluidic affinity assay. (A) The microfluidic device is fabricated by sandwiching an adhesive layer with two polyester films. A laser cutter is used to exclude an adhesive layer with a channel design and pattern the top polyester layer with inlet and outlet ports. Heat and pressure were applied to completely seal between the polyester films. (B) The microchannel was filled with polyacrylamide precursor solution. Using a darkfield photomask, a polyacrylamide gel was polymerized at a desired location above the B-2 outlet port.

Characterization of the microfluidic affinity assay for sample preparation

First, using a finite element simulation (COMSOL®), we sought to investigate whether spatial gradient and uniform distribution of protein concentration could be generated by a capillary-driven flow. For following simulation and experiments, we used ovalbumin (OVA) IgG antibody as a receptor and OVA as a ligand. With defined channel width (1.5 mm) and depth (60 μm) of the microfluidic affinity assay, Reynolds dimensionless number indicates that laminar flow is present in our device (Equation 5.1):

$$Re = \frac{vL\rho}{\mu} = \frac{(0.0001\frac{m}{s})(0.0015m)(1000\frac{kg}{m^3})}{0.01\frac{kg}{m \bullet s}} = 0.02 \ll 1 \tag{5.1}$$

Re = Reynolds number, v = the average velocity of the flow (simulated at pressure of 0.1 Pa in COMSOL), L = diameter of channel, μ = viscosity of water, ρ = water density.

Under this laminar flow, injection of the antibody solution (1 mol/m^3, 1 mM) at the S-1 port and water at the S-2 port with equal volumes generated a spatial gradient concentration of antibody across the width of the channel (Figure 5.2). The slope of the antibody concentration across the channel width varies according to the channel length: the slope is large yet non-linear (0 – 1 mol/m^3) near the inlet area (S ports), while the slope is low yet linear near (0.1 – 0.4 mol/m^3) near the outlet area (W ports, Figure 5.2).

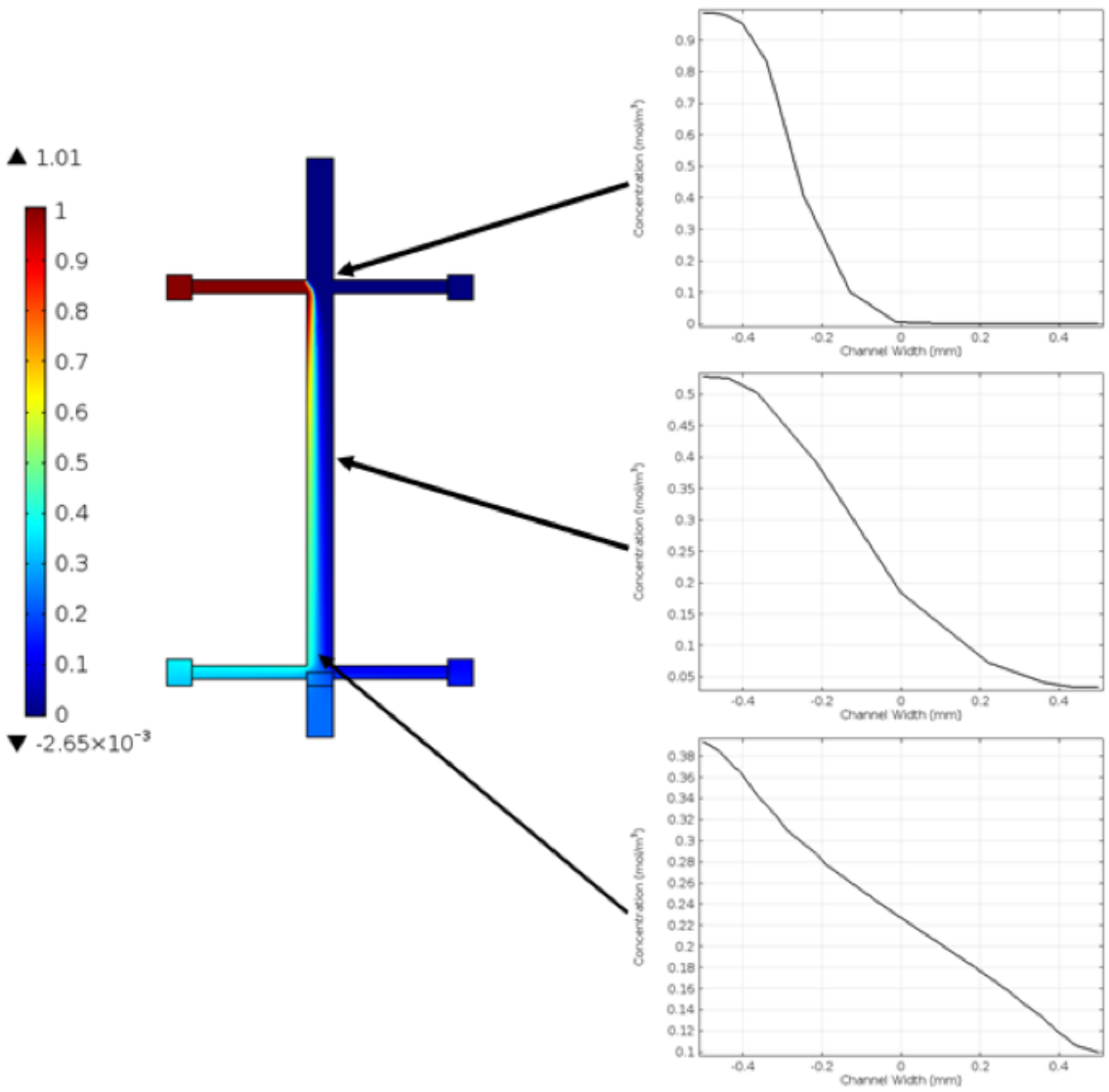

Figure 5.2: Generating OVA antibody concentration gradient across the channel width with a H-filter microchannel design.

Next, we further investigated whether the spatial gradient of antibody concentration was maintained when an electric field was applied to migrate and immobilize the antibody at the size exclusion zone (10% polyacrylamide gel). As expected, the spatial gradient of the antibody concentration across the channel width was remained at the exclusion zone. Additionally, we observed that the antibody stacking at the exclusion zone as the electric field duration increases: the antibody concentration was more than 3-fold greater at the 50 s than the 5 s (Figure **??**).

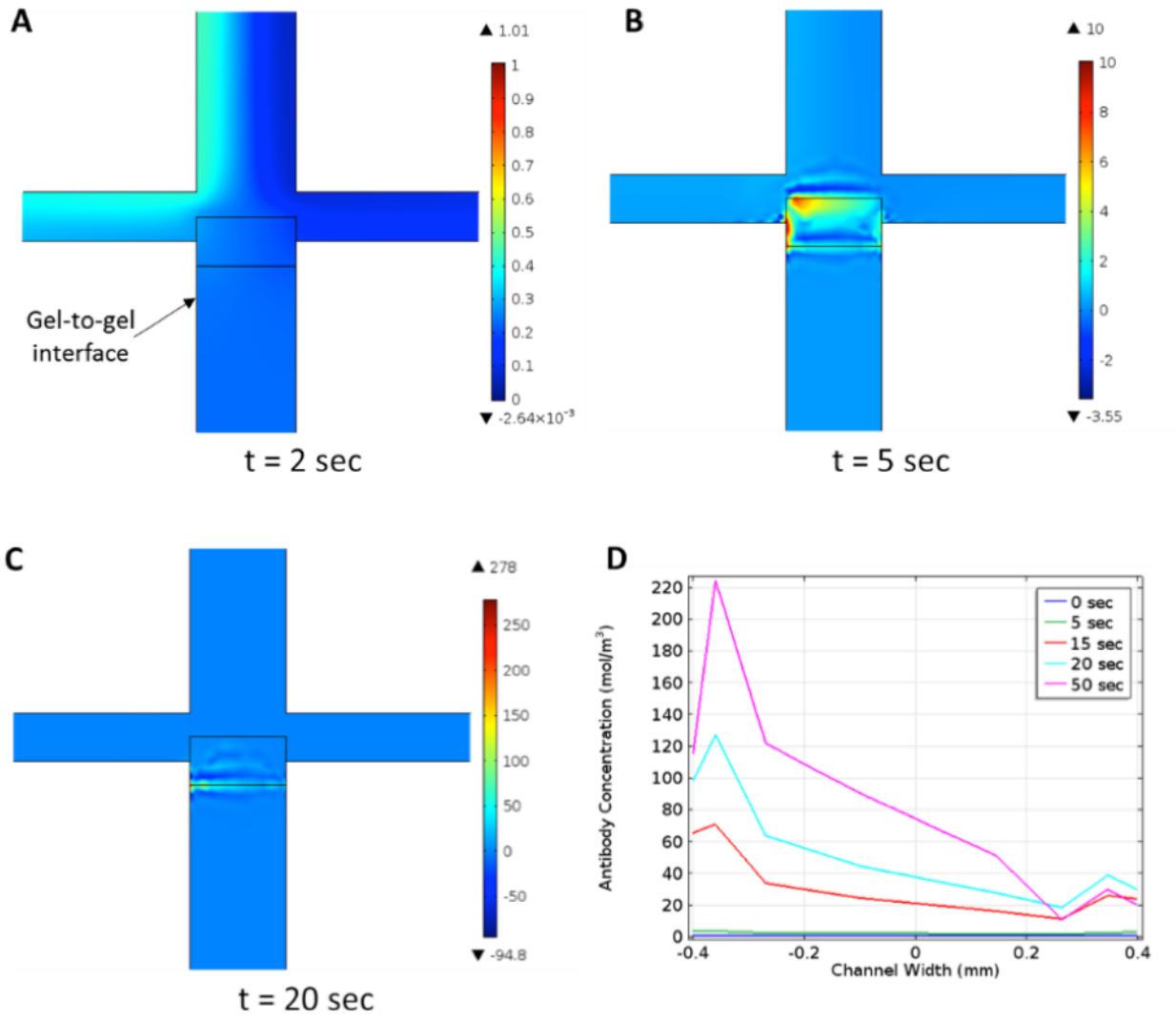

Figure 5.3: Immobilization of OVA antibody at the size exclusion zone between the solution and the polyacrylamide gel during an electric field at (A) 2 s, (B) 5 s, (C) 20 s. (D) A concentration gradient of the antibody at the exclusion zone across the channel width.

In order to measure ligand-receptor affinity in the microfluidic device, we further examined whether a uniform concentration of ligand across the channel width could be achieved at the size exclusion zone. After loading OVA at the S-1 and S-2 ports with equal volumes, the branch channel connecting the S-1 and S-2 ports was filled with OVA (Figure 5.1B). With an applied electric field at 300 V/cm across the B-1 and B-2 ports, an uniform OVA concentration across the width was electrophoresed through the exclusion zone in 30 s (Figure 5.4 A, B). The electric field would be turned off when the OVA reaches the exclusion zone so that OVA binds with the antibody in an equilibrium state. At the exclusion zone, we

found a uniform OVA concentration across the channel width varying less than 0.05 mol/m^3 (Figure 5.4 C). After binding, the electrical field would turn on again to wash away any non-bounded OVA and measure dissociation constant rate.

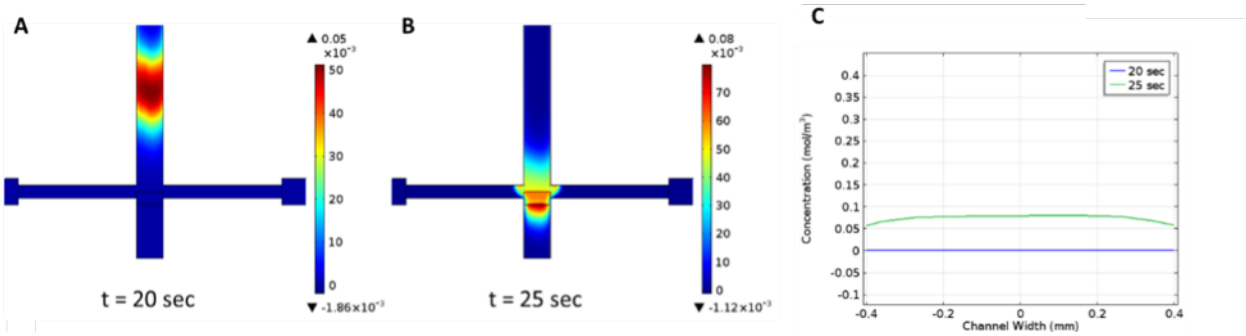

Figure 5.4: Loading spatially uniform concentration of OVA in the microfluidic affinity assay. Electromigration of OVA by applying electric field (300 V/cm) at (A) 20 s and (B) 25 s. (C) Uniform concentration of PSA across the channel width was achieved at the size exclusion zone.

After studying in the finite element simulations, we performed the sample preparation module experimentally to compare with the simulation results. The microfluidic affinity device was assembled with the 10%T polyacrylamide gel polymerized above the B-2 port. Large receptors (e.g. antibody IgG; 150 kDa) were immobilized at the size exclusion zone, while small ligands (OVA; 42.7 kDa) sieved through the zone (Figure 5.5A). Instead of using molecular weight cut-off (MWCO) or photoactive gel techniques [23, 24], an immobilization technique by manipulating a gel density and an antibody molecular size is simple and requires no further chemical modifications. With an electrical field, the receptor with the spatial concentration gradient electromigrated and immobilized at the size exclusion zone (Figure 5.5B, step 1). Then, a ligand with a spatially uniform concentration was added at W ports to form a uniform concentration gradient across the 1.5 mm channel width (Figure 5.5B, step 2). With the same electric field (300 V/cm), the ligand bound with immobilized receptor at the zone when the ligand with the spatially uniform concentration was electromigrated through the zone. By measuring fluorescence from the ligand bounded at the zone, K_D would be estimated in a single device run (Figure 5.5B, step 3).

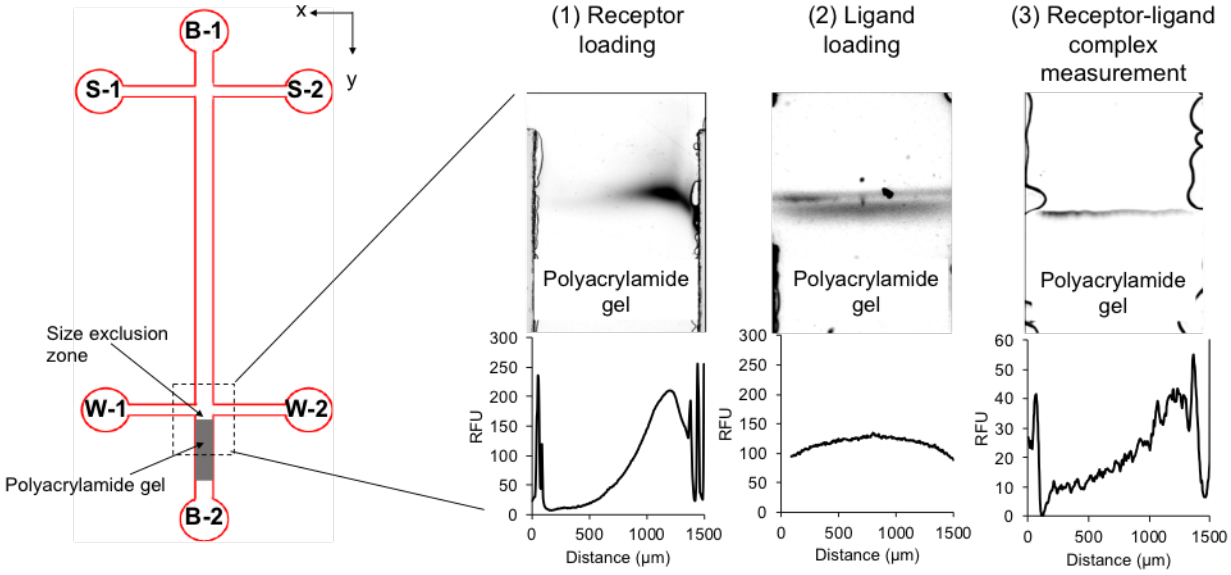

Figure 5.5: Microfluidic affinity device couples spatial gradient generation of protein concentration and electrophoretic size exclusion. In the sample preparation, the H-filter design with S and W ports enables to generate (1) gradient of receptor concentration and (2) uniform ligand concentration across the microchannel width. Following the sample preparation, the receptor gets immobilized at the size exclusion zone, formed between the solution and the polyacrylamide gel interfaces. The electromigrated ligand dwelled at the size exclusion zone for binding. The ligand fraction, bounded with the receptor remained at the zone, was measured after washing.

We further investigated performance of the sample preparation at the size exclusion zone by measuring fluorescence from fluorescence-labelled proteins. We measured the fluorescence intensity of OVA antibody at the exclusion zone as the antibody was electrophoresed to the zone (Figure 5.5, 5.6). Similar to the simulation data, we observed the OVA antibody stacking at the exclusion zone (Figure 5.5, 6). The antibody was enriched at the exclusion zone by a preconcentration factor of 2 within 5 min of electrophoresis (Figure 5.6). After the antibody stacking, the electric field was turned off to examine the antibody diffusing out of the exclusion zone. We observed the antibody remained immobilized at the zone and the spatial gradient of the antibody concentration retained at the zone for ¿ 80 min (Figure 5.7).

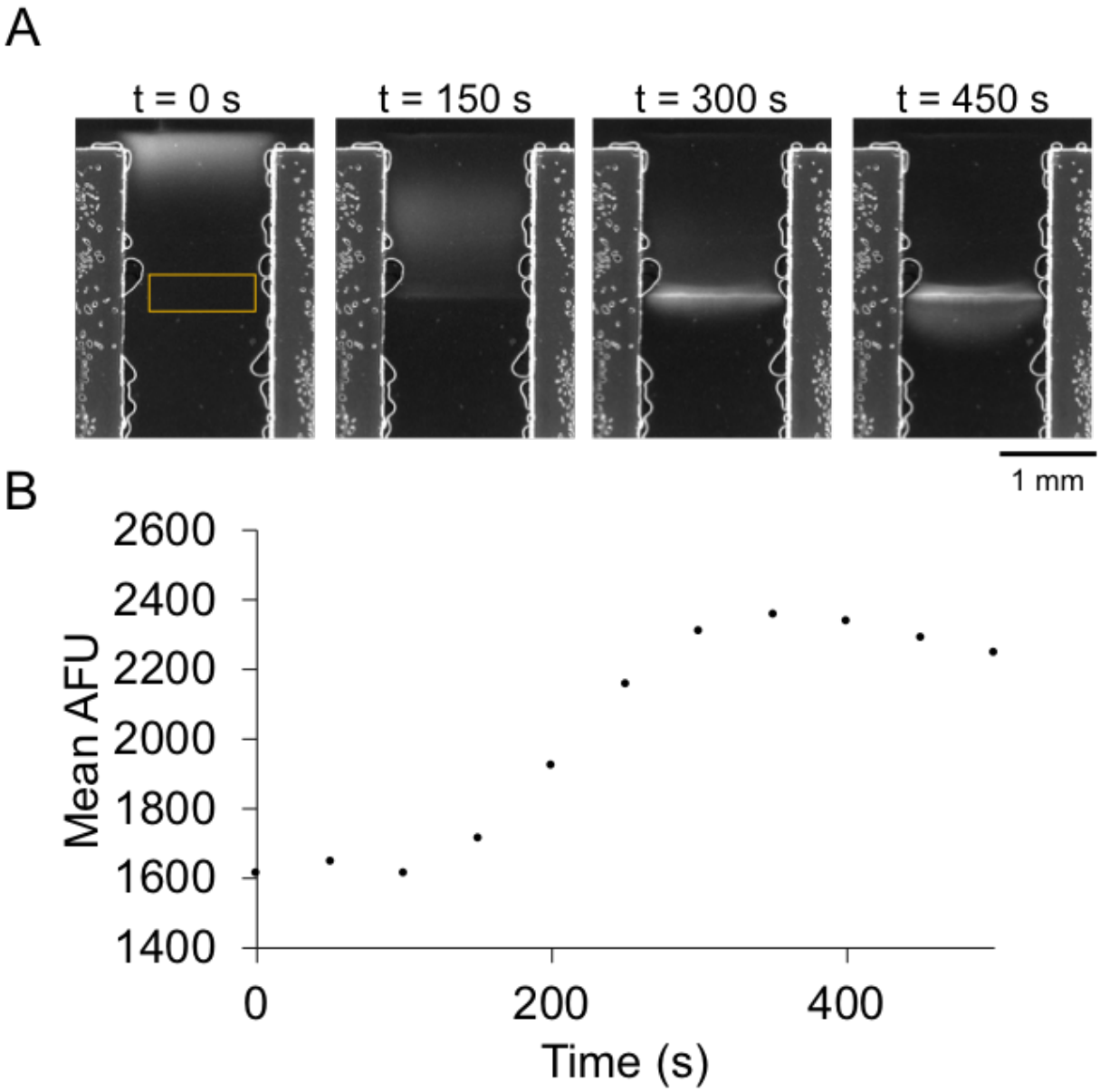

Figure 5.6: Immobilizing the receptor at the size exclusion zone. (A) Micrographs of the receptor electromigrating to the zone and immobilizing at the polyacrylamide gel front. 300 V/cm was applied. (B) Mean fluorescence from receptor measured at the size exclusion zone over the electrophoresis time.

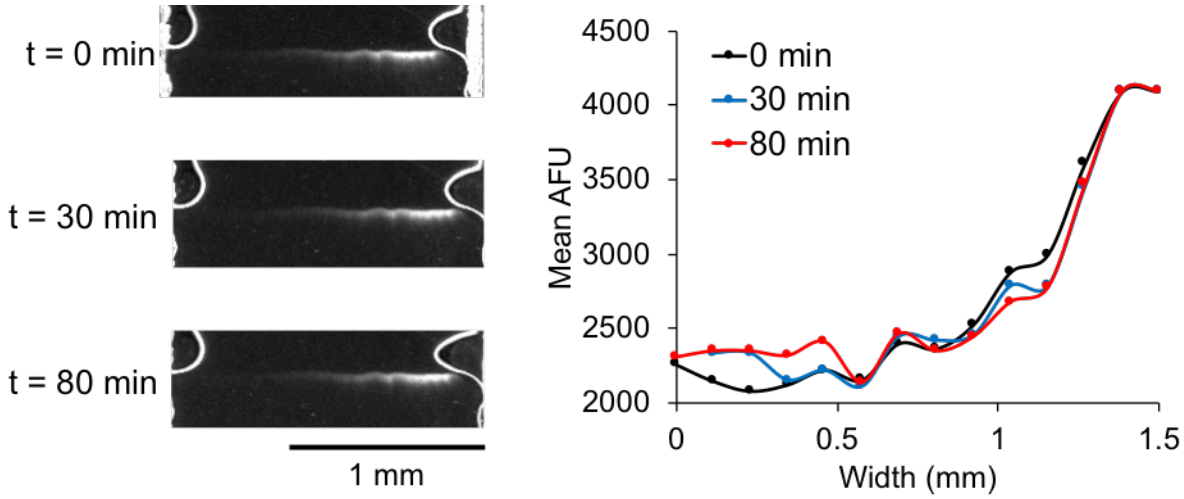

Figure 5.7: Receptor immobilizes at the size exclusion zone, and the receptor concentration gradient remains unchanged over electrophoretic washing.

Having established the spatial gradient of the antibody concentration, we sought to examine the ligand-antibody binding at the exclusion zone by taking average fluorescence across the channel width. Used as a positive control, OVA remained bounded with the OVA antibody at the zone (Figure 5.8). The OVA intensity profile matched with that of OVA antibody; for both intensity profiles, the maximum fluorescence was measured at 75 µm with OVA and OVA antibody peak amplitudes 2-fold greater than the background signal. On the other hand, as expected, BSA did not bind with the OVA antibody and electrophorese through the zone (Figure 5.8).

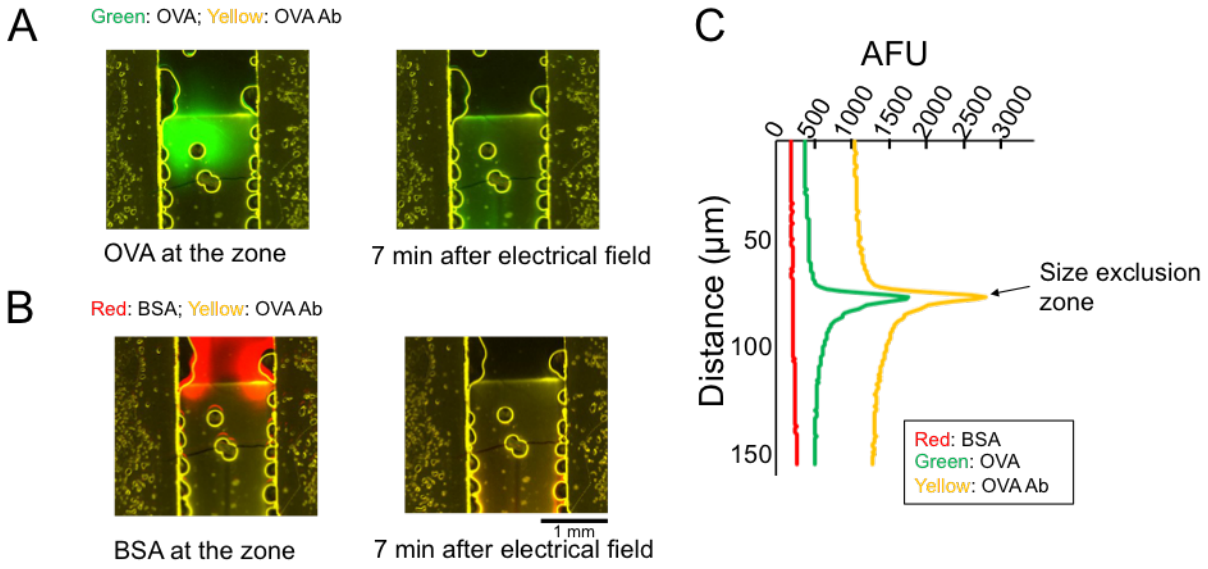

Figure 5.8: Binding of OVA and OVA antibody at the size exclusion zone. Fraction of (A) OVA remains at the size exclusion zone with the OVA antibody after washing at 300 V/cm, while (B) BSA does not bind and remain at the size exclusion zone.

Dissociation constant measurement in a single run with the microfluidic affinity device

Following characterization of the sample preparation and the polyacrylamide gel filtration modules, the microfluidic affinity device was run to measure K_D of OVA and OVA antibody. In order to measure the K_D, we developed calibration curves for OVA and OVA antibody to extract concentration values based on fluorescence measurements (Figure 5.9). Fluorescence intensity and protein concentration followed a linear relationship in nanomolar concentration ranges. For both OVA and OVA ab calibration curves, linear regression was fit with $R^2 > 0.9$ (Figure 5.9) and applied to measure protein concentrations at the size exclusion zone. Of note, the OVA concentration range is a 10-fold greater than the OVA antibody concentration range in order to estimate K_D in an assumption that an excess amount of OVA is present compared to OVA antibody.

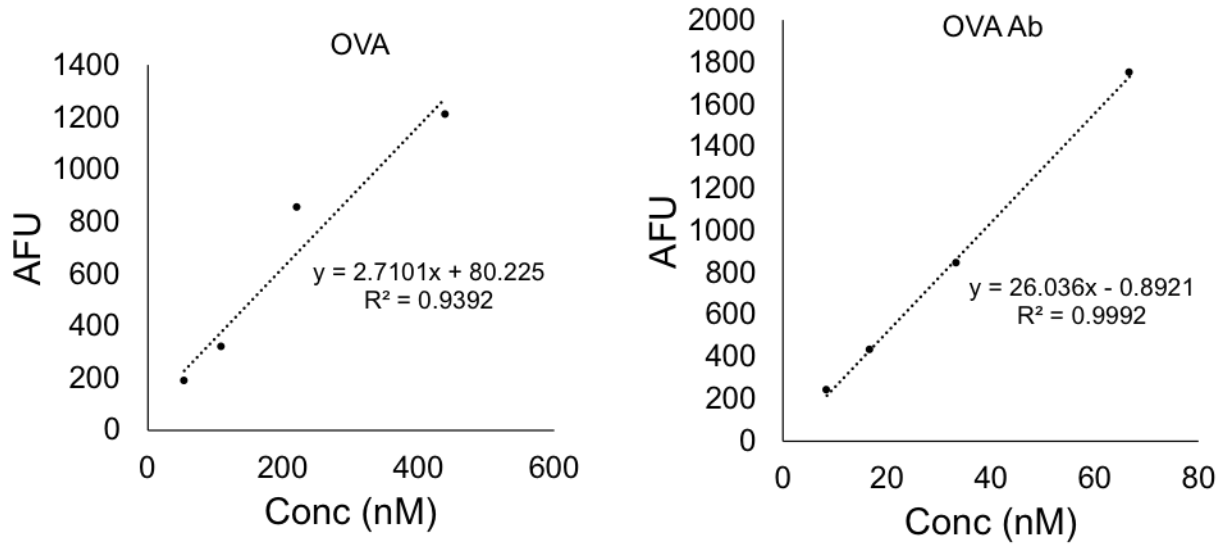

Figure 5.9: Calibration curves for fluorescence-tagged OVA and OVA antibody to extract amount of protein concentration based on fluorescence.

At the size exclusion zone in the microfluidic affinity device, a bimolecular binding reaction of OVA and OVA antibody is:

$$[OVA] + [OVA\ Ab] \underset{k_{off}}{\overset{k_{on}}{\rightleftharpoons}} [OVA : OVA\ Ab] \tag{5.2}$$

K_D, defined as k_{off}/k_{on}, is measured by:

$$\frac{[OVA : OVA\,Ab]}{[OVA]} = f_{max}(\frac{[OVA\,Ab]}{[OVA\,Ab] + K_D}) \tag{5.3}$$

where f_{max} is the fraction activity of OVA with OVA antibody at an excess concentration of OVA.

With a constant concentration of OVA and gradient concentrations of OVA antibody, K_D can be solved with the equation 5.2. With a fluorescent labeling on either OVA antibody or OVA, the equation 5.2 can be modified, and K_D can be directly measured by the fluorescence level of bimolecular complex, OVA:OVA Ab:

$$[OVA : OVA\,Ab] = [OVA : OVA\,Ab]_{max}(\frac{[OVA\,Ab]}{[OVA\,Ab] + K_D}) \tag{5.4}$$

where OVA:OVA Ab is the amount of fluorescence emitted from the binding formation [25]. Following the K_D measurement, an electric field of 300 V/cm was applied continuously

with a washing buffer (1x tris-glycine buffer) at the size exclusion zone to measure OVA fluorescence. The decrease in OVA fluorescence over time is analyzed by fitting with an exponential decay to estimate the dissociation rate (k_{off}) for OVA isolating from the OVA antibody:

$$\%OVA\ Bound = e^{-k_{off}t} \tag{5.5}$$

With the microfluidic affinity device, K_D and k_{off} values of OVA and OVA antibody are 23 nM and 1.67 x 10^{-4} s^{-1}, respectively (Figure 5.10). Because the K_D is a ratio of the dissociation (k_{off}) to association (k_{on}) rates, the association rate (k_{on}) value is calculated to be 1.2 x 10^{-4} s^{-1} M^{-1}. The K_D value (23 nM) of OVA and OVA antibody measured from the microfluidic affinity device agreed with the value (~ 20 nM) measured by standard ELISA (Figure 5.10) [11]. The additional k_{off} measurement from the microfluidic affinity device is crucial for ligand-receptor discovery that K_D alone does not provide; k_{off} and k_{on} measurements enable to discern ligand-receptor complexes that have the same K_D values but different k_{off} and k_{on} values. Especially, the ligand-receptor lifespan (k_{off}) controls activation of biological processes, ranging from endocytosis [2, 26, 27] to signal transduction pathways [28, 29].

Overall, we developed an integrated microfluidic system that increases the throughput of sample preparation to measure the affinity of protein interaction. By directly measuring both K_D and k_{off} within hours, the microfluidic affinity device holds a great potential for massively developing and screening drugs in pharmacology.

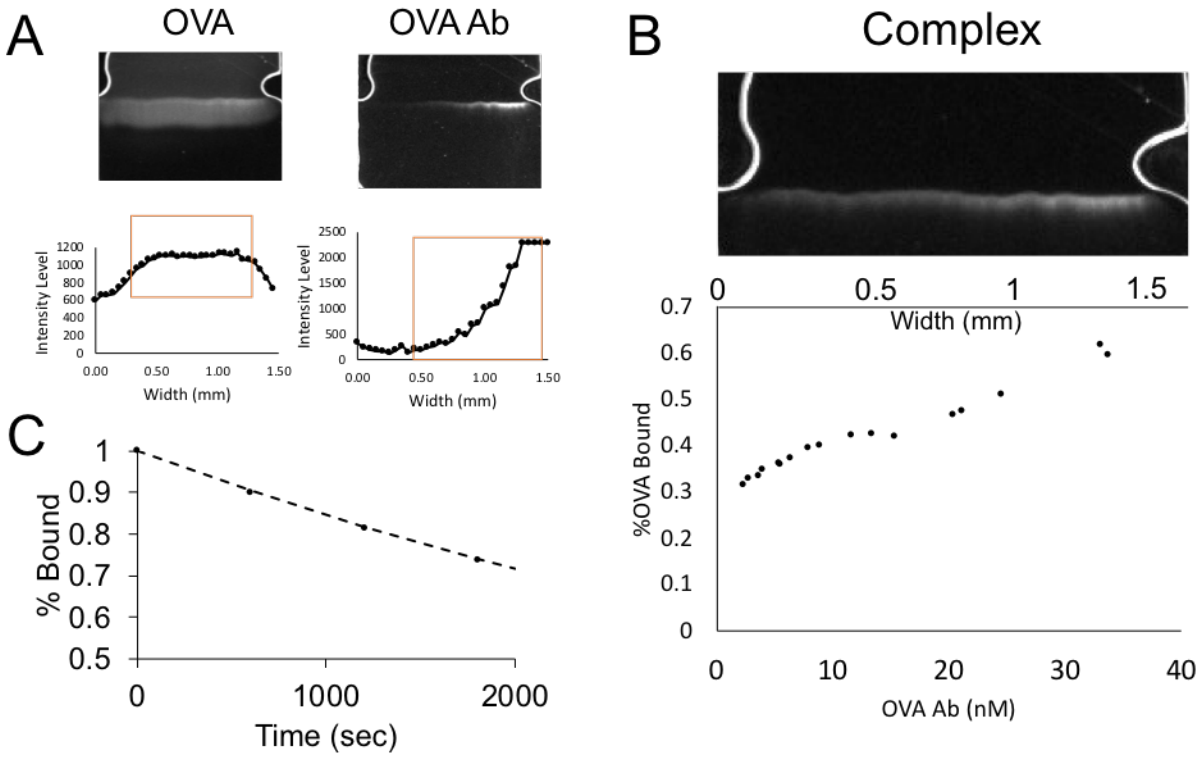

Figure 5.10: Measurement of K_D in the microfluidic affinity assay in a single run. (A, B) After binding of OVA and OVA antibody at the size exclusion zone, the fraction of OVA bound was measured with fluorescence across the channel width. K_D value was extracted by plotting the fraction of receptor-bounded OVA versus the concentration gradient of OVA antibody across the channel width.(C) By continuously electrophoresing with 1x tris-glycine, k_{off} is calculated by fitting % bound over time with the exponential decay curve. % Bound $= e^{(-0.000167t)}$, $R^2 = 0.99$, $k_{off} = 0.000167\ s^{-1}$.

Bibliography

1. Hoffmann, C *et al.* Ligand Residence Time at G-protein-Coupled Receptors-Why We Should Take Our Time To Study It. *Molecular pharmacology* **88,** 552–60. ISSN: 1521-0111 (2015).
2. Corzo, J. *Articles Time, the Forgotten Dimension of Ligand Binding Teaching* tech. rep. 6 (2006), 413–416. <http://www.bambed.org>.
3. Snozek, C. L., O'Kane, D. J. & Algeciras-Schimnich, A. *Pharmacogenetics of solid tumors: Directed therapy in breast, lung, and colorectal cancer - A paper from the 2008 William Beaumont Hospital symposium on molecular pathology* 2009. doi:10.2353/jmoldx.2009.090003.
4. Kousidou, O. C. *et al.* Estradiol-estrogen receptor: A key interplay of the expression of syndecan-2 and metalloproteinase-9 in breast cancer cells. *Molecular Oncology.* ISSN: 15747891. doi:10.1016/j.molonc.2008.06.002 (2008).
5. Rosenthal, A., Macdonald, A. & Voldman, J. Cell patterning chip for controlling the stem cell microenvironment. *Biomaterials* **28,** 3208–16. ISSN: 01429612 (2007).
6. Zon, L. I. *et al.* Developmental biology of hematopoiesis. *Blood* **86,** 2876–91. ISSN: 0006-4971 (1995).
7. Nam, K. *et al.* CD44 regulates cell proliferation, migration, and invasion via modulation of c-Src transcription in human breast cancer cells. *Cellular Signalling* **27,** 1882–1894. ISSN: 0898-6568 (2015).
8. Kolonin, M. G. *et al.* Interaction between Tumor Cell Surface Receptor RAGE and Proteinase 3 Mediates Prostate Cancer Metastasis to Bone. *Cancer research* **77,** 3144–3150. ISSN: 1538-7445 (2017).
9. Karlsson, R. SPR for molecular interaction analysis: a review of emerging application areas. *Journal of Molecular Recognition* **17,** 151–161. ISSN: 0952-3499 (2004).
10. Schuck, P. Reliable determination of binding affinity and kinetics using surface plasmon resonance biosensors. *Current opinion in biotechnology* **8,** 498–502. ISSN: 0958-1669 (1997).
11. Bobrovnik, S. A. *et al.* Traditional ELISA methods for antibody affinity determination fail to reveal the presence of low affinity antibodies in antisera: an alternative approach. *Journal of Molecular Recognition* **23,** 448–456 (2009).

12. Friguet, B *et al.* Measurements of the true affinity constant in solution of antigen-antibody complexes by enzyme-linked immunosorbent assay. *Journal of immunological methods* **77,** 305–19. ISSN: 0022-1759 (1985).

13. Squires, T. M., Messinger, R. J. & Manalis, S. R. Making it stick: convection, reaction and diffusion in surface-based biosensors. *Nature Biotechnology* **26,** 417–426. ISSN: 1087-0156 (2008).

14. Auld, D. S. *et al. Receptor Binding Assays for HTS and Drug Discovery* <http://www.ncbi.nlm.nih.gov/pubmed/22553864> (Eli Lilly & Company and the National Center for Advancing Translational Sciences, 2004).

15. Milton, J. D., Fernig, D. G. & Rhodes, J. M. Use of a biosensor to determine the binding kinetics of five lectins for Galactosyl-N-acetylgalactosamine. *Glycoconjugate Journal.* ISSN: 02820080. doi:10.1023/A:1019655303395 (2001).

16. Pan, Y. *et al.* Determination of equilibrium dissociation constants for recombinant antibodies by high-throughput affinity electrophoresis OPEN. doi:10.1038/srep39774. <www.nature.com/scientificreports> (2016).

17. Hu, S *et al.* Capillary sodium dodecyl sulfate-DALT electrophoresis of proteins in a single human cancer cell. *Electrophoresis* **22,** 3677–3682. ISSN: 0173-0835 (2001).

18. Kapil, M. A. *et al.* Kinetic Rate Determination via Electrophoresis along a Varying Cross-Section Microchannel. *Analytical Chemistry* **88,** 3669–3676. ISSN: 0003-2700 (2016).

19. Karns, K. *et al.* Microfluidic Screening of Electrophoretic Mobility Shifts Elucidates Riboswitch Binding Function. *Journal of the American Chemical Society* **135,** 3136–3143. ISSN: 0002-7863 (2013).

20. Takayama, S. *et al.* Selective Chemical Treatment of Cellular Microdomains Using Multiple Laminar Streams. *Chemistry & Biology* **10,** 123–130. ISSN: 1074-5521 (2003).

21. Noo Li Jeon *et al.* Generation of Solution and Surface Gradients Using Microfluidic Systems. doi:10.1021/LA000600B. <https://pubs.acs.org/doi/abs/10.1021/la000600b> (2000).

22. Holden, M. A. *et al.* Generating fixed concentration arrays in a microfluidic device. *Sensors and Actuators B: Chemical* **92,** 199–207. ISSN: 0925-4005 (2003).

23. Toh, G. M. *et al.* A low molecular weight cut-off polymersilicate membrane for microfluidic applications. *Microfluidics and Nanofluidics* **9,** 1135–1141. ISSN: 1613-4982 (2010).

24. De Jong, J., Lammertink, R. G. H. & Wessling, M. Membranes and microfluidics: a review. *Lab on a Chip* **6,** 1125. ISSN: 1473-0197 (2006).

25. Goodrich, J. A. & Kugel, J. F. *Binding and Kinetics for Molecular Biologists* **3,** 268–269. doi:10.1086/523132. <https://doi.org/10.1086/523132> (Cold Spring Harbor Laboratory Press, 2007).

26. Giudice, J., Jares-Erijman, E. A. & Coluccio Leskow, F. Endocytosis and Intracellular Dissociation Rates of Human InsulinInsulin Receptor Complexes by Quantum Dots in Living Cells. **04,** 53 (2018).

27. Birtwistle, M. R. & Kholodenko, B. N. Endocytosis and signalling: A meeting with mathematics. *Molecular Oncology* **3,** 308–320. ISSN: 1574-7891 (2009).

28. Pisolato, R. *et al.* Expression and regulation of the estrogen receptors in PC-3 human prostate cancer cells. *Steroids* **107,** 74–86. ISSN: 0039128X (2016).

29. Waters, C. M. *et al.* Rate constants for binding, dissociation, and internalization of EGF: effect of receptor occupancy and ligand concentration. *Biochemistry* **29,** 3563–3569. ISSN: 0006-2960 (1990).

Chapter 6

Conclusions and Future Directions

In this dissertation, we developed microfluidic devices that address challenges in collecting and interpreting protein information for precision medicine. We sought to investigate, characterize, and reduce the assay variability in sample preparation and protein analysis. By integrating sample handling with protein separation, we were able to achieve quantitative analysis of proteins from a low-number starting sample, estrogen receptor isoforms in response to hormone treatments, and protein binding kinetics. Moreover, the open microfluidic platform enables incorporation of microparticle-delivered protein markers for evaluating the chip-to-chip reproducibility and the sizing performance in the single-cell protein separation. For future directions in precision medicine and biomarker discovery, the workflow from sample collection to protein analysis needs to be fully automated and standardized to limit the addition of technical variabilities to complex biological systems. With specific regard to the single-cell protein assay improvement, we need to further develop the integrated assays that can massively record protein dynamics and post-translational modifications in order to provide quantitative analysis of signaling pathways, critical for personalized medicine.